

Investigation into Laser Re-melting of Inconel 625 HVOF Coating Blended with WC

By

Zuhair Yasin Al-Taha

BSc in Mechanical Engineering (KFUPM) KSA, 1990

MSc in Corrosion Control Engineering (UMIST) UK, 2003

This thesis is submitted to Dublin City University as the fulfillment of
the requirement for award of degree of

Doctor of Philosophy

Research Supervisors

Professor M.S.J. Hashmi (Ph.D., D.Sc., CEng., FIMechE., FIEI, MASME)
Professor B.S. Yilbas (Ph.D., D.Eng., MASME)

**School of Mechanical & Manufacturing Engineering
Dublin City University**

December 2008



Dedicated to

*My beloved wife
My passionate parents
My gorgeous children*

*For their endless support
and
patience
In critical periods*

*Without you, I could not
have finished this
achievement*

DECLARATION

I hereby certify that the material, which I now submit for assessment on the programme of study leading to the award of Doctor of Philosophy is my own work and has not been taken from the work of others save and to the extent that such work has been cited and acknowledged within the text of my work.

Signed: _____

ID No. 56102852

Date: _____

ACKNOWLEDGMENTS

I would like to express my gratitude to my supervisors, **Professor M.S.J. Hashmi and Professor B.S. Yilbas**, for their encouragement and guidance throughout my Ph.D. I am greatly indebted to them for giving special attention and support to my work and way of achievement.

My honest gratefulness to my dearly loved parents: **Yasin Al-Taha and Fakhriyah Al-Wosaibie** for their prayers, love, passionate, and care in the distance. My authentic gratefulness is expressed to my wonderful brother and sisters for their never ending support through my period of study.

It is always in my heart that, I am indebted to my beloved **wife Sana Al-Shaikh, my daughter Malak, my sons Ahmed and Ammar** who, as always, have given me endless love and support during my progress of study. They are the basis why I have kept a smile in my face and strength in my soul. The wide vision and long mission in front of us, made me realize how lucky I am of having them.

Last but not the least, I thank all my closed friends and colleagues at UMIST / DCU / KFUPM especially **Mr. Ali Adham** for being a true friend and for his support.

Title of Thesis: Investigation into Laser Re-melting of Inconel 625 HVOF Coating Blended with WC

Name of Student: Zuhair Y. Al-Taha **Student Number:** 56102852

ABSTRACT

High velocity oxy-fuel (HVOF) spraying of Diamalloy 1005 powders mixed with WC particles onto steel (304) is considered and laser re-melting of the resulting coatings is examined. Laser re-melting process is modeled to determine the melt layer thickness while temperature increase is formulated using the Fourier heating law. The morphological and metallurgical analyses prior and post laser re-melting process are carried out using scanning electron microscopy (SEM) and energy dispersive spectroscopy (EDS). X-ray diffraction (XRD) technique is used to determine the residual stress developed in the coating while the analytical formulation is adopted to predict the residual stress levels at the coating base material interface. The indentation tests are carried out to determine the Young's modulus and fracture toughness of the coating prior to laser re-melting. Corrosion resistance of coating is measured using potentiodynamic polarization technique prior and post laser treatment process. The predictions of the melt layer thickness are in good agreement with experimental results. The presence of WC particles modifies temperature rise and its gradient in the coating while affecting the Young's modulus, residual stress levels, and fracture toughness of the coating. The differences in the thermal properties of Inconel 625 powders and WC particles result in formation of small size cellular structure through polyphase solidification. WC dissolution in the central region of the large polycrystalline cells is observed due to the loss of carbon through carbonic gas formation. The results of corrosion tests prevail that significant improvement of corrosion resistance can be achieved after laser treatment process.

Table of Contents

	<i>Page</i>
Declaration	I
Acknowledgments	II
Abstract	III
Table of Contents	IV
List of Tables	VII
List of Figures	VIII
Nomenclature	X
Chapter 1 - Introduction	1
1.1 Types of Carbide Powder Are Used With HVOF Spraying ..	4
1.2 HVOF System Disadvantages	5
1.3 Lasers & Laser Beam Interaction with Materials	6
1.3.1. Laser Basic	6
1.3.2 Types of Lasers	8
1.3.2.1 Laser Surface Treatment.....	10
1.3.2.2 Laser Transformation Hardening	10
1.3.2.3 Laser Melting	10
1.3.2.4 Laser Alloying	11
1.3.2.5 Laser Cladding / Clad Re-melting	11
1.4 Clad Re-melted Layer Properties	12
1.4.1 Fusion Depth	12
1.4.2 Porosity	14
Chapter 2 - Literature Review	18
2.0 Introduction	18
2.1 Materials Characterization of HVOF Coatings	18
2.2 Materials Characterization of Laser Treated HVOF Coatings	33
2.3 Modelling of HVOF Coatings	39

2.4 Summary of Literature Review	40
Chapter 3 - Experimental Equipment & Procedures	43
3.0 Introduction	43
3.1 Specimen Design	44
3.2 Surface Preparation	46
3.2.1 Grit Blasting	46
3.2.2 Sample Mounting	47
3.3 HVOF Thermal Spraying Process	47
3.3.1 HVOF Coating Powder	47
3.3.2 HVOF and Laser Equipments	48
3.4 Characterization Tests	54
3.4.1 Potentiodynamic Anodic Polarization	54
3.4.2 SEM & EDS and Optical Microscope	54
3.4.3 X-Ray Diffraction (XRD)	57
3.4.4 Indentation Tests and Fraction Toughness Measurement	58
3.5 The XRD Technique for Residual Stress Measurement.....	59
3.5.1 Analytical Expression for the Residual Stress	60
3.5.2 Determination of Young's Modulus and Fracture Toughness by Indentation Test	61
Chapter 4 - Mathematical Analysis	65
4.0 Introduction	65
4.1 Melt Depth Formulation	66
4.2 Temperature Formulation	81
Chapter 5 - Results and Discussions	90
5.0 Introduction	90
5.1 Morphological and Metallurgical Changes in Coating	90
5.2 Mechanical Changes and Thermal Analysis in Coating	99
5.3 Corrosion Behaviour	114
Chapter 6 – Conclusions and Suggestions for Future Work	120

Suggestions for Future Work	123
References	125
Publications by the Author	138

List of Tables

	<i>Page</i>
1.1 Comparison of thermal spraying processes and coating characteristics	2
3.1 Chemical composition and size of HVOF powder Inconel 625 & WC	48
3.2 Process parameters of HVOF thermal spray	49
3.3 X-Ray Diffraction machine specifications	57
3.4 Properties of the coating material used in equation	61
3.5 Data obtained after indentation tests. The error estimated based on the repeats of the indentation test is 7%	64
4.1 Thermal properties used in the simulations for inconel 625 powder	80
4.2 Material properties used in the simulations	89
5.1 EDS results for the laser melted region for HVOF Inconel 625 coating. Each spectrum represents the different points across the cross-section of the coating after the laser treatment. The existing of gold in the spectrums is because of the gold coating of the samples prior to the EDS analysis.....	97
5.2 Residual stress measured using XRD technique and determined from analytical formulation. The error estimated based on the repeats of the XRD measurements is in the order of 5%	106
5.3 EDS analysis results for as received and laser melted coating. The WC content is 9.3% untreated coating	111
5.4 Phase constitutions of various coatings before and after laser treatment by XRD	118
5.5 Corrosion parameters of various coatings before and after laser treatment	119

List of Figures

	<i>Page</i>
1.1 Schematic of high velocity oxy-fuel (HVOF) spraying system	3
1.2 Light amplification by the stimulated emission of radiation	7
1.3 Range of laser processes mapped against power density per unit time	9
1.4 Cross-section of a single clad layer with definition of the clad geometry: clad height (hc), clad depth (dc), total clad height (tc) and clad width (wc)	13
1.5 Inter-run porosity	14
3.1 The workpieces were located close to each to attain uniform thermal spray	45
3.2 Cutting machine used to sectioned the coated samples ..	45
3.3 Enviraclean grit blasting machine used to clean and rough on the specimens surfaces	46
3.4 HVOF JP-5000 unit used in spraying Inconel 625 with and without WC inclusion	51
3.5 Rofin DC 020 (Diffusion-cooled Slab CO ₂) CO ₂ laser equipment	52
3.6 A Laser line 160–1500 LDL 1.5 kW diode laser	53
3.7 Scanning electron microscope model JEOL JDX 3530 LV.	56
3.8 Olympus BX 60 optical microscope with Polaroid digital microscope camera (DMC)	56
3.9 X-Ray Diffraction machine model AXS D8 Bruker Inc.....	58
3.10 The indentation testing BUEHLER machine used to get fraction toughness of the surface	59
3.11 The indentation geometry used in the calculations	64
4.1 A schematic view of liquid- and gas-side velocities in the coordinate system	80

4.2	A step input pulse intensity used in the analysis	87
4.3	Construction of a step input intensity pulse	88
4.4	Two laser pulses used in the simulations	88
5.1	Melt layer thickness with laser power predicted from the lump parameter analysis and obtained from the experiment.	92
5.2	SEM micrograph of HVOF coating cross-section prior to laser melting	93
5.3	SEM micrograph of laser HVOF coating cross-section after the laser treatment. The cellular structure is clearly observed	96
5.4	SEM micrograph of laser HVOF coating cross-section after the laser treatment. The corrugations of the cellular structure are observed	98
5.5	SEM micrograph of laser HVOF coating cross-section after the laser treatment. The differences in the cell sizes are observed due to non-uniform cooling rates	98
5.6	SEM micrograph of laser HVOF coating cross-section after the laser treatment. The dendritic structure is observed in the surface region of the coating	99
5.7	Temporal distribution of temperature due to two consecutive laser pulses	101
5.8	Temperature distribution inside the coating at two different heating periods	103
5.9	SEM and optical micrographs of coatings with and without WC	108
5.10	EDS line scan in the coating. The existing of low peaks of W and slope of WC peaks indicates the existence of W ₂ C and WC dissolution in the coating	109
5.11	SEM micrographs of laser melted coatings with and without WC	112
5.12	XRD results for laser treated and un-treated coating (9.3% WC content)	114
5.13	Polarization curves of Sample 47 wt.% of WC before and after laser treatment	118

Nomenclature

A	Area (m^2)
C	Constant
C_1	Laser Intensity multiplication factor
C_p	Specific heat capacity (J/kgK)
C_{p_g}	Specific heat capacity of gas ($J/kg.K$)
C_{p_m}	Specific heat capacity of liquid ($J/kg.K$)
C_{p_s}	Specific heat capacity of solid ($J/kg.K$)
C_H	Heat transfer parameter
C_f	Skin friction coefficient
D	Diffusion coefficient (m^2/s)
d, d_n	Lattice spacing (m)
E_{in}	Laser power available at liquid surface (W)
$E_{Conduction}$	Rate of energy conducted (W)
$E_{Convection}$	Rate of energy convected (W)
E_{req}	Rate of energy required for melting (W)
E	Elastic modulus (Pa)
E_c	Elastic modulus of coating (Pa)
E_s	Elastic modulus of base material (Pa)
$Erfc$	Co-error function
h	Heat transfer coefficient (W/m^2K)
h_o	Total enthalpy of gas at the edge of the boundary layer (J/kgK)
h_g	Total enthalpy of gas at the melt surface (J/kgK)
h	elastic penetration (m)
HV	Vickers hardness (Pa)
I	Laser power intensity (W/m^2)
I_1	Power intensity ($I_o(1-r_f)$) (W/m^2)
I_o	Power intensity (W/m^2)
k	Thermal conductivity ($W/m.K$)
K	Fracture toughness ($Pa/m^{1/2}$)
K	Thermal conductivity (W/mK)
L_m	Latent heat of melting (J/kg)
L_{ev}	Latent heat of evaporation (J/kg)
\dot{m}_g	Assisting gas mass flow rate (kg/s)
\dot{m}_L	Liquid mass flow rate (kg/s)
Pr	Prandtl number
P_o	Laser output power reaching the melt surface after reflection (W)

P	Applied load (N)
Re _L	Liquid layer Reynolds number
R	Indenter equivalent diameter (m)
r _f	Surface reflectivity
s	Distance along the workpiece surface (m)
Sc	Schmit number
SP(t)	Temporal function for laser pulse profile
T _{ev}	Boiling temperature (K)
T _m	Melting temperature (K)
T _{oi}	Initial temperature of the workpiece (K)
T _{oe}	Gas temperature at the edge of the boundary layer (K)
T _{ref}	Reference temperature
T	Temperature (K)
T(x,t)	Temperature (K)
T _o	Ambient temperature (K) ($= T_o \frac{k\delta}{I_1}$)
Δt	Laser pulse length (s)
t	Time (s)
t _s	Base material thickness (m)
t _c	Coating thickness (m)
U _e	Gas velocity at the edge of the gas boundary layer (m/s)
U _L	Melt velocity (m/s)
U _{LS}	Melt velocity at the melt surface (m/s)
V _L	Melt velocity normal to the surface (m/s)
x	Distance along the laser beam axis (m)
y	Distance normal to the workpiece surface (m)

Greek

α	Thermal diffusivity (m ² /s)
α _s	Thermal expansion coefficient of base material (1/K)
α _c	Thermal expansion coefficient of coating (1/K)
α	Thermal diffusivity (m ² /s)
β	Evaporation factor , <1
δ	Absorption coefficient (1/m)
δ _L	Liquid layer depth (m)
η	Dimensionless distance (= xδ)
ν	Poisson's ratio
ρ	Density (kg/m ³)

ρ_g	Density of assisting gas (kg/m ³)
ρ_L	Density of molten metal (kg/m ³)
ρ_s	Density of solid material (kg/m ³)
σ	Stress (Pa)
ψ	Tilt angle
$\theta(\eta, \tau)$	Dimensionless temperature ($= T(x, t) \frac{k\delta}{I_1}$)
θ_o	Dimensionless ambient temperature
τ	Dimensionless time ($= \alpha\delta^2 t$)
$\Delta\tau$	Dimensionless pulse length of laser pulse

Chapter 1 - Introduction

Several surface treatment techniques including coatings are available to improve the surface properties of metallic parts. The thermal spray processes is well-established technique in this regard. The attribution of these techniques is recognized in the application and deposition of surface layer with required properties on top of substrate material surfaces with poor properties. Depending on the feature of applied technique, common problems would be of a dispute as combination of a poor bonding of the applied surface layer to the base material, the occurrence of porosity, the thermal distortion of the workpiece, the mixing of the surface layer with the base material and the inability of a very local treatment.

One of the techniques that provide structural homogeneity through thermal integration called laser cladding or re-melting. Laser cladding has been defined as a process which is used to fuse a material with a laser beam to another material. The re-melting surface has different metallurgical properties on a substrate with only very thin layer of the substrate has to be melted in order to achieve strong bonding. The minimum diffusion of coating into the substrate is regarded for the

integrity of coating and maintaining the original properties of the coating material [1, 2].

Thermal spraying family is well known system as well of being used to form a composite layer and vary from one to another in performance and quality. High velocity oxy-fuel (HVOF) is one of the family is considered to be excellent and the best among other types as stated in Table 1.1 [2].

Table 1.1. Comparison of Thermal Spraying Processes and Coating Characteristics [2].

Process	Particle Velocity (m/s)	Adhesion (MPa)	Oxide Content (%)	Porosity (%)	Deposition Rate (kg/hr)	Typical Deposit Thickness (mm)
Flame	40	<8	10–15	10–15	1–10	0.2–10
Arc	100	10–30	10–20	5–10	6–60	0.2–10
Plasma	200–300	20–70	1–3	1–8	1–5	0.2–2
HVOF	600–800	>70	1–2	1–2	1–5	0.2–2

HVOF coating is to be considered one of the most recent thermal spraying family added technique, has become as an alternative to others in properties such as detonation (D-GUN) flame spraying and the lower

velocity, air plasma spraying processes for depositing wear resistant coatings. However, HVOF is a system that delivers high pressure and flow rate compared with those in the atmospheric burning flame spraying system due to internal combustion process (Figure 1.1) [2].

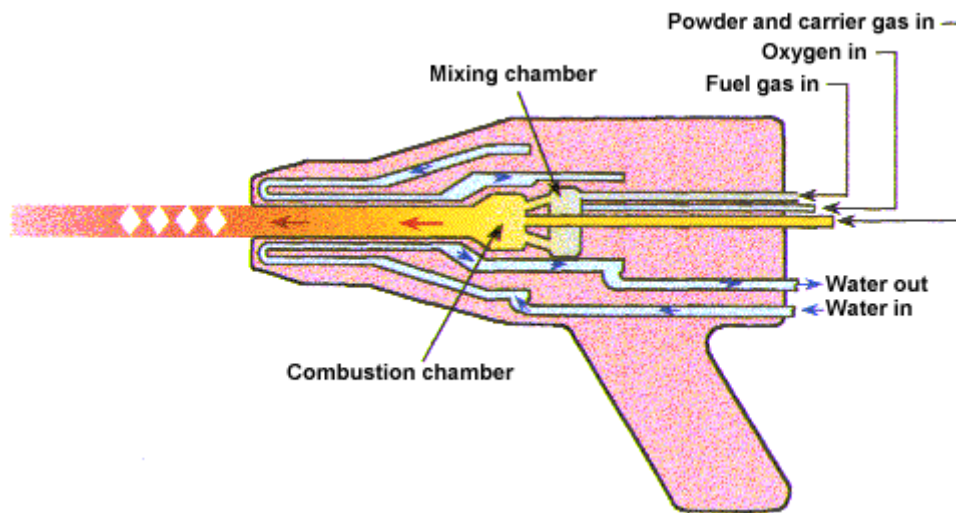


Figure1.1. Schematic of High Velocity Oxy-fuel (HVOF) spraying system [2].

There are different types of HVOF systems which can be utilized in research and experiments or even in practice such as diamond jet hybrid, modified diamond jet, JP5000, DJ2700, and TopGun [3,4]. However, the applications of HVOF sprayed coatings have been growing gradually in the last two decades because of increased use of surface engineering.

It has been developed primarily for wear resistance at different industrial locations like aerospace. The major utilization of the system as succeeded with superiority in technical and competitively in commercial is base on corrosion and wear protection, as well as repair of worn components [3, 5]. In relation with sort of properties consideration in performance of coating such as mechanical, process, microstructure and parameters, the type of coating powders has significant effects of HVOF on the wear-corrosion, and other properties of the resulting surface. Moreover, use of carbide particles can improve the tripological properties of the resulting coating surface.

1.1 Types of Carbide Powder Are Used With HVOF Spraying

One class of coatings widely prepared using the HVOF spraying process is carbide-containing composites, called cermets. Because of their combination of high hardness, moderate toughness, good adhesion and chemical stability in many service environments, these coatings are widely used to provide protection against wear.

The main components are tungsten carbide or chromium carbide particles in a metallic alloy matrix consisting of various combinations of Co, Ni or Cr. The two most common carbide coatings are WC-Co and

$\text{Cr}_3\text{C}_2\text{-NiCr}$. In the HVOF process, these materials are sprayed as a powder consumable. The main keys of powder characteristics needed during manufacturing process control to achieve compatibility of resulting needed of coating can be summarized in particle grain size, homogeneity of carbide dispersion within the powder particle, density of the powder particle, shape of the powder particle and particle size distribution [6].

1.2 HVOF System Disadvantages

However beyond the performance of HVOF spraying application compared with other systems, there are also disadvantages associated. HVOF sprayed coatings can be found complicated with their properties and microstructure depending on processing variables. For instant, restriction to sintering powder sizes of a range of about 5 - 60 μm with a need for narrow size distributions. Moreover HVOF spraying requires experienced and qualified applicator is of high demand to ensure safe operation and to achieve consistent coating quality. Proper controlled automated and robotic of an HVOF spray gun is required more than manual control. The design of the gun is limited for larger equipment size and to be found extremely not accessible to internal of small

cylindrical components narrow paths as long as maintaining distance of 150-300 mm is required [7].

1.3 Lasers & Laser Beam Interaction with Materials

Laser treatment techniques is considered to be the advanced way to form a layer with better performance compared with conventional methods like thermal spraying in terms of their advantages in chemical cleanliness, thermal penetration, and surface profile with absence of voids and oxides as well [1].

1.3.1. Laser Basic

Simple laser is made of two parallel mirrors named as resonators. It is meant to create an optical oscillator in which light would oscillate back and forth between the mirrors. Considering a lasing medium between the mirrors, the process of Light Amplification by the Stimulated Emission of Radiation would be achieved and hence named as laser (Figure 1.2) [1, 8].

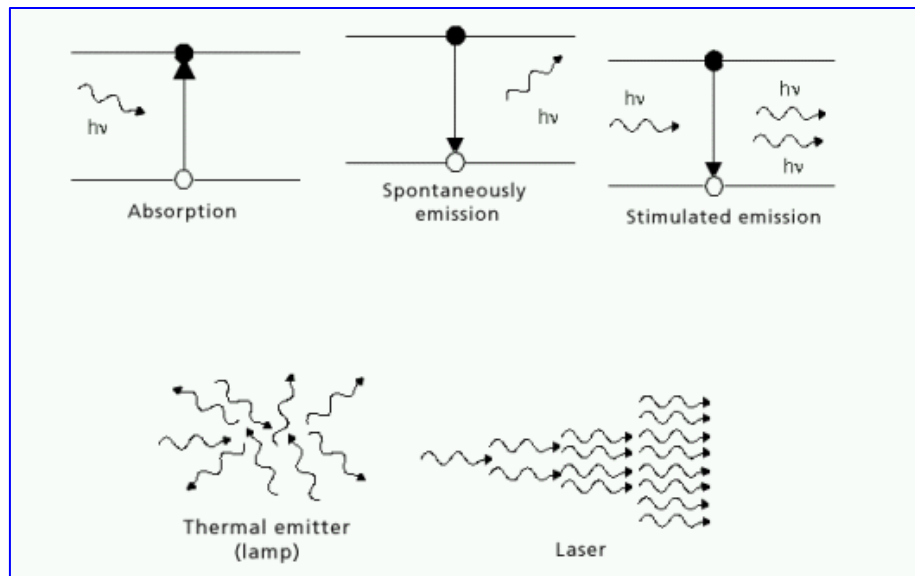


Figure 1.2. Light Amplification by the Stimulated Emission of Radiation [8].

There is a straightforward approach to understand laser processing which is relevant for every situation. This approach considers only processes that can occur when a laser beam strikes a surface and expressed in: $\text{Reflection} + \text{Absorption} + \text{Transmission} = 1$ with possibility of occurrence of all of them in practical [1]. The other approach that some of these pure Light Amplification beam hit the target, some photons would be absorb and they would be converted into thermal energy at the target surface as heat. The heat generated may be conducted, radiated or convected away from the area. In most practical situations, convection and radiation are playing in a very narrow

occasion however conduction is the prevailing process. Once the heat enter to the target area with higher rate than the rate of conduction of heat away from the target, then melting or vaporization or both combined together would occur due to raise of temperature locally with possibility of sublimation as indicated by some scientists. In general assumption and usually in most of industrial laser processes, the target would absorb significant proportion of the light amplification beam. Furthermore, it is widely accepted that there are three dominating factors playing the big rule in laser processes as of average power, intensity of the laser spot in the target and wavelength of the laser beam [1,8]:

1.3.2 Types of Lasers

There are many kinds of lasers manufactured today and each produce laser light at a unique frequency. However, the most common lasers used in fabrication are the carbon dioxide (CO₂) laser, the Nd:YAG (neodymium-yttrium aluminum garnet) laser, and the diode laser. The CO₂ laser uses a mixture of gases including CO₂ as the active medium and produces light with a 10.6-micron wavelength. The Nd:YAG laser uses a crystal as its active medium and produces light with a 1.06-micron wavelength. The diode laser uses a semi-conductor diode

material as its active medium can be manufactured to produce one of several wavelengths.

There are many laser types. Each type of laser has its advantages and disadvantages and is therefore used for different applications. In addition, laser process in industrial have been extended to cover many applications such as welding, cutting, drilling and in little wide range in surface treatment that is covering diversify range of areas (Figure 1.3) [1].

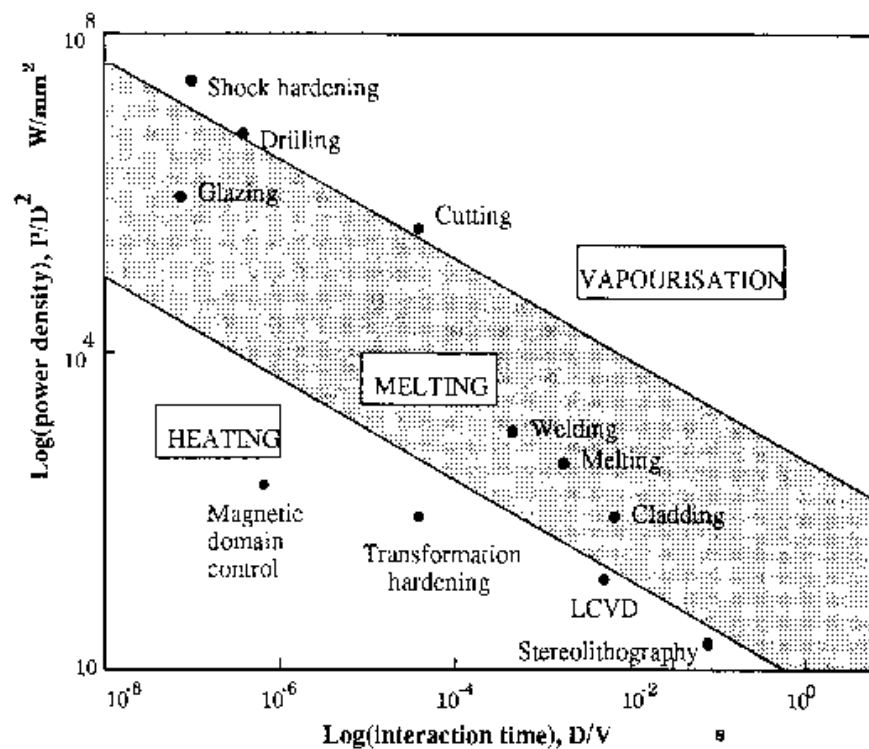


Figure 1.3. Range of laser processes mapped against power density per unit time [1].

1.3.2.1 Laser Surface Treatment

It is called laser surface modification increasingly used in industrial to change the surface of a component to develop a reliable material work against aggressive environments (high temperature and corrosive environments). Different types of modifications are available to do the change required as of laser transformation hardening, laser melting, laser alloying and laser cladding (re-melting) [1].

1.3.2.2 Laser Transformation Hardening

Laser hardening is one of surface treatment techniques justified for developing high stressed and hard surfaces to avert to better wear resistance and increase in fatigue life in respect to change in microstructure [2].

1.3.2.3 Laser Melting

It is similar of laser surface hardening as meant in surface melting through application of a focused or near focused beam in order to gain fine homogeneous structures with ensuring covering the substrate with inert gas [1, 2].

1.3.2.4 Laser Alloying

The processing of hardening and melting are closed related to laser surface alloying (LSA) with modifying the process to add alloying elements in the melt pool while changing the chemical composition in surface region. In order to achieve the required properties, alloying elements can be introduced either with inert gas or with powder feed line if available in the system [1, 2].

1.3.2.5 Laser Cladding / Clad Re-melting

Laser cladding / clad re-melting can form metallurgical bond between two materials and lead to new microstructure with desirable properties at the surface. As laser with its function of producing high power densities, it will have the ability to generate heat reaching to melt the substrate and some of the cladding particles. With controlled power density, fusion of metal onto another metal with minimal thermal input can be attained. Selection of suitable cladding materials can increase the component wear, hardening and corrosion resistance with well-established parameters of laser processing.

In principle there are two possibilities of realizing the process of cladding [1, 2]:

- Pre-placed powder process (two stages) as meant of clad re-melting.
- Blown powder process (one stage) as meant of cladding with surface re-melting.

1.4 Clad Re-melted Layer Properties

It is found to be complicated in practice to generate a clad re-melted layer with all desirable requirements such as geometric features, mechanical properties, metallurgical properties, and other qualitative properties. Moderating the requirements of such properties has to be evaluated and assessed against environments. Application of preheating the substrate material prior to laser implementation can lead to reduce the cooling rate and eventually lowering the residual stress levels. Crack prevention is an important issue against the initiation of corrosion fracture and reduce fatigue strength [9,10].

1.4.1 Fusion Depth

Formation of a melt pool in the substrate is highly required to perform strong fusion bonding with clad layer. However, part of metallurgical and geometrical properties in laser re-melting, depth of clad melt into substrate need to be as small as not to be fused deep with the base

material in order to obtain a pure surface that characterizing the quality of layer. The fusion depth measurements can be carried out in two ways. One way of defining the fusion depth is based on the clad layer geometry by means of the ratio of the clad depth (d_c) in the substrate over the total clad height (t_c) with the assumption of homogeneity in elements distribution over the clad cross section geometrical. (Fig. 1.4)

The other way of assessment the fusion depth can be made through analysis of the material composition in the clad layer. In more detail, an evaluation is to be made between the material composition of the pure coating material and the composition of the substrate. This way permit recognizing the variation of the fusion over the clad depth and is preferred over the geometrical approach [11].

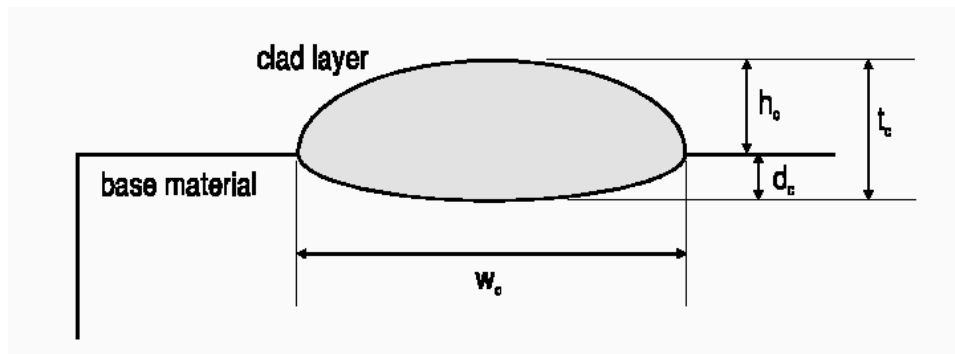


Figure 1.4. Cross-section of a single clad layer with definition of the clad geometry: clad height (h_c), clad depth (d_c), total clad height (t_c) and clad width (w_c) [11].

1.4.2 Porosity

Voids in the clad layer are called porosity which can be resulted through different process occasions. They may be created due to trapped gas bubbles in the melt pool during cooling and solidification. However, this can be reduced by vibrating the workpiece which has an advantage of reducing also cracks and internal stresses. The other reasons to form the porosity is the solidification process, which proceeds different directions, i.e. resulting and causing tensile stress in the layer with possible formation of holes. Impurities like presence of some flaws of grease during laser processing can affect the bonding between the clad and substrate causing the porosity formation.

During overlapping tracks of continuous laser application, ‘inter-run porosity’ as called can appear as referred in Figure 1.5 due to excess laser power supplied [11].

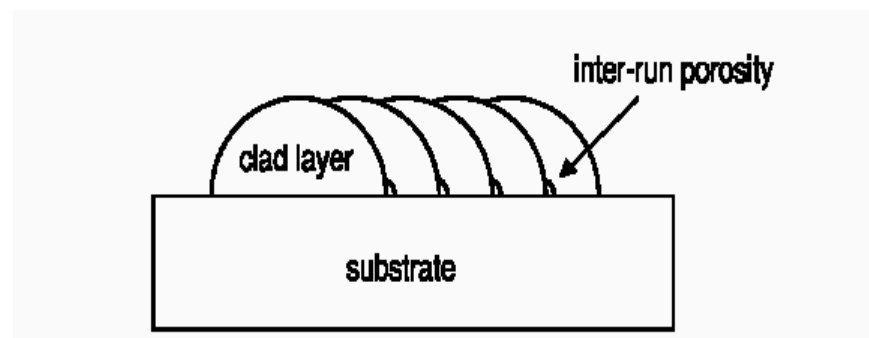


Figure 1.5. Inter-run porosity [11].

High Velocity Oxy-fuel (HVOF) coatings in specific are widely used in industry for the wear preventions and high temperature protection of surfaces. The coating powder has resistance to high temperature and to abrasive operations, which enables the coating to be used in the power industry. Moreover, WC addition to the powder improves the wear properties of the coating significantly. In HVOF coating process, the splats (semi-molten powder) anchors to the grit blasted surface through the mechanical locking. As the spraying progresses, the splats build up forming the coating layers. The particles during in-flight remain in semi-molten state, which give rise to the formation of porous structures in the coating. This causes a non-homogeneous structure being formed in the coating. Thermal integration of the splats in the coating reduces the porosity and improves the structural integrity in the coatings. This can be achieved through controlled melting of the resulted coating. The laser melting process has several advantages over the conventional melting methods. The local heating resulting in narrow heat affected zone, precise operation, and fast processing time are the main advantages. However, the thermal strains developed during the heating and cooling cycles differ significantly inside the coating. This, in turn, results in the development of the excessive stress field in the coating and in some

cases the crack formation at the stress centers in the coating becomes unavoidable. Consequently, investigation into microstructural changes and temperature rise during the laser melting process become essential for possible structural integration in the coating with low stress levels.

In the present study, laser re-melting of HVOF coating of Inconel 625 including WC particles is considered and the microstructural analyses prior and post laser re-melting is carried out. Inconel and WC mixture are used as the spraying powders while stainless steel (SS 304) is accommodated as the base material for spraying. The selection of Inconel 625 powder is because of its wide usage in industry. However, addition of WC provides improved hardness of the resulting coating. Since, Inconel 625 and WC have different properties, structural integrity of the coating needs improvement through controlled re-melting. Consequently, the influence of WC content in the microstructure of the coating after laser re-melting is also investigated.

The thesis consists of six chapters as the first chapter presents introduction of HVOF coating and laser re-melting processes. The second chapter reports the literature review pertaining to previous works carried out in regards to finding and assessment of the state of the art

and application of HVOF and laser treatments. This review survey is performed and classified into four related categories of HVOF coating. They are of pertaining to coating processes and characterization, coatings and WC addition, coatings and laser treatment and finally coatings and corrosion. In chapter three, equipment used in the experiment with specimen preparations, spraying, procedures, and laser facility used in the experiment were presented. Furthermore, the morphological and metallurgical examinations were carried out using EDS, optical microscopy and SEM. XRD technique for residual stress measurement was applied. Last in this chapter, determination of young's modulus and fracture toughness measurement was also carried out using indentation tests. However, the laser heating process is modeled using the lump parameter analysis, which is presented in chapter four followed by simulation the equation for temperature distribution with different concentration of WC in Inconel 625 powder. Results and discussion is given in chapter five of the thesis. The findings of experimental tests and theoretical model are discussed in details in this chapter as well. The limitations of equipments and model study are also given. Finally, the conclusion and future work are presented at the end of the thesis in chapter six.

Chapter 2 - Literature Review

2.0 Introduction

The studies reported in the open literature related to the materials characterization of HVOF coatings and application of laser treatment are presented in the following literature survey. Considerable numbers of investigations have been carried out while using different types of equipment as well as materials and processes in order to secure high coating performance and quality as judged by the mechanical, metallurgical, corrosion, and erosion properties.

The published work in the literature survey covers the period of past 15 years. The literature survey will be presented under the relevant sub-headings.

2.1 Material Characterization of HVOF Coatings

Different types of gaseous fuels have been used recently with HVOF coating process such as hydrogen, propylene, propane, and acetylene. However, the use of liquid fuel (kerosene) in HVOF system is found to produce thick deposition layers of coating as compared with gaseous

fuels units [2, 12]. Sturgeon [4] reported that the deposition efficiency is exceeding more than twice of JP5000 and DJ2700 systems when the TopGun HVOF system was used. They indicated that this was due to design of dwelling time of the TopGun spraying facility, which resulted in high temperature powder particles in the spraying jet as compared with other HVOF facilities.

Particle velocity is one of the important parameters in thermal spray process. Higher the particle velocity results in higher the bond strengths. This gives rise to low porosity due to reduced cooling period, provided that the particles are impacting the preheated substrate surface within a semi-molten state. The HVOF process is designed to produce high particle velocities, and this contributes to the advantages of HVOF coating over the other thermal spray processes [13 - 15].

It was demonstrated that temperature tends to increase during spraying a nanostructured WC-12Co cermet powder through using the different gun-fuel in descending order JP-5000 kerosene, DJ-2600 hydrogen, and DJ-2700 propylene. However, the velocity of particles tended to decrease in the same order. High velocity with maintaining high temperature could promote the coating properties due to improvement of

bonding and adhesive strength of multiple layers through kinetic energy gain of the particles during spraying. Moreover, the low temperature would endorse low melting and low viscosity that lead to possible rebounding of particles and increase of porosity. Hardness of the coatings increased while using DJ-2600 hydrogen as compared to DJ-2700 propylene due to the increase in temperature and velocity [13, 15, 16].

Increasing the stoichiometric factor of oxygen / fuel ratio was measured for the flame during spraying of Inconel 718, which was found to decrease the flame temperature and increase the velocity of the flame. It was observed that the percentage of oxide contents was also increased. Moreover, producing dense coating can be possible due to the increase of oxides in the coating as a result of the increase in combustion pressure. However, the porosity was at constant level with the increase of combustion pressure regardless of the stoichiometry ratio [17-19]. However, Lugscheider et al. [18] highlighted the importance of spraying parameters on the resulting coating characteristics. Increase in the spray distance was correlated to the adjustment of substrate temperature in restraining the severe oxidization by reducing the heat load on the substrate. The increase in the powder feed rate was found to reduce the oxide contents due to the incomplete melting of particles. Thus, building

a thick layer pass with high feed rate could create residual stresses in the coating. As a result of this study, hydrogen / oxygen ratio was expected to be high enough to reduce the oxides with maintaining thin layers of coating [20].

Fixing the cylindrical shroud at the end of the jet nozzle was intended to reduce in-flight oxidation of the powder. It was found that the increase of particle temperature with decrease in particle velocity was possible while applying the shroud. It appeared that the geometry of the cylindrical shroud produced low quality of coating because of low bonding strength. Thus, re-designing the shroud to minimize the re-circulation of the flow inside the shroud as noticed would be of future study [21].

Nuruzzaman et al. [22] examined the surface durability of HVOF coating (WC-Cr-Ni) in lubricated rolling with sliding contact conditions against the substrate material and its surface finish. They applied two-roller testing machine to investigate the durability of the steel roller with and without coating. While using thermally refined steel substrates during the test, formation of flaking was noticed in steady condition if the substrate was axially ground. On the other hand, with blasted or circumferentially ground substrate of coated roller, the coating durability

of the roller was indicated to be inferior with the increase of coating thickness. However, the coated rollers were found to be harder and demonstrated a longer life compared with the thermally refined steel substrates. Furthermore, the condition of the substrate exhibited significant effect on the surface durability of thermally sprayed WC cermet coating, which was due to the higher hardness of the substrate [22]. HVOF coating of micron and nano sized WC-Co powders was examined by Cho et al. [23]. They showed that WC-Co coating was protective for the sliding machine component, since the hardness of the coating was 2-3 times higher than those of machine component materials. It was shown that the WC-binder adhesion and adhesion between splats is correlated with hardness and toughness of the coatings. Increase in WC-binder adhesion could increase decarburization as a result of high flame temperatures, in which it was found afterward to decrease adhesion between the splats. Decarburization is to be considered one of the most prominent problems affecting the integrity of nanostructured coating because of their relatively large surface area. To overcome and to reduce the decarburization, additive in Infralloy was decreased the adhesion between WC grains and binder. This study showed that increasing in the decarburization would adversely decrease the wear resistance while the hardness would increase the wear

resistance. Qiao et al. [24] indicated that worn out of the WC grains and the lifting of entire splats was affecting the sliding wear. However, they associated the occurrence of abrasive wear related to ductile cutting, grain loss, and lifting of splats. Moreover, splat-boundary weakening, by fatigue, extended to the low wear rate in sliding. In general, as long the high abrasive wear removes material before fatigue becomes important, the abrasion wear was found to be inferior with decarburization. Unfavorably, decarburization could play a major role in sliding wear [24]. In addition, the effect of carbide size and cobalt content on the microstructure and mechanical properties of HVOF WC-Co coating were examined by Chivavibul et al. [25]. They analyzed the microstructures of the resulting coatings and they showed that the binder phase was a key factor affecting the microstructure of the coating.

High temperature gradients are developed in the HVOF coating, which result in the formation of high residual stress levels. Liao et al. [26] examined the residual stress developed in the coating using the curvature method. They indicated that the attainment of high temperature during coating caused the formation of high levels of the residual stresses, particularly in the surface region of the coatings. Stokes and Looney [27] analyzed the residual stress formation after the

HVOF coating. They showed that the residual stress levels changed from tensile to compressive as the coating thickness reduced. Thermal stress analysis of HVOF coating produced by WC-Co/NiAl powders was carried out by Toparli et al. [28]. They found that the stress distributions changed during the spraying and cooling phases because of the different mechanical properties of the coating layers. In addition, they demonstrated that the tensile stress was higher than the compressive stress. Lima et al. [29] investigated the residual stress levels in the HVOF coating using the material removal method. They indicated that the plastic deformation and quenching history of individual splats influenced significantly the stress levels in the coating. Gill et al. [30] studied the residual stress development in the HVOF coating. They showed that the curvature method for the residual stress measurement was reliable and accurate. Kesler et al. [31] investigated the residual stress formation in plasma sprayed coatings. The findings revealed that the thermal expansion coefficients and mechanical properties were the important factors influencing the residual stress levels. Santana et al. [32] measured the residual stress levels in the coating using the hole drilling method. They indicated that depending on the coating and base material properties, the residual stress could become tensile. Totemeier and Wright [33] examined the residual

stresses in the coatings using the curvature method and XRD technique. They showed that the residual stress levels in the coating became compressive as the particle velocity increased. Wang et al. [34] used the curvature interferometer technique to measure the residual stress levels in the coatings. They indicated that the residual stress formed in the surface region of the coating had significant effect on the wear properties of the coating. Ghafouri-Azar et al. [35] studied residual stress developed in the coating. They showed that the residual stress levels increased significantly with the increase in the coating layer thickness. Otsubo et al. [36] investigated the residual stress distribution in the coating. They showed that the residual stress levels remained almost uniform in the coating, except at the coating base material interface; in which case, it is reduced below the average value. McGrann et al. [37] examined the effect of the residual stress levels on the fatigue life of the coating. They indicated that the amount of tungsten carbide in the coating influenced the fatigue life of the coating.

The residual stress minimization through monitoring temperature of substrate material was considered as one of the target approaches. Many research studies in thermal spray techniques were focused on to avoid adhesion loss, formation of cracks, buckling, and interlaminar de-

bonding. Stokes et al. [38] succeeded in some extent to maximize the HVOF (WC-Co) coating thickness by application of carbon dioxide cooling system.

Fatigue failure modes of thermal spray (WC-12%Co) HVOF coatings on the surface of 440-C steel substrate were studied to correlate the performance with the influence of coating thickness and contact stress fields. A modified four ball machine under identical tribological conditions of contact stress, configuration and lubrication was used for rolling contact failure tests. The study showed that a non-dimensional coating thickness parameter might be applied as functional indicator to optimize coating delamination resistance during Hertzian contact loading. Moreover, fatigue life in excess of 70 million cycles without failure was of probability for attainment. It was attributed to the improvement in coating performance of an improved fracture toughness of coatings, in which liquid fuel was used [39]. On the other hand, typical study with same objectives was performed by Stewart et al [40], but with post-treatment (Hot Isostatic Pressing) on the Rolling Contact Fatigue performance of thermal spray (WC-12%Co) HVOF coatings. Temperature range in between 850 °C and 1200 °C was set inside the furnace during the post-treatment process. In addition, a modified four

ball machine under the identical tribological conditions of contact stress, configuration, and lubrication was also used for rolling contact failure tests. The results of the study indicated that the possibility to achieve a fatigue life in excess of 70 million stress cycles without failure in relatively thin (50 μ m) cermet coatings through increasing the furnace temperature to 1200 °C with maintaining the full film lubrication was feasible. As a result of cyclic loading, shear stress occurring in either at the coating substrate interface or within the coating microstructure was considered coating failure in the experiment [40].

Hernandez et al [41] investigated fatigue properties of a 4340 steel coated with a Colmonoy 88 deposit by HVOF spraying facility. They found a decrease in the fatigue strength of both coated and non-coated surfaces related to existence of Al_2O_3 particles penetrated during grit blasting as became stress concentrators that enhanced the multiple nucleations of fatigue cracks. However, in case of coated substrate, results revealed further fatigue strength reduction as attributed to the partial fracture and detachment of the coating from the substrate along the substrate deposit interface. This indicated control of the deposit thickness of HVOF as it could endure the stress applied to the material [41, 42].

Producing an amorphous and nanocrystalline structure using the HVOF spray facility was investigated and evaluated for various spraying conditions [43]. The study showed an ability to attain amorphous coating from the FeNb powder while adjusting the spraying conditions. Crystalline deposit was formed in all cases of microcrystalline and nanocrystalline powders whenever using silicon-iron powder was used. However, considerable addition of boron was suggested in the study to bring amorphous phase in the silicon-iron alloy. Boron in Fe₃Si alloy with variation of quantity added indeed showed the ability to produce amorphous phase with appearance of increase or decrease the nanocrystalline phase [43].

Toma et al. [44] studied the microstructure and photocatalytic properties of nanostructured TiO₂ and TiO₂-Al coatings applied by HVOF spraying in two different methods. They were internal injection, as in a conventional HVOF system, and external injection at the exit of the torch nozzle. In general, a lamellar structure would be observed in thermally sprayed coatings that prepared by standard HVOF spraying process. Specific structure with a high ratio of non-melted particles and significant amount of anatase phase was obtained in the deposits by

external injection of the powder feedstock system. They found that the external injection method used was exhibited better photocatalytic activity compared to conventional HVOF method. They also found a significant enhancement of photocatalytic activity if aluminum particles were added to TiO_2 powders. Moreover, the HVOF TiO_2 coating containing certain amount of rutile phase showed a better photocatalytic performance [45]. Lee et al. [46] investigated the effect of heat treatment on the microstructure and properties of HVOF-sprayed Ni-Cr-W-Mo-B alloy coatings. They showed as-sprayed coatings induced a localized corrosion if metastable and heterogeneous phases such as amorphous, nanocrystalline and very refined grain crystals and precipitates are exist in the coating. Increased of microstructural and chemical homogeneity such as the reduction of porosity, densification, and reduction of the eutectic phase was found to be affected by the increase of annealing temperature which in turn would enhance corrosion resistance.

Adhesion of thermal sprayed coating to a substrate material has been a primary concern to engineers since thermal spray processes were introduced to various industries. This was because of the process, which could not be effectively employed for engineering applications if the coating did not bond well to a substrate interface. Therefore,

investigation on the bonding mechanisms at coating-substrate interface has received considerable attention in thermal spray technology [47-49]. For a conventional spraying process with spray particle at a relatively low velocity, the adhesion between the coating and the substrate primarily depends on the mechanical interlocking, which is mainly related to the substrate surface roughness and the solidification of impacting droplets. However, diffusion processes might occur due to the high temperature of the substrate when vacuum plasma spray or low pressure plasma spray technology was used to deposit a coating [50-51]. As far as the mechanical interlocking effect was concerned, the adhesive strength of coating sprayed by the conventional thermal spraying processes was increased with the improvement in the melting state of spraying particles and the increase in roughness of substrate surface [22, 52-55]. However, Li et al. [56] proved that no significant effect in the adhesive strength of HVOF WC cermet coatings in which they exceeded the strength of the adhesives used approx. 65 MPa was observed as compared to others such as Cr_3C_2 -25NiCr and Al_2O_3 -Ni. Subsequently, other researchers linked the bond strength with mass of solid phase in a spray particle with excluding the effect of the conventional state parameters of a spray particle, i.e., temperature, velocity, and momentum. With the result attained, insurance of high bond strength of

HVOF coating besides the solid–liquid two-phase condition was requiring high density of non-melting phases in a solid–liquid two-phase droplet [19].

From corrosion point of view through electrochemical behaviour, different types of HVOF coatings on steel were examined. Observations indicated that spraying parameters was playing a major rule in influencing the corrosion behaviour of the sample surfaces. The electrochemical behaviour of HVOF coatings was strongly affected by porosity, the presence of micro- and macro-cracks, and also of unmelted particles. Once the electrolyte reached the substrate material via these defects, the galvanic pair formed between the coating and substrate resulting in accelerated corrosion leading to the depletion of the coating. Moreover, Inconel 625 is found to be more resistant to corrosion compared with 316L steel coating, if electrochemical testing was carried out using a sea water [4, 57]. The formation of oxides in the splats exhibited better avoidance of corrosion solution to approach the substrate surface. However, possible effects of higher oxides in the lamella type microstructure were representing low tensile bond strength as attributed to the discontinuity of coating structure [58]. Exposure to thermal cycling was found significantly affecting to some Ni-Cr

coatings accompanied with aging. As a matter of fact, adhesive strength was reduced and coating delaminated indicated the limit of integrity and protection of using these coating on boiler components against steam oxidation [59]. Moreover, the hot corrosion behaviour of HVOF NiCrAl coating on superalloys was investigated by Mahesh et al. [60]. They performed mass gain measurements after each cycle to establish the kinetics of corrosion using the thermogravimetric technique. They showed that the bare superalloys experienced higher weight gain and the formation of oxides and spinels of nickel, chromium, and aluminium contributed to hot corrosion resistance of the coating. Corrosion resistance of WC based cermets coatings produced by HVOF spraying was studied by Aw et al. [61]. They performed polarization and electrochemical impedance spectroscopy on both uncoated and coated workpieces, which were immersed in 3% NaCl solution prior to spectroscopic analysis. They demonstrated that the nickel binder in the WC-17Ni coating had a better corrosion resistance than the cobalt binder in the WC-17Co coating.

Important concerns other than corrosion were erosion and weight loss through abrasion and impingement. In this case, WC-Co was hard metal and introduced through HVOF spraying on the top of components while

some others employed sintering material. The re-melting surfaces were, then, tested by microscale abrasion that occurred predominantly by preferential removal of the binder phase followed by pullout of the carbide. It was observed that the binder phase removal was accelerated by corrosion in acid media [62]. Chen et al. [63] were carried out experiments on applying WC–Co coatings produced by HVOF spraying from two different feedstock powders, one with a conventionally sized WC grains and one with nanoscale WC grains. It was found that under conditions of micro-scale abrasion, the fine WC grain size in the nanostructured material resulted in rapid pullout of the hard phase and thus to high wear rates [63]. HVOF coatings were applied on to three different metallic surfaces, which they were plain stainless steel, spot-welded stainless steel, and a composite surface of stainless steel and carbon steel welding. After impingement test, it was found that the coating over both spot-welded and plain stainless steel surfaces exhibited a similar degree of weight loss. However, the coating on the composite surface experienced a greater degree of weight loss [64].

2.2 Material Characterization of Laser Treated HVOF Coatings

Laser surface treatment has been employed to enhance the bonding of coating to the substrate material through reduction in porosity and crack

formation. This required the selection of appropriate parameters resulting in uniform coating onto the substrate during melting and solidification process. In addition, formation of the metal matrix composition (MMC) at low porosity and oxides is one of the main targets for many researchers in order to expose the effect of different parameters on the re-melting of the coating. The formation of high performance of MMC layers whether by HVOF or by laser techniques or both together could improve adhesion, wear resistance, temperature resistance and corrosion prevention on the surfaces. However, the metallurgical changes occurred during the melting, and the main constituents of the coating could be retained with quenching.

Pang et al. [65] utilized laser surface alloying of Mo, WC and Mo-WC metal matrix composite on Ti6Al4V alloy. They found that the solubility levels of hard particles could be varied through changing the laser output power level. They observed different weight percentage content of WC lead to variation in wear and hardness proportionally. Moreover, it could reduce the hardness and increase the wear resistance compared with HVOF coating due to reduction of carbide and could increase in bonding to prevent layer lamination [63]. The dendritic growth around WC particle was required and it could be achieved with the selection of proper processing parameters. It, then, could produce pores free coating

with good bonding, good corrosion resistance, and wear resistance simultaneously [66]. The elastic limit of coating was found to be reduced after the laser treatment of Inconel 625 HVOF coating and the defect sites at coating base material interface were the origin of the crack sites. Moreover, some locally distributed splats with high oxygen content were also act as crack initiation centers [67]. This indicates that many factors could lead to crack initiation in coating influencing the coating performance.

Laser re-melting of Ni-20Cr and Stellite-6 powders coating was found to be effective in reducing the porosity less than 0.5% as compared to original plasma spray coating application of 2-4%. However, significant improvement in interfacial strength between the coating and substrate material was observed after the laser re-melting. It was also noticed from the early studies that almost no porosity and improved structural homogeneity occurred in the laser re-melted coating as compared with the plasma spraying [68]. The microhardness decreased after the laser re-melting as compared to the original coating hardness. This might be attributed to the internal stresses and disordered arrangement of atoms in the coated material [69].

The harmful effects of high-temperature oxidation, evaporation, melting, crystallization, residual stress, gas release, and other common problems of traditional thermal spray methods could be avoided by means of new emerging a recent technique called the cold spray process. The coating is formed by high-velocity particles impacting on the substrate to be coated. The particles are accelerated by a jet of compressed air whose temperature is always lower than the melting temperature of the material being sprayed, and the coating is formed by particles in the solid state. These particles bond mechanically with the substrate by way of plastic deformation only. Application of laser treated coatings had exhibited a high density and high particle bonding strength [70].

It was reported [71] that the sliding wear resistance of a plasma-sprayed WC-17 wt.% Co coating was improved following laser re-melting by factors between 1.5 and 8 depending upon the test conditions due to a reduction in porosity. A similar result was also observed in the study of laser re-melted plasma-sprayed Cr₂C₃-25 wt.% NiCr [72]. In addition, Liang et al. [73] demonstrated that laser surface re-melting of plasma-sprayed WC-80NiCrBSi coatings also increased their hardness and sliding wear resistance. However, it was also reported [63] that following laser re-melting of HVOF-sprayed conventional and

nanostructured WC-12 wt.% Co coatings, the hardness and wear resistance of both coating types were significantly reduced, with the nano-scale coating exhibiting a slightly lower wear rate than its conventional counterpart. It is explained in the reference [63] that the reduced wear resistance of the conventional coating as a result of laser re-melting may be attributed to the cracking and porosity, which is always present in the CO₂ laser treatment. Moreover, the carbides within the laser re-melted coating were either reduced in size or severely cracked, these attributes would allow easy pull-out of the carbides in the micro-scale abrasion test and thus to reduce wear resistance. Up to date, there have been very limited studies considering corrosion performance of laser re-melting on thermal sprayed composite coatings. Tuominen et al. [74] reported that laser re-melting of HVOF-sprayed Inconel 625 coatings resulted in homogenization of the sprayed structure, leading to improvement in resistance to wet corrosion and high temperature corrosion. In addition, laser re-melting of HVOF sprayed Ni-45Cr and Cr₃C₂-20 wt.% NiCr coatings [75] showed good corrosion resistance in a short-term and high-temperature environment. So far, no work has been reported on the effect of laser re-melting of WC MMC HVOF-sprayed coatings on corrosion performance, although substantial effects have been made on laser direct deposition, such as laser cladding and

laser melt/particle injection, of various WC composite coatings [67,76-78].

Laser heating of HVOF coating and thermally sealing of the coating surface were investigated by Oksa et al. [75]. They showed that the thermal sealing provided good corrosion resistance of the surface in short-term tests. The laser assisted spraying and the laser treatment of thermally sprayed coating was studied by Suutala et al. [79]. They indicated that the cracks perpendicular to the processing direction were observed when using the Nd:YAG laser; however, this situation was improved when the diode laser was used. The adhesion testing of the thermally sprayed and the laser deposited coatings was carried out by Hjornhede and Nylund [80]. They suggested that the delamination mechanism was the initial formation of a radial crack in the coating after which the coating/substrate interface came under increased tension load and fractures. The influence of laser melting on morphology, composition, and microhardness of the thermally sprayed coatings was investigated by Kumari et al. [81]. They showed that the microhardness increased by the post deposition treatment; however, the extent of increase depended on the laser scanning speed and the coating composition. Yilbas et al. [67] investigated HVOF coating and the laser

treatment process. They showed that the elastic limit of the coated workpiece after the laser treatment reduced slightly.

2.3 Modelling of HVOF Coatings

Bansal et al [82] applied finite element modelling for the fracture behaviour of brittle coatings to assess the experimental results carried out by the others. They demonstrated that the finite element analysis could provide the information on the effects of various coating parameters for understanding the mechanical response of coatings under bending loads. Moreover, the residual stress modelling and predictions in HVOF coating was carried out by Bansal et al. [83]. They used a hybrid non-linear explicit-implicit finite element analysis to model the thermomechanical process developed during the thermal spraying. The researchers [84-85] previously proved, in some extent that the result of modelling can be set as a basis for the formulation of parameters in HVOF coating process. In practice, modelling and analysis were carried out for HVOF thermal spray process and demonstrated systematic characterization in representing the influence of controllable process variables such as combustion chamber pressure, oxygen/fuel ratio. The effect of powder size distribution on the particle velocity and temperature at the point of impact on substrate was also demonstrated in

the model study [84-85]. However, Sysweld software used to calculate the residual stresses in HVOF thermal sprayings showed inconsistency with the experimental observations as attributed to low memory capacity simplified two-dimensional model of the program compared with proposed application of improved three dimensional calculation model instead [86].

2.4 Summary of Literature Review

Residual stress, variation of fatigue strength, corrosion and erosion resistance in relation to HVOF-sprayed Inconel 625 coatings are found to be important, which in general, depend on the coating process parameter. The information related to HVOF coating properties, that introduced in the literature have attributed to the observations of researchers through experiments studies. This provided the understanding of the complexities accomplishing a high quality HVOF coating to all deficiencies. On the other hand, post heat-treatment application on metal matrix composite (MMC) coatings were targeted to improve the coating corrosion resistance and other mechanical properties by reducing the composition gradient between the matrix and the hard phase through promoting some inter-diffusion in the coating. Laser surface treatment is an option owing to its unique features over

conventional heat-treatments, such as its capabilities of precise control of treatment depth with or without melting. The resultant microstructural homogenization, such as modifying of splat-structure through control melting and porosity, reduction of compositional gradient between the hard phase and the matrix, and improvement of adhesion bonding between coating and substrate, can be readily achieved to improve coating properties. Up to now, most of the previous work on laser surface treatment of HVOF thermal sprayed coatings has been concentrated on attempts to improve their hardness and wear resistance. The metallurgical changes after laser treatment process were not examined in detail. In addition, blending of spraying powder with hard particles influences the metallurgical changes in the coating and modifies the residual stress levels in the coating. In the previous studies, the mechanical properties were the focused research area and the metallurgical changes as well as the residual stress levels were not deeply examined. The open literature review shows that there is a gap in the knowledge on aspects of laser treated HVOF coatings and assessment of performance of such treated coatings. Consequently, the main objective of this thesis has been focused on determining the metallurgical changes, residual stress levels, and corrosion response

prior and after the laser treated HVOF coatings consisting of Inconel 625 and WC particles at different weight ratios.

Chapter 3 - Experimental Equipment & Procedures

3.0 Introduction

Experiments are carried out to examine metallurgical, topological, and corrosion properties of HVOF coating of diamalloy 1005 with and without level of WC powders onto stainless steel (304). The experiment carried out include sample preparation, HVOF coating, laser re-melting, measurement of residual stress, and fracture toughness. With laser re-melting of the coating that had been carried out, the effect of WC content on the residual stress formation in the coating is examined. XRD technique is used to measure the residual stress in the coating with and without WC content. The indentation tests are carried out to measure the Young's modulus and fracture toughness of the coating with and without WC content also. The microstructural characterization and surface morphology of the coating after laser re-melting are carried out using SEM, EDS and optical microscopy. In addition, corrosion tests are conducted for laser re-melted samples.

3.1 Specimen Design

Stainless steel 304 is selected in this experiment due to its widely used in industry such as Saudi Arabian Basic Industrial Company (SABIC). Stainless steel 304 has low toughness and low to high temperature resistance with highly affected by sensitization as the precipitation of chromium, which take place during welding. In addition, exposure to high temperature will make material prone to reduction of corrosion resistance due to chromium depletion. Therefore, application of HVOF coating of diamalloy 1005 with and without level of WC particles re-melted by laser beam is considered to improve metallurgical and surface properties.

The geometry of the substrate material workpieces were cut and mounted on a holding plate. The workpieces were located close to each to attain uniform thermal spray (HVOF) coating in terms of layer thickness as shown in Figure 3.1. The samples were prepared by Applied Surface Technology Ltd. [87-89]. However, coated samples received from Applied Surface Technology Ltd. [87-89] were cut and prepared for examination. Figure 3.2 demonstrates the cutting machine type, "Brilliant 220" made by ATA in Germany applied to sectioned coated samples by using a CBN slitting wheel [87].

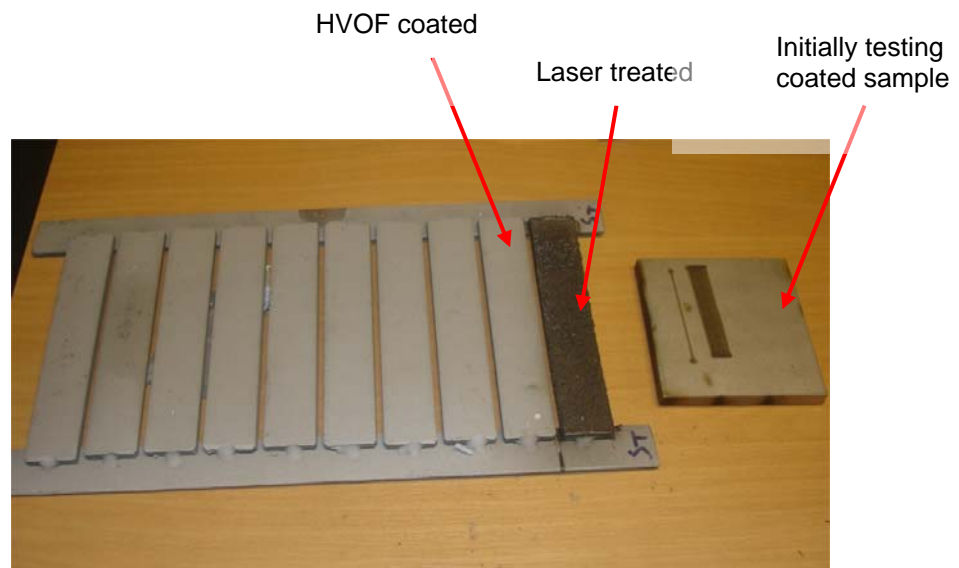


Figure 3.1. The workpieces were located close to each other to attain uniform thermal spraying.



Figure 3.2. Cutting Machine used to section the coated samples [87].

3.2 Surface Preparation

The steps for surface preparation of the workpieces are given below.

3.2.1 Grit Blasting

Samples were grit blasted by Applied Surface Technology Ltd. [88]. Grit blasting provided a clean and a rough surface to enhance the adhesion of coating and to remove any contaminations that restrain the bonding with possible forms uneven surface profile. The specimens were grit blasted with 20 mesh Alumina particles at 40 – 45 psi pressure to roughen the surface followed by cleaning by compressed air prior HVOF thermal spraying. Figure 3.3 illustrates the grit blasting machine [88].



Figure 3.3. Enviraclean grit blasting machine used to clean and rough on the specimens surfaces [88].

3.2.2 Sample Mounting

The metallographic samples for coating structure evaluation are cut from section of specimens and mounted using automatic mounting press manufactured by BUEHLER. All the samples were sectioned and mounted. Grinding was performed using different grades of sandpapers and polishing was carried out using diamond suspensions on well-lubricated sintered metallic disc. Final polishing was carried out to 0.25 μ m of diamond suspensions. Samples were electrochemically etched a mix of 15 mL HCl – 10 mL acetic acid – 10 mL nitric acid in order to reveal microstructure.

3.3 HVOF Thermal Spraying Process

The thermal spray process and the powder used are given below.

3.3.1 HVOF Coating Powder

The aim of using Inconel 625 powder and tungsten carbide WC is to increase the wear resistance by the addition of wear resistant phases in which afterward to be subjected to laser treatment for assessment and evaluation against HVOF. Various compositions of Inconel 625 were blended with tungsten carbide, and the resultant coatings were assessed

to establish the microstructural and morphological changes prior and after the laser re-melting process.

Table 3.1. Chemical composition and size of HVOF powder (Inconel 625 & WC)

Powder Material	Chemical composition				Powder Size Microns
Inconel 625 powder	Fe	Mo	Cr	Ni	22 to 53
	5	9	21	Balance	
Tungsten Carbide WC Spec HV.CA04	Co	Cr	WC		15 to 45
	10	4	Balance		

3.3.2 HVOF and Laser Equipment

HVOF spraying was carried out using the JP-5000 unit by Applied Surface Technology Ltd. as shown in Figure 3.4[89]. The coating layer thickness of approximately 300 μ m was achieved. The spraying parameters are given in Table 3.2. Some of coated samples were laser treated.

Table 3.2. Process parameters of HVOF thermal spray.

Oxygen Pressure (kPa)	Fuel Pressure (kPa)	Air Pressure (kPa)	Powder Feed Rate (m ³ /h)	Spray Rate (Kg/h)	Spray Distance (m)	WC %
1023	590	720	0.85	6.5	0.28	0 %, 9.3% and 47%

The Rofin DC 020 (Diffusion-cooled Slab CO₂) CO₂ laser equipment was used to irradiate the surface of coated samples as shown in Figure 3.5. The laser was operated at HF excitations giving the nominal output power of 2000 W. The beam quality factor for this equipment is to be considered as $k > 0.9$ and the pulse frequency is 0 or 2 up to 5000 Hz; cw. The temporal distribution of the laser output power intensity was in the repetitive pulses form of 5 ns nominal pulse length. The traverse speed of the samples was 10 mm/s during the laser scanning. The laser spot size at the sample surface was set as 1.2 mm and the overlap tracks were developed during the laser processing. The overlap ratio was kept as 40% to cover the large area of the irradiated surface. Argon was used as a shielding gas during the processing to reduce the oxidation of the irradiated surface.

The laser diode was also used to irradiate the coating surface. The samples re-melted by the diode laser were only used for corrosion experiments. A Laser line 160–1500 LDL 1.5 kW diode laser Figure 3.6, with a rectangular beam size of $2.5\text{ mm} \times 3.5\text{ mm}$, having a uniform power density distribution, and mixed wavelengths of 808 and 940 nm with beam delivery: 5 m optical fibre (1000 micron) or direct beam, were the specification of the equipment used in this study. In order to reduce/eliminate oxidation induced in the laser processes, samples to be treated were placed in a hermetic box with a Perspex cover, which is transparent to the laser beam, on the top. Before laser processing, the box was purged by argon gas for at least 20 min to remove/minimize the oxygen and other gases. The laser power was varied from 350 W to 800 W, whereas the scanning velocities were varied from 5 mm/s to 40 mm/s. Overlap ratio was 50%.

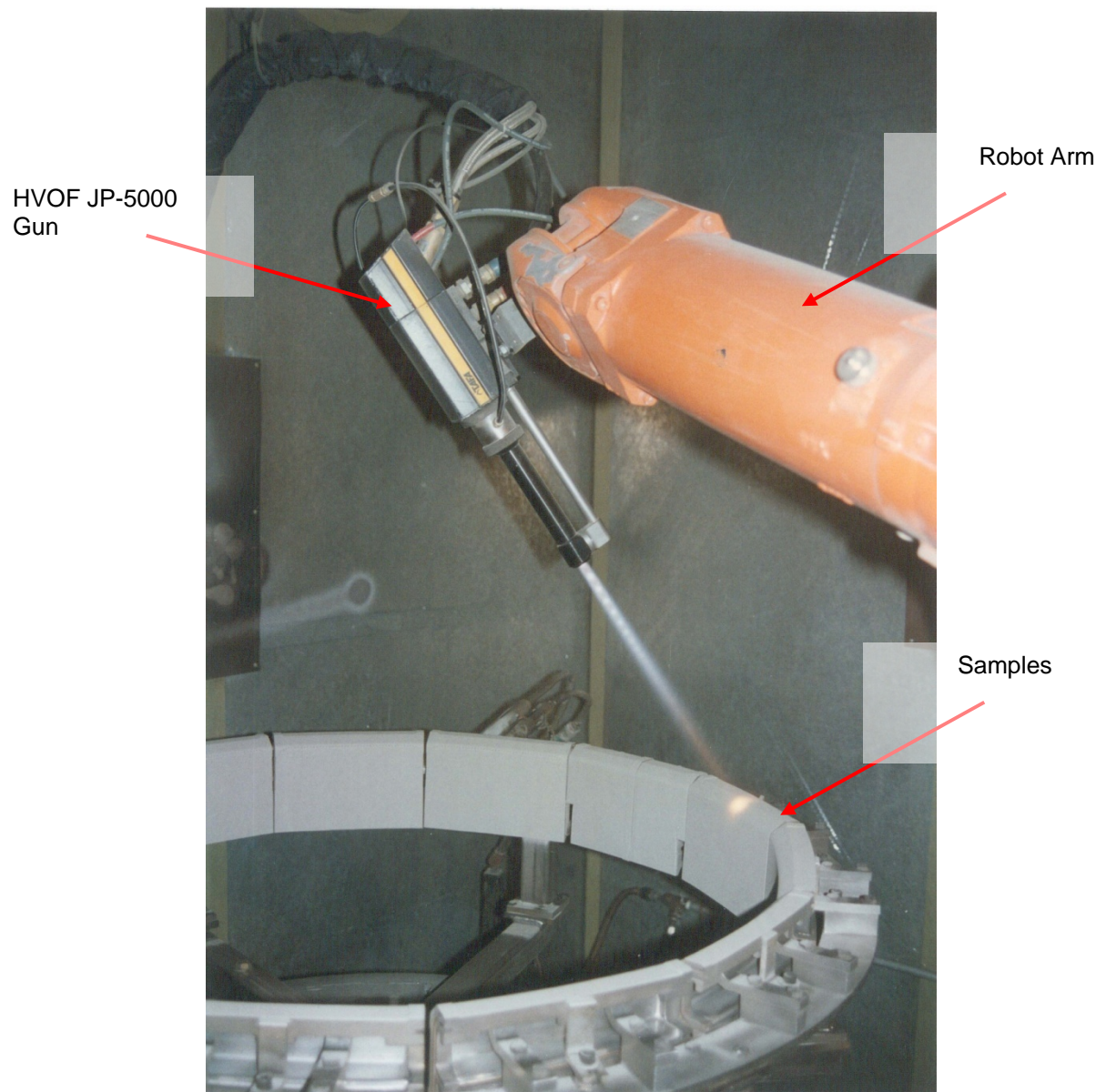


Figure 3.4. HVOF JP-5000 unit used in spraying Inconel 625 with and without WC inclusion [89].

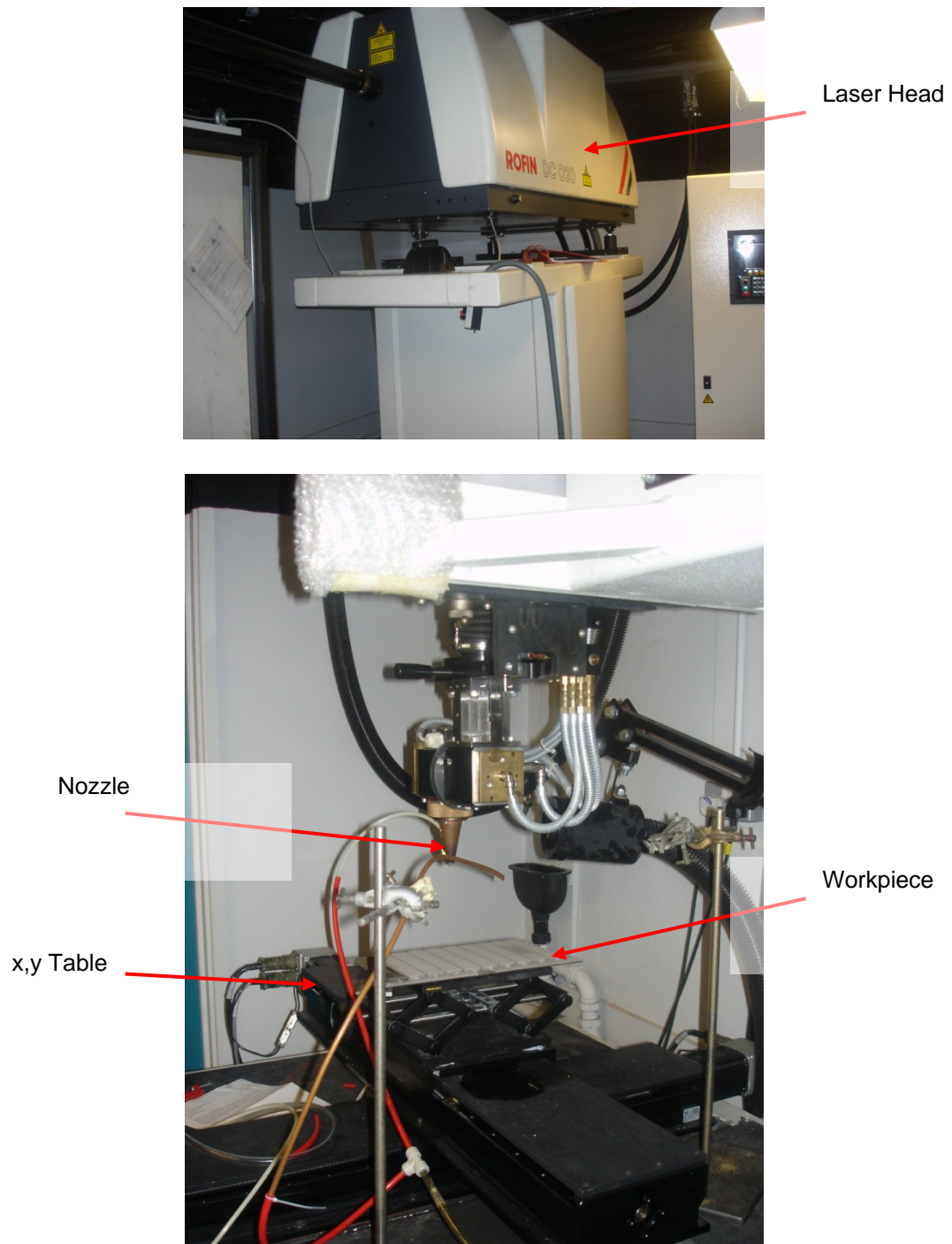
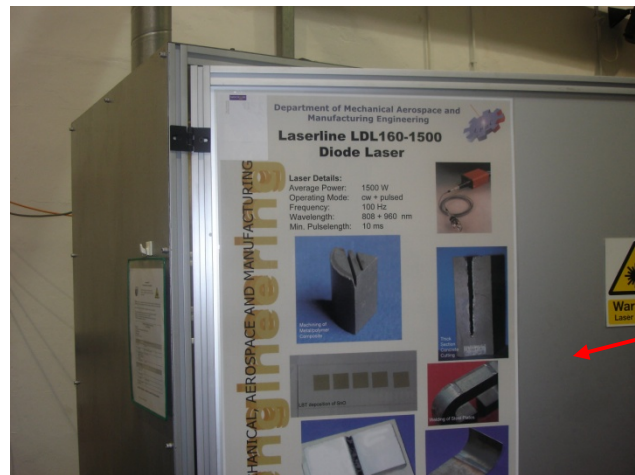
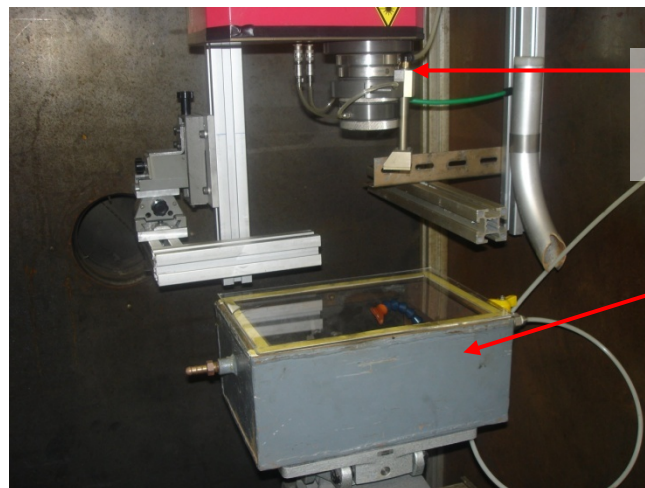
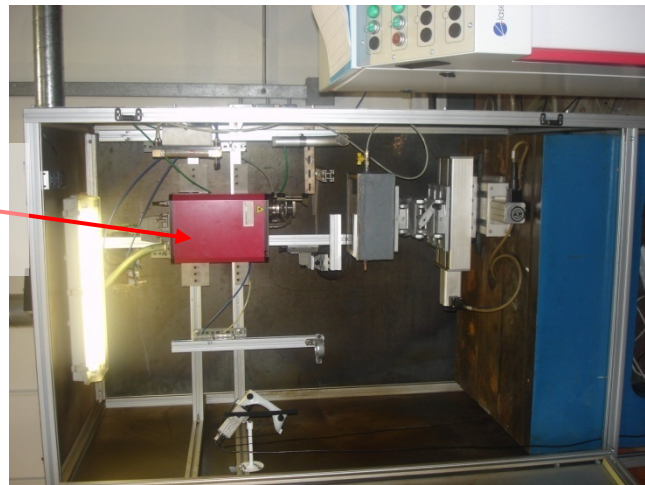


Figure 3.5. Rofin DC 020 (Diffusion-cooled Slab CO₂) CO₂ laser equipment.



Laser Power Supply

Laser Head



Focusing Lens

Workpiece Holder

Figure 3.6. A Laser line 160–1500 LDL 1.5 kW diode laser.

3.4 Characterization Tests

The tests carried out for the characterization of the coating are given below.

3.4.1 Potentiodynamic Anodic Polarization

Corrosion behaviour was assessed by potentiodynamic anodic polarization in deaerated 3.5% NaCl at 24 °C. The samples were immersed in the solution for 50 min to stabilize the open circuit potential (E_{corr}). Anodic polarization curves were determined at a scan rate of 15 mV/min, using a Gill ACM computer controlled potentiostat and a conventional three-electrode cell employing a platinized titanium counter electrode and a saturated calomel reference electrode (SCE). Purging the nitrogen was continued throughout the tests. Values of corrosion current density (i_{corr}), which is linked to the corrosion rate through application of Faraday's law, were determined by the TAFEL extrapolation technique.

3.4.2 SEM & EDS and Optical Microscope

JEOL JDX-3530 scanning electron microscope (SEM) was used to obtain photomicrographs of the cross-sections and surface of the

workpieces prior and after the tests while energy dispersive spectroscopy (EDS) was accommodated for the elemental analysis. JEOL JDX 3530 LV has specifications of resolution 3.0 nm, accelerating voltage 03 to 30 kV, and magnification x5 to 300,000. The equipment is shown in Figure 3.7.

The optical microscope, which is used in this study, is manufactured by Olympus as shown in Figure 3.8. It is Olympus BX 60 optical has Polaroid digital microscope camera (DMC). It is used for microscopic observations and to obtain optical micrographs of the surface. The microscope has a revolving nosepiece with 5 objective lenses of various magnifications attached to it. The magnifications levels are 50X, 100X, 200X, 500X and 1000X.

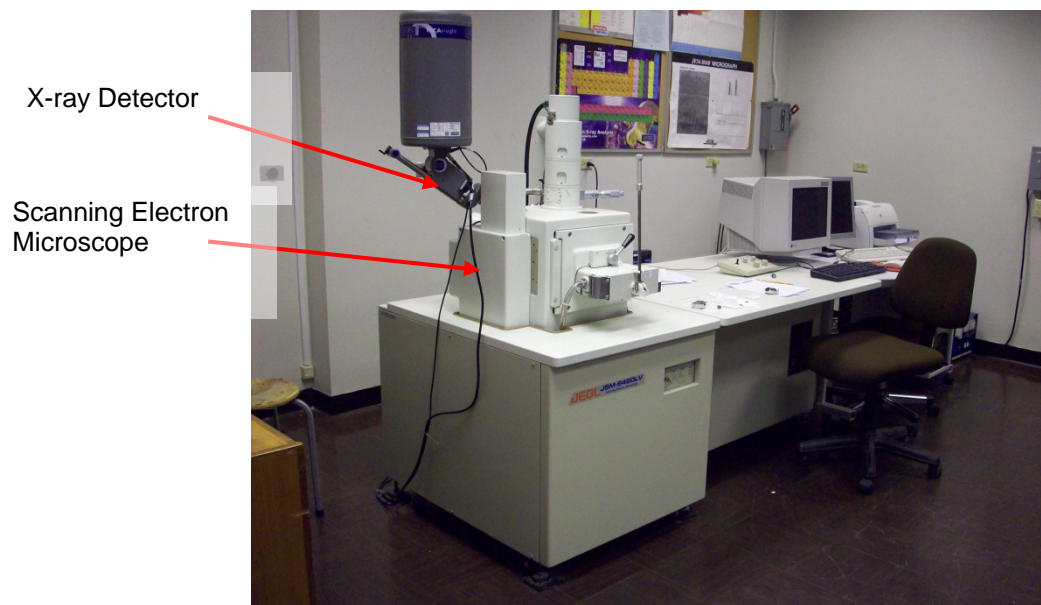


Figure 3.7. Scanning Electron Microscope model JEOL JDX 3530 LV.

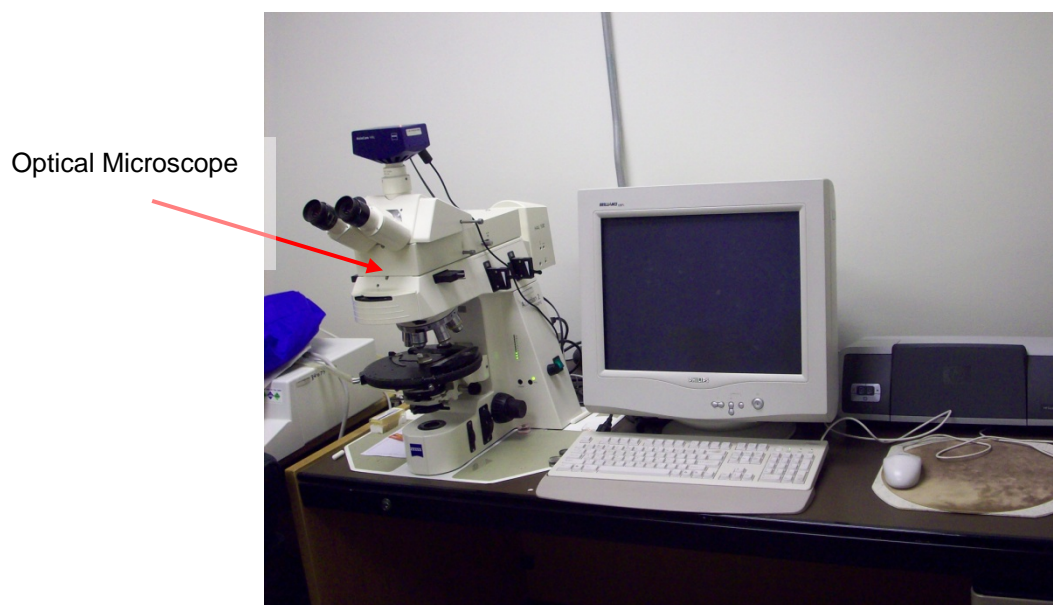


Figure 3.8. Olympus BX 60 optical microscope with Polaroid digital microscope camera (DMC).

3.4.3 X-Ray Diffraction (XRD)

The Bruker D8 Advance having Mo-K α radiation is used for XRD analysis. A typical setting of XRD was 40 kV and 30 mA. It should be noted that the residual stress measured using the XRD technique provided the data in the surface region of the specimens. This was because of the penetration depth of Mo-K α radiation into the coating, i.e. the penetration depth was in the order of 10 – 20 μm . the detailed specification and picture are is allustrated in Table 3.3 and Figure 3.9 respectively.

Table 3.3. X-Ray Diffraction machine specifications

Model	AXS D8 Bruker Inc
Sample Positioning & Rotation	Goniometer; Eulerian Cradle; Theta-Theta, Thet-2Theta
X-Ray Source & Optics	Collimeter or slits to reduce angular divergence in the incident beam
Performance Specifications	<ul style="list-style-type: none">• 2-Theta Angular Range (degree) – 110 to 168• Peak Count Rate (cps) 2.00E6• Max Sample Dia (mm) 600• Computer based interface and dispaly; Othe digital or analog interface or display; Ability to process and analyze the diffraction data

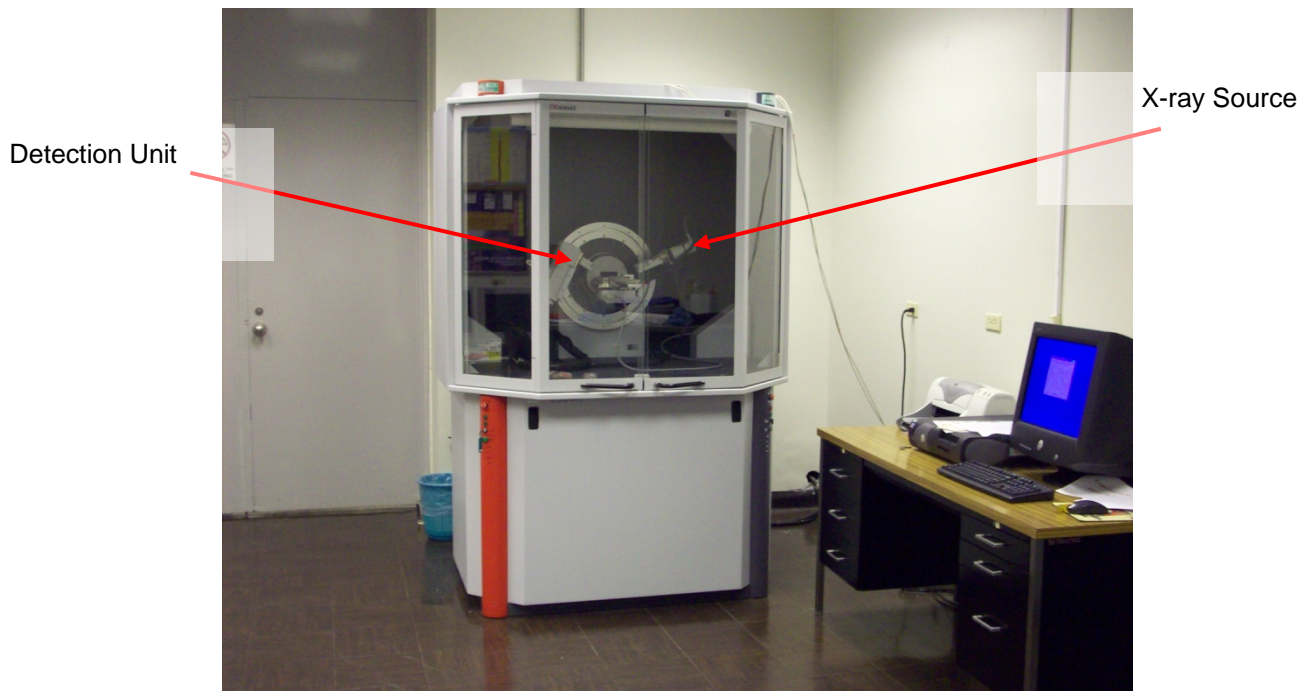


Figure 3.9. X-Ray Diffraction machine model AXS D8 Bruker Inc.

3.4.4 Indentation Tests and Fraction Toughness Measurement

The indentation tests were performed by the Indentation Hardness Tester manufactured by BUEHLER Com as shown in Figure 3.10. The fraction toughness of the surface was measured using the indenter test data for microhardness (Vickers) and crack inhibiting. In this case, microhardness in HV and the crack length generated due to indentation at the surface were measured using 20 N load level. Moreover, in order to visualize the cracks formed around the indentation mark, an optical microscopy was performed. The indentation tests were carried out at 20

locations at the laser treated surface to secure the data uniformity and repeatability of the tests.

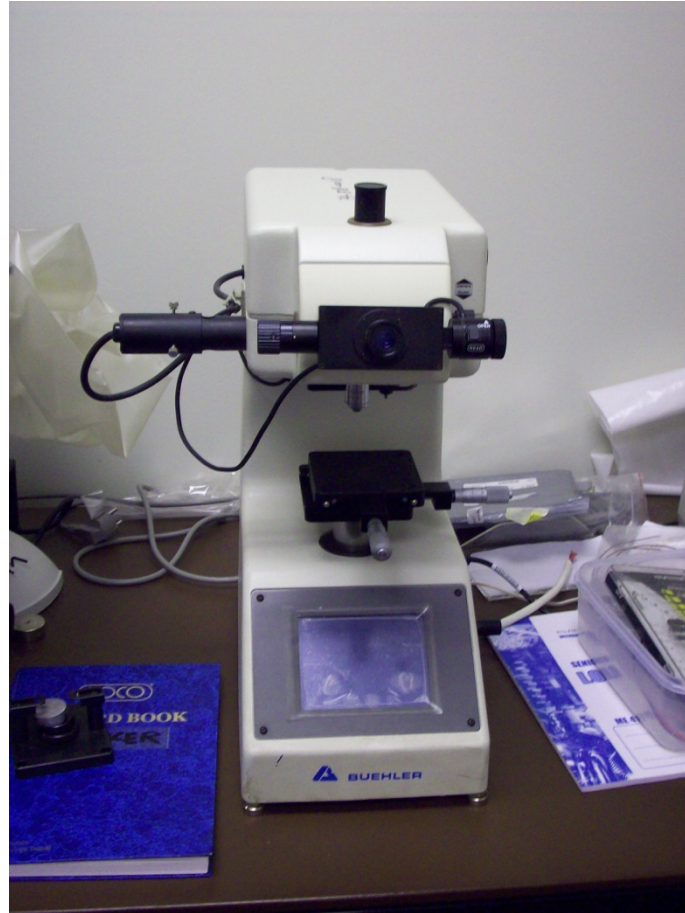


Figure 3.10. The indentation testing BUEHLER machine used to get fraction toughness of the surface.

3.5. The XRD Technique for Residual Stress Measurement

The measurement relies on the stresses in fine grained polycrystalline structure. The position of the diffraction peak undergoes shifting as the

specimen is rotated by an angle ψ . The magnitude of the shift is related to the magnitude of the residual stress. The relationship between the peak shift and the residual stress (σ) is given [90]:

$$\sigma = \frac{E}{(1+\nu)\sin^2\psi} \frac{(d_n - d_o)}{d_o} \quad (1)$$

where E is Young's modulus, ν is Poisson's ratio, ψ is the tilt angle, and d_i are the d spacing measured at each tilt angle. If there are no shear strains present in the specimen, the d spacing changes linearly with $\sin^2\psi$.

3.5.1 Analytical Expression for the Residual Stress

The analytical expression for the residual stress was developed previously [27]. The previous expression is based on the thermal expansion mismatched between the coating and the base material. Therefore, the residual stress is:

$$\sigma = \frac{[E_c(T_f - T_R)(\alpha_c - \alpha_s)]}{1 + 2\left(\frac{E_c t_c}{E_s t_s}\right)} \quad (2)$$

where E_c and E_s are the elastic modules of the coating and the base material, t_c and t_s are the coating and base material thicknesses, T_f is the maximum temperature during laser heating and T_R is the room temperature after the cooling period is over, α_c and α_s are the thermal expansion coefficient of the coating and the base material, respectively. Table 3.4 gives the data used for the residual stress calculation using equation (2). It should be noted that the properties used in the table are estimated using the mass average method.

Table 3.4. Properties of the coating material used in equation (2)

	E_c (GPa)	E_s (GPa)	t_s (m)	t_c (m)	α_c (1/K) $\times 10^{-6}$	α_s (1/K) $\times 10^{-6}$	T_R (K)
0% WC	208	210	3×10^{-3}	3×10^{-4}	13.1	15	300
9.3 % WC	225	210	3×10^{-3}	3×10^{-4}	12.36	15	300
47% WC	424	210	3×10^{-3}	3×10^{-4}	12.36	15	300

3.5.2 Determination of Young's Modulus and Fracture Toughness by Indentation Test

The elastic response of the surface when subjected to indentation test, needs to be examined through which the Young's modulus can be

determined. After considering Figure 3.11, the Young's modulus can be formulated as [91]:

$$E^* = \left(\frac{9}{16}\right)^{0.5} P.h^{-1.5} .R^{-0.5} \quad (3)$$

where P is the applied load, h is the elastic penetration of the indenter, and R is the indenter radius. The true modulus of elasticity can be determined using the indenter properties [92], i.e.:

$$E = \frac{1 - \nu^2}{\frac{1}{E^*} - \frac{(1 - \nu_i^2)}{E_i}} \quad (4)$$

where E_i and ν_i are the Young's modulus and Poisson's ratio of indenter, respectively. In the calculations $E_i = 1141$ GPa and $\nu_i = 0.07$ (diamond indenter), and $\nu = 0.24$ are taken [91].

The fracture toughness of the surface is measured using the indenter test data for microhardness (Vickers) and crack inhibiting. In this case, microhardness in HV and the crack length generated due to indentation at the surface are measured. The lengths of the cracks, which are generated due to indentation at the surface are measured. The length (l) measured corresponded to the distance from the crack tip to the indent. The crack lengths (l) were individually summed to obtain $\sum l$ as described in the previous study [93]. The crack length (c) from the

center of the indent is the sum of individual crack lengths ($\sum l$) and half the indent diagonal length ($2a$). Therefore, $c = a + \sum l$ [93]. However, depending upon the ratio of $\frac{c}{a}$, various equations were developed to estimate the fracture toughness (K). However, the equation proposed by Evans and Davis [94] and Anstis et al [95] has limitations due to nonlinearity of the coefficients for values of $\frac{c}{a} < 2$, which has not case for the HVOF coatings ($\approx 0.8 - 1.5$). Therefore, the equation proposed by Evans and Wilshaw [96] is used to determine the fracture toughness (K), which is applicable for ($0.6 \leq \frac{c}{a} \leq 4.5$ [93]), i.e.:

$$K_c = 0.079 \left(\frac{P}{a} \right)^{3/2} \cdot \log(4.5P \frac{a}{c}) \quad (5)$$

where P is the applied load on indenter, c is the crack length, and a is the half indent diagonal length. The data used for the calculations are given in Table 3.5. Moreover, in order to visualize the cracks formed around the indentation mark, top surface of coating is grinded slightly.

Table 3.5. Data obtained after indentation tests. The error estimated based on the repeats of the indentation test is 7%.

	Fracture Toughness ($\text{MN/m}^{3/2}$)	E (GPa)	H		P (N)	l $\times 10^{-6}$ (m)
0%WC	7.5	208	500 (HV)	4.904 (GPa)	20	40
9.3%WC	8.5	250	550 (HV)	5.394 (GPa)	20	38
47%WC	9.21	424	600 (HV)	5.884 (GPa)	20	36

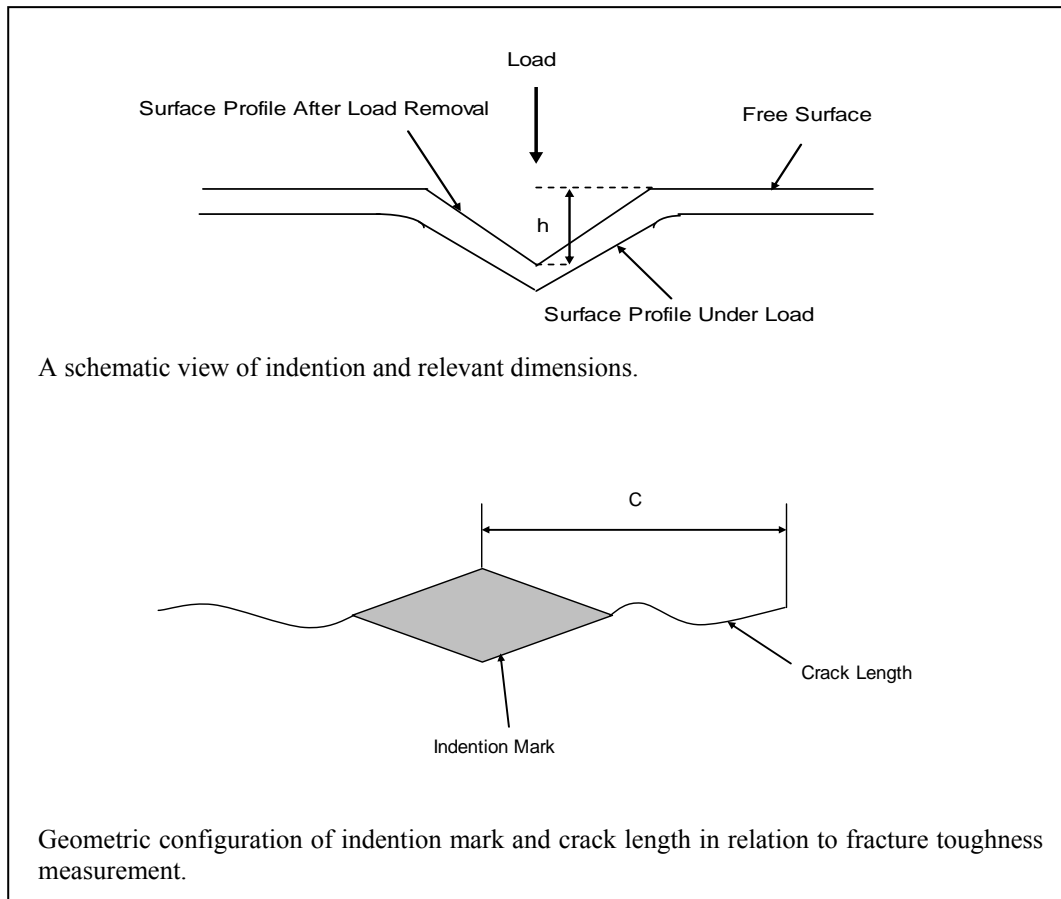


Figure 3.11. The indentation geometry used in the calculations.

Chapter 4 – Mathematical Analysis

4.0 Introduction

Laser heating and re-melting of coating is modeled using lump parameter technique while temperature distribution using the laser heating process is formulated through solving the heat transfer equation. In the lump parameter technique, energy balance in the coating is considered during the heating process and molten front velocity is derived using the Navier-Stokes equations. The solution of the heat conduction equation for temperature distribution is achieved using the laplace transformation technique. Since the laser absorption depth is significantly small and the focused spot diameter of the laser beam at the coating surface is significantly small, one dimensional heating situation is considered in the heating analysis for temperature formulation, i.e. temperature gradient along the beam axis in the substrate material is much higher than along the radial direction.

4.1 Melt Depth Formulation

The influence of assisting gas including cooling and exothermic reaction contribution on the melting process needs to be modeled prior to droplet formulation. This is because of the fact that the liquid layer film and the liquid film velocity at liquid film-assisting gas interface should be determined including the assisting gas jet effect. In the case of oxygen as assisting gas, the exothermic reaction contributes to the energy transport process at the interface. Moreover, during the melting process, the assisting gas forms a boundary layer flow over the liquid film surface (molten metal surface) and heat transfer from liquid surface to boundary layer flow occurs, at assisting gas-liquid interface, since the assisting gas is at room temperature, and heat transfer from liquid surface to solid substrate occurs at liquid-solid interface. High temperature oxidation reaction (exothermic reaction during which metal oxides are formed) at the melt surface provides excess energy to the laser irradiated region during the machining operation. It should be noted that, in general, nitrogen is used as an assisting gas in laser machining operation; however, existing of oxygen in the air results in high temperature exothermic reactions taking place in the melting region. The species formed after the chemical reactions (product of exothermic reactions) contribute to the heat transfer taking place at gas-liquid interface. In this

case, heat transfer at the gas-liquid interface due to high temperature oxidation reaction can be described through the ratio of dimensionless heat transfer coefficients due to diffusion (C_{H_d}) and chemical reaction $-(C_{H_c})$, which was presented as [97]

$$\frac{C_{H_d}}{C_{H_c}} = \frac{\left[1 + B_1 \left(\frac{U_L}{U_e}\right)\right]^{Pr-1} - 1}{\left[1 + B_1 \left(\frac{U_L}{U_e}\right)\right]^{Sc-1} - 1} \quad (6)$$

where

$$B_1 = \frac{2(\rho U)_g}{\rho_e U_e C_f}$$

and Pr and Sc ($Sc = \frac{\nu}{D}$) , where ν is the thermal diffusivity and D is the diffusion coefficient) are turbulent Prandtl and Schmidt numbers, respectively. U_e is the gas jet velocity at the outer edge of the assisting gas boundary layer (free stream velocity). U_L is the liquid velocity at interface, and C_f is the skin friction coefficient. The rate of heat transfer (\dot{q}_c) per unit area of the molten metal excluding the cooling effect while including chemical reaction contribution of the assisting gas can be written as [97]:

$$\dot{q}_c = \rho_e U_e C_{H_c} \left[\left(\frac{C_{H_d}}{C_{H_c}} - 1 \right) h_c \right] \quad (7)$$

where U_e is the gas velocity and ρ_e is the gas density at the edge of the boundary layer, h_c is the chemical reaction enthalpy.

The ratio $\frac{C_{H_d}}{C_{H_c}}$ is dependent on Pr , Sc and B_l where Pr and Sc are constant [97].

The energy balance associated with the melting process can be simplified through investigating the melting process by lumped parameter technique. Therefore, it is considered that the melt layer generated flows steadily in the direction of the assisting gas due to the drag force developed at the assisting gas-liquid interface. Consider the melt layer generated at the solid surface during the steady laser heating process. Assume a small fraction (β) of molten metal evaporates from the surface at the assisting gas-melt interface during the laser heating process. The rate of energy required (\dot{E}_{req}) to generate a melt flow rate (\dot{m}_L) at the surface of the solid substrate can be written as:

$$\dot{E}_{req} = \dot{m}_L [Cp_s (T_m - T_i) + L_m + \beta L_{ev} + 1.65 Cp_m (T_{ev} - T_m)] \quad (8)$$

where T_i and T_m are initial and the melting temperatures of the solid substrate. L_m and L_{ev} are the latent heating of melting and evaporation of the substrate material. Cp_m and Cp_s are the specific heat capacity of

the liquid and solid phases of the substrate. It should be noted that since the liquid layer flows along the surface due to a shear force across the gas-liquid interface, it stores extra rate of energy. Therefore, the term $1.65 C_{p_m} (T_{ev} - T_m)$ represents the extra rate of energy due to melt layer flow at the surface as approximated in the previous study [97]. Moreover, in laser melting process, the rate of mass generated from solid into liquid at the solid surface can be written as:

$$\lim_{\Delta t \rightarrow 0} \frac{\Delta m}{\Delta t} = \frac{dm}{dt} = \dot{m}_L = \frac{d}{dt}(\rho \forall) = \rho_L V_L A$$

where \forall is the volume, A is the cross sectional area, ρ_L is the density of melt, and V_L is the liquid velocity along the y-axis (V_L is the velocity of melt generated from solid into liquid as depicted in Figure 4.1).

The rate of energy convective ($\dot{E}_{Convection}$) from the surface due to the assisting gas is:

$$\dot{E}_{Convection} = \dot{m}_g C_H (h_o - h_g) \quad (9)$$

where \dot{m}_g is the assisting gas mass flow rate, h_o is the total enthalpy ($h_o = \int_{T_{ref}}^{T_{oe}} Cp dT + \frac{1}{2} U_e^2$) at the edge of the boundary layer and h_g is the total enthalpy ($h_g = \int_{T_{ref}}^{T_{ev}} Cp dT + \frac{1}{2} U_{LS}^2$) at assisting gas-liquid interface (where U_{LS} is the assisting gas-liquid interface velocity). C_H is the heat transfer factor, which can be obtained from the Reynold's analogy, i.e. [98]:

$$C_H = \frac{1}{2} \frac{C_f}{Pr^{2/3}}$$

where C_f is the skin friction coefficient and Pr is the Prandtl number. The evaluation of skin friction coefficient is based on the type of assisting gas flow. In the case of turbulent boundary layer, C_f can be evaluated as [99]:

$$C_f = 0.0576 Re^{-1/5}$$

where Re is the Reynolds number of the assisting gas flowing over the molten metal. Therefore, the rate of energy input (\dot{E}_{in}) for melting at the assisting gas -liquid interface can be written as:

$$\dot{E}_{in} = P_o + \int \dot{q}_c dA - \dot{E}_{Convection} \quad (10)$$

where P_o is the laser power available at the assisting gas-liquid interface. It should be noted that the reflectivity of the surface is included in the P_o , i.e. P_o represents the laser power available after the reflection. Therefore,

$$\dot{E}_{in} = P_o + \int \dot{q}_c dA - \dot{m}_g C_H (h_o - h_g) \quad (11)$$

However, the rate of heat transfer from liquid surface to assisting gas can be written as:

$$\dot{E}_{gas} = \dot{m}_g C_H (h_o - h_g) = \rho_g U_e A C_H [Cp_g (T_{ev} - T_{oe}) + \frac{1}{2} (U_e^2 - U_{LS}^2)]$$

where A is the area, ρ_g is the assisting gas density, Cp_g is the specific heat capacity of the assisting gas at the edge of the boundary layer, C_H heat transfer parameter, and T_{oe} is the gas temperature at the edge of the boundary layer.

Consider the rate of heat transfer from liquid to solid substrate across the liquid-solid interface; in this case, continuity of heat flux at the interface can be employed, i.e.:

$$\dot{E}_{\text{Conduction}} = k_m \left[\frac{dT}{dx} \right]_m = Ah(T_m - T_{oi}) \quad (12)$$

where k_m and dT/dx is the thermal conductivity of the melt layer and the temperature gradient at the melt-solid interface. A is the area, h is the heat transfer coefficient at the interface, and T_{oi} is the solid temperature at infinitely large depth from the interface. It should be noted that the conjugate heat transfer equation employing Neumann boundary condition (continuity of heat flux and temperature) can be used across the liquid and gas surfaces (interface). However, the Neumann and radiation boundary conditions are omitted, since conjugate solution of the heating situation is simplified using a lump parameter analysis. Therefore, a simplified approach is introduced employing a Dirichlet boundary at the interface (boundary condition of first kind).

The rate of energy required for melting is (\dot{E}_{melt}):

$$\dot{E}_{\text{melt}} = P_o + \int \dot{q}_c dA - \dot{m}_g C_H (h_o - h_g) - Ah(T_m - T_{oi}) \quad (13)$$

Setting the rate of energy balance across the melt per unit area yields:

$$\frac{\dot{E}_{req}}{A} = \frac{\dot{E}_{melt}}{A} \quad (14)$$

Therefore:

$$V_L = \frac{1}{\rho_L} \frac{\frac{P_o}{A} + \dot{q}_c - h(T_m - T_{oi}) - \rho_g U_e C_H [Cp_g(T_{ev} - T_{oe}) + \frac{1}{2}(U_e^2 - U_{LS}^2)]}{[Cp_s(T_m - T_i) + L_m + \beta L_{ev} + 1.65 Cp_m(T_{ev} - T_m)]} \quad (15)$$

Consider the flow system as shown in Figure 4.1 for the steady production of liquid substrate while neglecting the evaporation from the liquid surface during laser heating, continuity equation for incompressible flow can be written, i.e.:

$$\frac{\partial U_L}{\partial s} + \frac{\partial V_L}{\partial y} = 0 \quad (16)$$

where U_L is the velocity of the liquid layer in the s direction. It should be noted that only a small fraction (β) of melt evaporates.

At the assisting gas-liquid interface, shear stresses should be the same.

In this case,

$$\tau_g = \tau_L$$

where τ_g is the shear stress exerted by an assisting gas on the liquid layer and τ_L is the shear stress exerted by the liquid layer on the gas

layer. If the liquid layer flow is assumed to be treated as Due to extremely small liquid layer thickness, then the shear stress (τ_L) is:

$$\tau_L = \mu_L \frac{\Delta U_L}{\delta_L} \quad (17)$$

where δ_L is liquid layer thickness. For zero velocity at the solid surface yields $\Delta U_L = U_{LS}$, where U_{LS} is the liquid layer velocity at assisting gas-liquid interface. Equation (17) becomes:

$$\tau_L \approx \mu_L \frac{\Delta U_{LS}}{\delta_L} \quad (18)$$

In the case of flow due to inclined surface with pressure variation, the velocity distribution in the liquid layer can be obtained from Navier-Stokes equation. After assuming liquid layer depth is considerably smaller than its width, then Navier-Stokes equation for two-dimensional flow reduces to:

$$\frac{\partial^2 U_L}{\partial y^2} = \frac{1}{\mu} \frac{d}{ds} (P + \gamma z) \quad (19)$$

where inclination angle of surface is:

$$\sin \theta = -\frac{dz}{ds} \quad (20)$$

Assuming a linear variation of pressure in the liquid layer with constant slope along the s direction due to considerably thin layer of liquid, it results:

$$\frac{d}{ds}(P + \gamma z) = \text{Constant} \quad (21)$$

Solving equation (19) with appropriate boundary condition yields the velocity distribution in the liquid layer, i.e.:

$$U_L = \frac{1}{2\mu} \frac{d}{ds}(P + \gamma z)(y^2 - y^\delta) + U_{LS}(1 - \frac{y}{\delta}) \quad (22)$$

Since $\frac{d}{ds}(P + \gamma z) = \text{constant}$ along the s direction, therefore:

$$\frac{\partial}{\partial s}(\frac{U_L}{U_{LS}}) = 1 - \frac{y}{\delta} \quad (23)$$

The continuity equation (16) can also be written as:

$$\int_0^y \frac{\partial V_L}{\partial y} dy = - \int_0^y \frac{\partial U_L}{\partial s} dy \quad (24)$$

or

$$\int_{V_L(0)}^{V_L(y)} dV_L = - \frac{d(\delta_L U_{LS})}{ds} \int_0^y \frac{U_L}{U_{LS}} \frac{dy}{\delta_L} \quad (25)$$

Inserting equation (23) into equation (25) and after the mathematical arrangements, equation (25) yields:

$$V_L(y) - V_L(0) = -\frac{d}{ds} \left\{ \delta_L U_{LS} \left[\frac{y}{\delta_L} - \frac{1}{2} \left(\frac{y}{\delta_L} \right)^2 \right] \right\} \quad (26)$$

Since at $y = 0$ (at the assisting gas-liquid interface) $\Rightarrow V_L(0) = 0$ and $y = -\delta_L$ (at the liquid-solid interface) $\Rightarrow V_L(0) = V_L$, equation (26) reduces to:

$$V_L = -\frac{d}{ds} \left(\frac{1}{2} \delta_L U_{LS} \right) \quad (27)$$

Introducing V_L from equation (15) into equation (27), it yields:

$$-\frac{d}{ds} \left(\frac{1}{2} \delta_L U_{LS} \right) = \frac{1}{\rho_L} \frac{\frac{P_o}{A} + \dot{q}_c - h(T_m - T_{oi}) - \rho_g U_e C_H [Cp_g(T_{ev} - T_{oe}) + \frac{1}{2}(U_e^2 - U_{LS}^2)]}{[Cp_s(T_m - T_i) + L_m + \beta L_{ev} + 1.65 Cp_m(T_{ev} - T_m)]} \quad (28)$$

or:

$$-\frac{d}{ds} \left(\frac{1}{2} \delta_L U_{LS} \right) = C_1 - \frac{\rho_g U_e C_H [Cp_g(T_{ev} - T_{oe}) + \frac{1}{2}(U_e^2 - U_{LS}^2)]}{C_2} \quad (29)$$

where

$$C_1 = \frac{1}{\rho_L} \frac{\frac{P_o}{A} + \dot{q}_c - h(T_m - T_{oi})}{[Cp_s(T_m - T_i) + L_m + \beta L_{ev} + 1.65 Cp_m(T_{ev} - T_m)]}$$

and

$$C_2 = \rho_L [Cp_s(T_m - T_i) + L_m + \beta L_{ev} + 1.65 Cp_m(T_{ev} - T_m)]$$

Due to the assisting gas flow over the melt surface, the heat transfer characteristics are modified accordingly. In this case, the rate of heat transfer from the liquid surface to assisting gas is modified as [98]:

$$\dot{E}_{gas} = Ns^{-1/5} \quad (30)$$

where N is a function varying with \dot{E}_{gas} and considered to be constant along S [98]. Therefore equation (29) becomes:

$$-\frac{d}{ds}\left(\frac{1}{2}\delta_L U_{LS}\right) = C_1 - \frac{Ns^{1/5}}{C_2} \quad (31)$$

Integration of equation (31) yields:

$$-\frac{1}{2}\delta_L U_{LS} = \int \left[C_1 - \frac{Ns^{1/5}}{C_2}\right] ds \quad (32)$$

or:

$$-\frac{1}{2}\delta_L U_{LS} = C_1 s - \frac{5}{4} \frac{N}{C_2} s^{4/5} + C_3 \quad (33)$$

where C_3 is a constant to be determined from the boundary conditions.

Consider at the tip of the cutting edge, the velocity of the liquid surface is approximately zero, since the liquid layer thickness is negligibly small in this region. Therefore, at $s = 0 : U_{LS} = 0$; therefore, $C_3 = 0$.

Replacing $\dot{E}_{gas} = Ns^{-1/5}$ in equation (33) yields:

$$-\frac{1}{2}\delta_L U_{LS} = C_1 s - \frac{5}{4} \frac{\rho_g U_e C_H [Cp_g (T_{ev} - T_{oe}) + \frac{1}{2}(U_e^2 - U_{LS}^2)]s}{C_2} \quad (34)$$

Let us define

$$C_4 = \rho_g U_e C_H [Cp_g (T_{ev} - T_{oe})]$$

Then equation (34) yields:

$$-\frac{1}{2}\delta_L U_{LS} = C_1 s - \frac{5}{4} \frac{C_4 s}{C_2} + \frac{1}{2} \frac{(U_e^2 - U_{LS}^2)]s}{C_2} \quad (35)$$

Re-arrangement of equation (35) yields:

$$\frac{s}{2C_2} U_{LS}^2 - \frac{1}{2}\delta_L U_{LS} = C_1 s - \frac{(5C_4 + 2U_e^2)s}{4} \quad (36)$$

Moreover, to obtain the liquid layer thickness, consider the shear stresses at the assisting gas-liquid interface, which is:

$$\tau_g = \tau_L \quad (37)$$

From equation (17): $\tau_L = \mu_L \frac{U_{LS}}{\delta_L}$; and τ_g can be written as:

$$\tau_g = \frac{C_f}{2} \rho_g U_e^2$$

Inserting the shear stresses into equation (36), the liquid layer thickness becomes:

$$\delta_L = \mu_L \frac{U_{LS}}{U_e} \frac{2}{C_f \rho_g U_e^2} \quad (38)$$

Combining equation (36) and (38), it yields:

$$U_{LS} = \sqrt{\frac{C_1}{C_5} s - \frac{5}{4} \frac{(C_4 + 2U_e^2)s}{C_5}} \quad (39)$$

where

$$C_5 = \frac{s}{2C_2} - \frac{1}{2} \mu_L \frac{1}{C_f \rho_g} \frac{2}{U_e^2}$$

Substituting equation (39) into equation (38) gives the liquid film thickness in the melting section, i.e. [97]:

$$\delta_L = \mu_L \frac{\sqrt{\frac{C_1}{C_5} s - \frac{5}{4} \frac{(C_4 + 2U_e^2)s}{C_5}}}{\frac{1}{2} C_f \rho_g U_e^2} \quad (40)$$

Equations (39) and (40) are used to compute liquid layer velocity and liquid layer thickness in the cutting section.

A computer program in Mathematica software is developed to compute the liquid layer thickness (δ_L) from equation (6) for various laser power settings. Table 4.1 gives the simulation conditions.

Table 4.1. Thermal properties used in the simulations for inconel 625 powder.

Source of Variation	Value	Units
Boiling temperature	3133	K
Melting temperature	1910	K
Density of assisting gas	1.97 at 50kPa	kg/m ³
Density of workpiece	8440	kg/m ³
Fraction of evaporation contribution (β)	0.1	-
Specific heat capacity of solid	429	J/kgK
Specific heat capacity of melt	560	J/kgK
Specific heat capacity of gas	918	J/kgK
Thermal conductivity of molten metal	21.3	W/mK
Thermal conductivity of solid	9.8	W/mK
Latent heat of melting	$10^5 \times 2.72$	J/kg
Latent heat of boiling	$10^6 \times 6.10$	J/kg

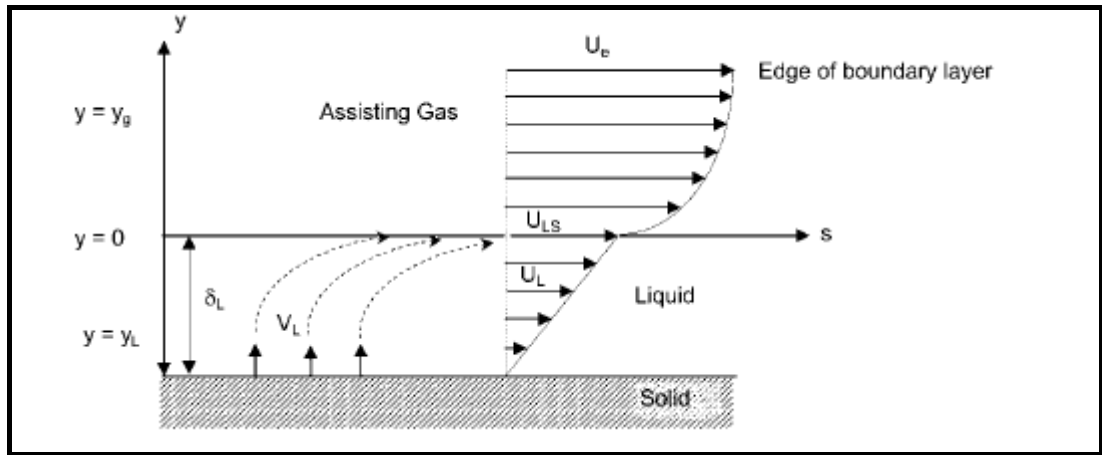


Figure 4.1. A schematic view of liquid- and gas-side velocities in the coordinate system. [100]

4.2 Temperature Formulation:

Laser pulse heating consists of two cycles, namely heating and cooling cycles. The heating cycle starts with the initiation of the pulse and ends when the pulse intensity reduces to zero. The construction of the step intensity pulse can be achieved through subtraction of two unit step functions, i.e. the first unit step pulse starts at time $t = 0$ (Figure 4.3) while the second unit step pulse (shifted unit step pulse) starts at time $t + \Delta t$ (Figure 4.4). The difference in both pulses results in the step intensity pulse, i.e.[101]:

$$SP(t) = I[t] - I[t - \Delta t] \quad (41)$$

$$I[t] = \begin{pmatrix} 1, & t > 0 \\ 0, & t < 0 \end{pmatrix} \quad \text{and} \quad I[t - \Delta t] = \begin{pmatrix} 1, & t > \Delta t \\ 0, & t < \Delta t \end{pmatrix} \quad (42)$$

and $SP(t)$ is the step intensity pulse with a unit intensity. The Fourier heat transfer equation for a laser heating pulse can be written as:

$$\frac{\partial^2 T}{\partial x^2} + \frac{I_1 \delta}{k} (C_1 * SP(t)) e^{-\alpha x} = \frac{1}{\alpha} \frac{\partial T}{\partial t} \quad (43)$$

where

$$I_1 = (1 - r_f) I_o$$

and r_f is the reflection coefficient, C_1 is the intensity multiplication factor, and I_0 is the laser power intensity.

The initial and boundary conditions are:

At time $t = 0$: $T(x,0) = T_0$

At the surface $x = 0$: $\left[\frac{\partial T}{\partial x} \right]_{x=0} = 0$ and $x = \infty$ $T(\infty, t) = T_0$.

After introducing the dimensionless parameters as:

$$\tau = \alpha \delta^2 t \quad : \quad \eta = \delta x \quad : \quad \theta = T \frac{k \delta}{I_1}$$

Equation (43) becomes:

$$\frac{\partial^2 \theta}{\partial x^2} + [C_1 * SP(\tau)] e^{-\eta} = \frac{\partial \theta}{\partial \tau} \quad (44)$$

where

$$SP(\tau) = I[\tau] - I[\tau - \Delta \tau] \quad (45)$$

and $\Delta \tau = \Delta \alpha \delta^2 t$.

The dimensionless initial and boundary conditions become:

At time $\tau = 0$: $\theta(\eta, 0) = \theta_o$

At the surface $\eta = 0$: $\left[\frac{\partial \theta}{\partial \eta} \right]_{\eta=0} = 0$ and at $\eta = \infty$: $\theta(\infty, \tau) = \theta_o$

The solution of equation (44) can be obtained through Laplace transformation method, i.e., with respect to τ , the Laplace transformation of equation (44) yields:

$$\frac{\partial^2 \bar{\theta}}{\partial \eta^2} + [C_1 * SP(\tau)]e^{-\eta} = [s\bar{\theta} - \theta_o]$$

or

$$\frac{\partial^2 \bar{\theta}}{\partial \eta^2} - s\bar{\theta} = -[C_1 * SP(\tau)]e^{-\eta} - \theta_o \quad (46)$$

The homogenous solution of equation (46) can be written as:

$$\bar{\theta}_h = K_1 e^{\sqrt{s}\eta} + K_2 e^{-\sqrt{s}\eta} \quad (47)$$

and the particular solution for equation (46) is:

$$\bar{\theta}_p = \frac{[C_1 * SP(s)]}{s-1} e^{-\eta} + \frac{\bar{\theta}_o}{s} \quad (48)$$

Therefore, the solution of dimensionless temperature in Laplace domain becomes:

$$\bar{\theta} = K_1 e^{\sqrt{s}\eta} + K_2 e^{-\sqrt{s}\eta} + \frac{[C_1 * SP(s)]}{s-1} e^{-\eta} + \frac{\bar{\theta}_o}{s} \quad (49)$$

The boundary condition $\theta(\infty, \tau) = \theta_o$ results in $K_1 = 0$. The boundary condition at the surface yields:

$$\left[\frac{\partial \bar{\theta}}{\partial \eta} \right]_{\eta=0} = \frac{\partial}{\partial \eta} \left[-K_2 e^{-\sqrt{s}\eta} - \frac{[C_1 * SP(s)]}{s-1} e^{-\eta} + \frac{\bar{\theta}_o}{s} \right]_{\eta=0} = 0$$

Therefore:

$$K_2 = -\frac{[C_1 * SP(s)]}{\sqrt{s}(s-1)}$$

Therefore, equation (49) becomes:

$$\bar{\theta} = -\frac{[C_1 * SP(s)]}{s-1} e^{-\sqrt{s}\eta} + \frac{[C_1 * SP(s)]}{s-1} e^{-\eta} + \frac{\bar{\theta}_o}{s} \quad (50)$$

Noting from equation 1 that:

$$SP(s) = \frac{1}{s} - \frac{e^{-(\Delta\tau)s}}{s}$$

Hence equation (50) becomes:

$$\bar{\theta} = -C_1 \left[\frac{e^{-\sqrt{s}\eta}}{s\sqrt{s}(s-1)} - \frac{e^{-\sqrt{s}\eta-(\Delta\tau)s}}{s\sqrt{s}(s-1)} \right] + C_1 \left[\frac{e^{-\eta}}{s(s-1)} - \frac{e^{-\eta-(\Delta\tau)s}}{s(s-1)} \right] + \frac{\bar{\theta}_o}{s} \quad (51)$$

Noting that:

$$\frac{1}{s(s-1)} = \frac{1}{s-1} - \frac{1}{s}$$

The inversion of Laplace transforms can be written as:

$$L^{-1}\left[\frac{e^{-\sqrt{s}\eta}}{s\sqrt{s}(s-1)}\right] = L^{-1}\left[\frac{e^{-\sqrt{s}\eta}}{\sqrt{s}(s-1)}\right] - L^{-1}\left[\frac{e^{-\sqrt{s}\eta}}{s\sqrt{s}}\right]$$

and

$$L^{-1}\left[\frac{e^{-\eta}}{s(s-1)}\right] = L^{-1}\left[\frac{e^{-\eta}}{(s-1)}\right] - L^{-1}\left[\frac{e^{-\eta}}{s}\right]$$

Consequently, Laplace transformation of $L^{-1}\left[\frac{e^{-\sqrt{s}\eta}}{s\sqrt{s}(s-1)}\right]$ yields [102]:

$$\begin{aligned} L^{-1}\left[\frac{e^{-\sqrt{s}\eta}}{s\sqrt{s}(s-1)}\right] &= \frac{e^{\tau}}{2} \left[e^{-\eta} \operatorname{Erfc}\left(-\sqrt{\tau} + \frac{\eta}{2\sqrt{\tau}}\right) - e^{\eta} \operatorname{Erfc}\left(\sqrt{\tau} + \frac{\eta}{2\sqrt{\tau}}\right) \right] \\ &- \left[\frac{2\sqrt{\tau}}{\sqrt{\pi}} e^{-\frac{\eta^2}{4\tau}} - \eta \operatorname{Erfc}\left(\frac{\eta}{2\sqrt{\tau}}\right) \right] \end{aligned} \quad (52)$$

Let us denote the right hand side of equation (52) by $f(\eta, \tau)$. Consider the following Laplace operation:

$$L^{-1} e^{-\Delta s} F(s) = f(t - \Delta t)$$

where $L^{-1} F(s) = f(t)$. Therefore,

$$L^{-1} e^{-\Delta s} \left[\frac{e^{-\sqrt{s}\eta}}{s\sqrt{s}(s-1)} \right] = f(\eta, \tau - \Delta \tau)$$

Consequently,

$$\begin{aligned}
L^{-1} e^{-\Delta s} \left[\frac{e^{-\sqrt{s}\eta}}{s\sqrt{s}(s-1)} \right] &= \frac{e^{\tau-\Delta\tau}}{2} \left[e^{-\eta} \operatorname{Erfc} \left(-\sqrt{\tau-\Delta\tau} + \frac{\eta}{2\sqrt{\tau-\Delta\tau}} \right) \right. \\
&\quad \left. - e^{-\eta} \operatorname{Erfc} \left(\sqrt{\tau-\Delta\tau} + \frac{\eta}{2\sqrt{\tau-\Delta\tau}} \right) \right] \\
&\quad - \left[\frac{2\sqrt{\tau-\Delta\tau}}{\sqrt{\pi}} e^{-\frac{\eta^2}{4(\tau-\Delta\tau)}} - \eta \operatorname{Erfc} \left(\frac{\eta}{2\sqrt{\tau-\Delta\tau}} \right) \right]
\end{aligned} \tag{53}$$

Laplace transformation of $L^{-1} \left[\frac{e^{-\eta}}{s(s-1)} \right]$ yields:

$$L^{-1} \left[\frac{e^{-\eta}}{s(s-1)} \right] = e^{-\eta} [e^{\tau} - 1[\tau]] \tag{54}$$

where $1[\tau]$ is a unit step function. Similarly, Laplace transformation of

$$L^{-1} e^{-\Delta s} \left[\frac{e^{-\eta}}{s(s-1)} \right] \text{ is:}$$

$$L^{-1} e^{-\Delta s} \left[\frac{e^{-\eta}}{s(s-1)} \right] = e^{-\eta} [e^{\tau-\Delta\tau} - 1[\tau-\Delta\tau]] \tag{55}$$

Using the terms in equations (52, 53, 54, and 55), dimensionless temperature (Laplace inversion of equation 51) becomes [101]:

$$\begin{aligned}
\theta = \theta_o + C_1 & \left\{ e^{-\eta} [e^{\tau} - I[\tau]] - \frac{e^{\tau}}{2} \left[\begin{aligned} & e^{-\eta} \operatorname{Erfc} \left(-\sqrt{\tau} + \frac{\eta}{2\sqrt{\tau}} \right) \\ & - e^{-\eta} \operatorname{Erfc} \left(\sqrt{\tau} + \frac{\eta}{2\sqrt{\tau}} \right) \end{aligned} \right] \right. \\
& \left. + \left[\frac{2\sqrt{\tau}}{\pi} e^{-\frac{\eta^2}{4\tau}} - \eta \operatorname{Erfc} \left(\frac{\eta}{2\sqrt{\tau}} \right) \right] \right\} \\
- C_1 & \left\{ e^{-\eta} [e^{\tau-\Delta\tau} - I[\tau-\Delta\tau]] - \frac{e^{\tau-\Delta\tau}}{2} \left[\begin{aligned} & e^{-\eta} \operatorname{Erfc} \left(-\sqrt{\tau-\Delta\tau} + \frac{\eta}{2\sqrt{\tau-\Delta\tau}} \right) \\ & - e^{-\eta} \operatorname{Erfc} \left(\sqrt{\tau-\Delta\tau} + \frac{\eta}{2\sqrt{\tau-\Delta\tau}} \right) \end{aligned} \right] \right. \\
& \left. + \left[\frac{2\sqrt{\tau-\Delta\tau}}{\pi} e^{-\frac{\eta^2}{4(\tau-\Delta\tau)}} - \eta \operatorname{Erfc} \left(\frac{\eta}{2\sqrt{\tau-\Delta\tau}} \right) \right] \right\}
\end{aligned} \tag{56}$$

where Erfc is the complimentary Error function.

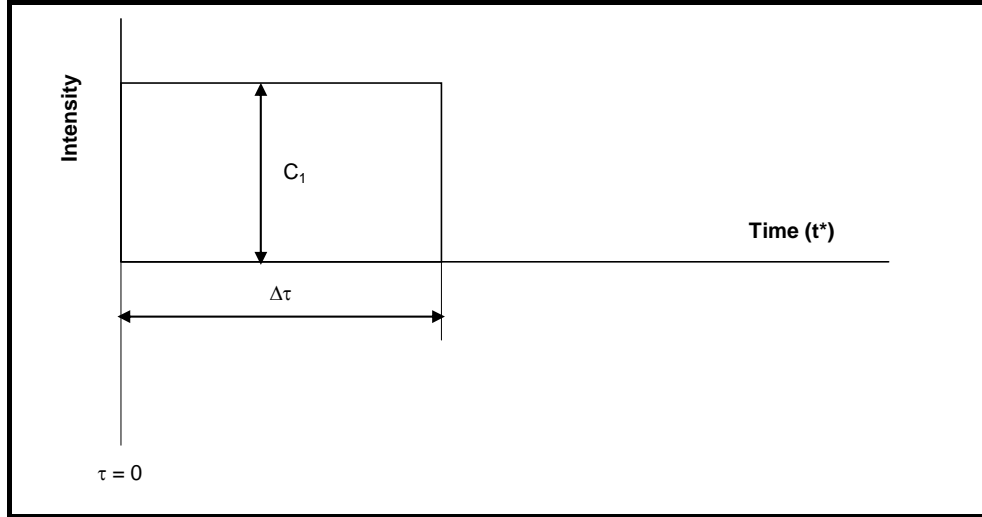


Figure 4.2. A step input pulse intensity used in the analysis.

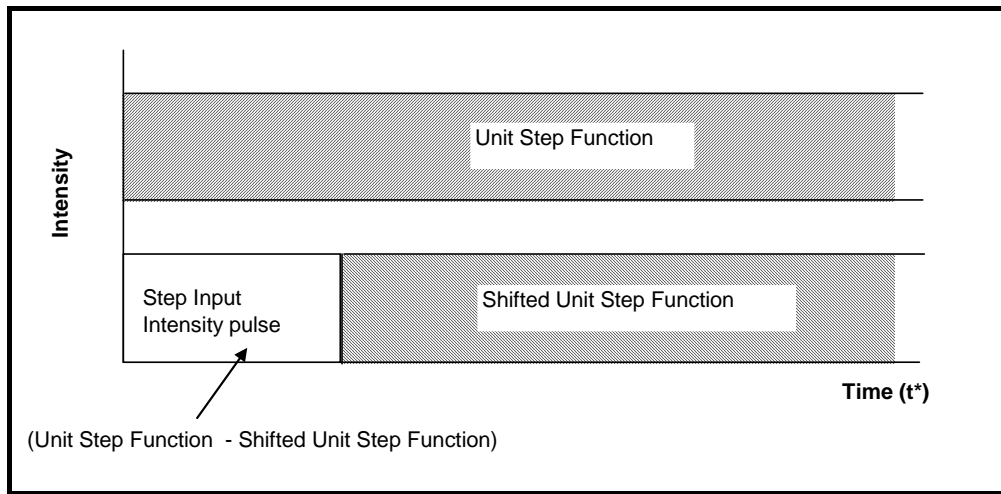


Figure 4.3. Construction of a step input intensity pulse.

Equation (56) is the closed form solution for temperature distribution.

Two consecutive pulses are used in the simulations as shown in Figure 4.4.

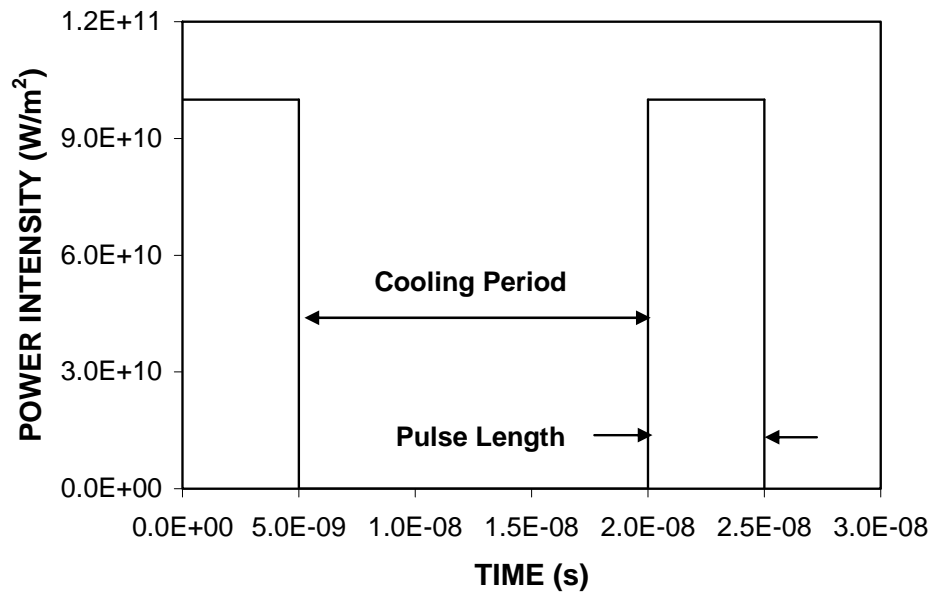


Figure 4.4. Two laser pulses used in the simulations.

The material properties and simulation conditions for equation (56) are given in Table 4.2. The selection of laser pulse parameters are similar to those used in practical applications. The absorption coefficient (δ) is taken as 6.17×10^6 1/m for all the materials simulated. It should be noted that the thermal properties of the coating is obtained from the open literature for Inconel 625 [103] while thermal properties of coating with addition of WC are estimated using the mass averaged base calculation.

Table 4.2. Material properties used in the simulations.

	K (W/mK)	Cp (J/kgK)	$\alpha \times 10^{-6}$ (m ² /K)	ρ (kg/m ³)	$\delta \times 10^6$ (1/m)	Io (W/m ²)	h [104] (W/m ²)
0%WC	9.8	429	2.707	8440	6.17	10^{11}	3000
9.3% WC	16.7	408.6	4.81	9124	6.17	10^{11}	3000
47% WC	44.68	326	1.33	11899	6.17	10^{11}	3000

Chapter 5 – Results and Discussions

5.0 Introduction

The results and discussion are categorized into morphological, metallurgical changes, thermal analysis, mechanical and corrosion properties prior and post laser re-melting. Thus, the discussion of observations and findings are given in coming appropriate classified headings.

5.1 Morphological and Metallurgical Changes in Coating with no Inclusion of WC

Laser melting of HVOF sprayed Inconel 625 coating with and without WC inclusion is carried out in the thesis. The melt layer thickness and microstructural changes in the laser re-melted zone are examined. The melt layer thickness is formulated using the lump parameter analysis and compared with the experimental results.

Figure 5.1 shows melt layer thickness with laser output power obtained from predictions (equation (40)) and experimental data for no WC inclusion situation. It should be noted that the measurements were repeated five times at each data point and estimated error is shown in bars at each data point in Figure 5.1. The melt layer thickness increases almost in a parabolic form with increasing laser output power. In the analysis laser scanning speed and beam spot size at the workpiece surface are kept constant to resemble the experimental conditions. The non-linearity in the melt layer variation occurs for the laser power intensity ≤ 400 W. This is because of the heating situation during the formation of the melt layer at low laser power intensities. In this case, conduction and convection losses from the melt region are almost comparable to the laser power at low intensities. The increase in the conduction and convection losses from the melt region is incremental as the laser power increases. Consequently, increase in the melt size mostly depends on the increase in the laser irradiated power. This provides almost linear variation of melt layers thickness with increasing laser irradiated power beyond 400 W.

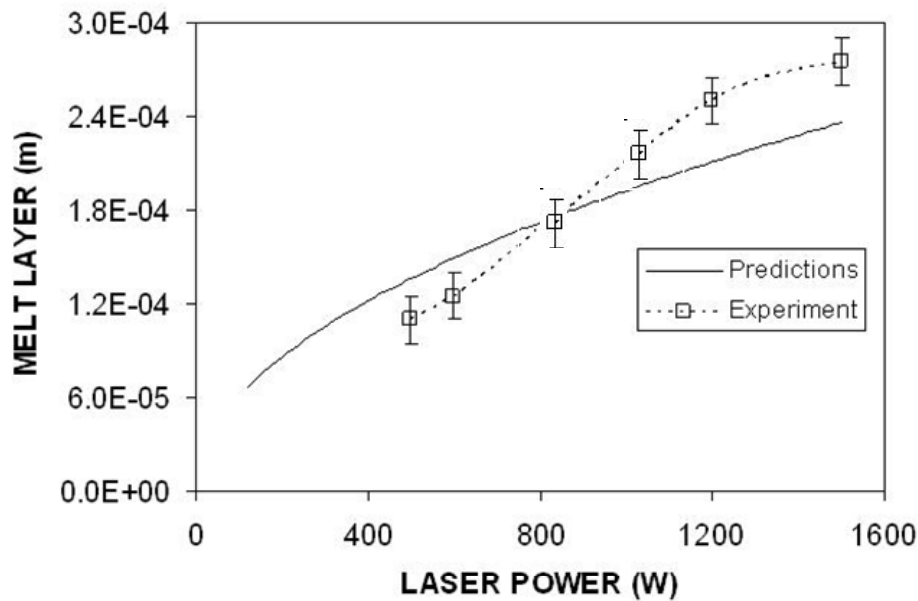


Figure 5.1. Melt layer thickness with laser power predicted from the lump parameter analysis (equation (40)) and obtained from the experiment.

When comparing the experimental results and predictions of melt layer thickness, it is evident that both results are in good agreement. Some small discrepancies between both results are because of the assumptions of the structural homogeneity and porous free consideration, as well as constant thermal properties used in the analysis. Although the porosity level in the coating is almost 2-3 %, which is small, the oxide formation in the coating as a result of spraying process alters the thermal properties. In addition, thermal properties vary with temperature, provided that this variation is not significant. Consequently, the effects

of structural changes such as oxide formation, and temperature dependant properties are responsible for the discrepancies between the experimental results and the predictions of the melt layer thickness.

Figure 5.2 shows SEM micrographs of HVOF Inconel 625 coating (without WC inclusion) prior to laser melting. It can be observed that the coating consists of lamellar structure. The voids are scattered randomly provided that overall porosity is within 2-3 %. Moreover, some oxidation around the splats is evident, which occurs during the in-flight prior to impacting the base material surface. Some dark inclusions around the splats are the evidence of brittle oxide particles.

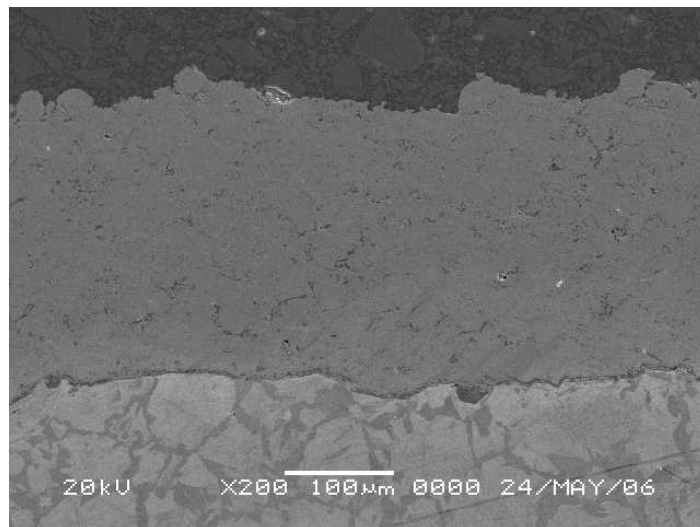


Figure 5.2. SEM micrograph of HVOF Inconel 625 coating (without WC inclusion) cross-section prior to laser melting.

Figure 5.3 shows SEM micrographs of the cross-section of laser melted and re-solidified coating structure without WC inclusion. The cellular structure is observed upon solidification and the size of grain changes across the cross-section of the laser re-melted region. This is because of the non-uniform cooling at high rates. In this case, the liquid solution upon melting is solidified progressively while the composition of the solid is not uniform. The distribution of the solute in the solid after the completion of the solidification becomes different than from that in the liquid. This situation is also observed from the EDS results (Table 5.1); in which case, non-uniformity of the elemental composition in the coating post laser re-melting is evident. Moreover, the development of transverse periodicity in the solidification process is also evident. This is attributed to the instability during the super-cooling process. In this case, cellular sub-structures are formed and then fine regular corrugated structures are developed extending along the regular cellular boundary. The corrugations are roughly parallel to the direction of growth of the crystal (Figure 5.4). Furthermore, the formation of the cellular structure (Figure 5.3) is because of the liquid, which is rapidly decanted exposing the solid-liquid interface. The cell size increases with decreasing rate of growth and the growth direction depends on the impurity content, speed of growth, and the inclination of the dendrite direction to the growth

direction. The heat flow and cooling rate are related to the asymmetry in the shape of the cells, which in turn results in anisotropy of the growth rate of the cells. The segregation occurs at the grain boundaries during the process of solidification (Figure 5.5), i.e. two crystals grow side-by-side and the boundary between them forms a groove. It should be noted that cellular segregation occurs when super-cooling takes place during the solidification. However, segregation decreases as a result of diffusion during the cooling after the solidification. In the cooling process, if the temperature gradient is reduced, then the zone of super-cooling extends. Consequently, the cells change to characteristic of dendrites forming cellular dendrites as seen from Figure 5.6. This appearance is distinct from the cellular structure and free dendritic growth. One of the causes for this type of morphology is that the cellular dendritic type of growth occurs when the temperature gradient is small in the liquid phase providing the heat rejection into the solid at a low rate. Alignment of dendrites forms webs, which enhances conducting path for heat flow from the liquid to the crystals. It should be noted that the cellular-dendritic growth differs from cellular growth; in which case, the depth of super-cooled zone is greater for cellular growth.

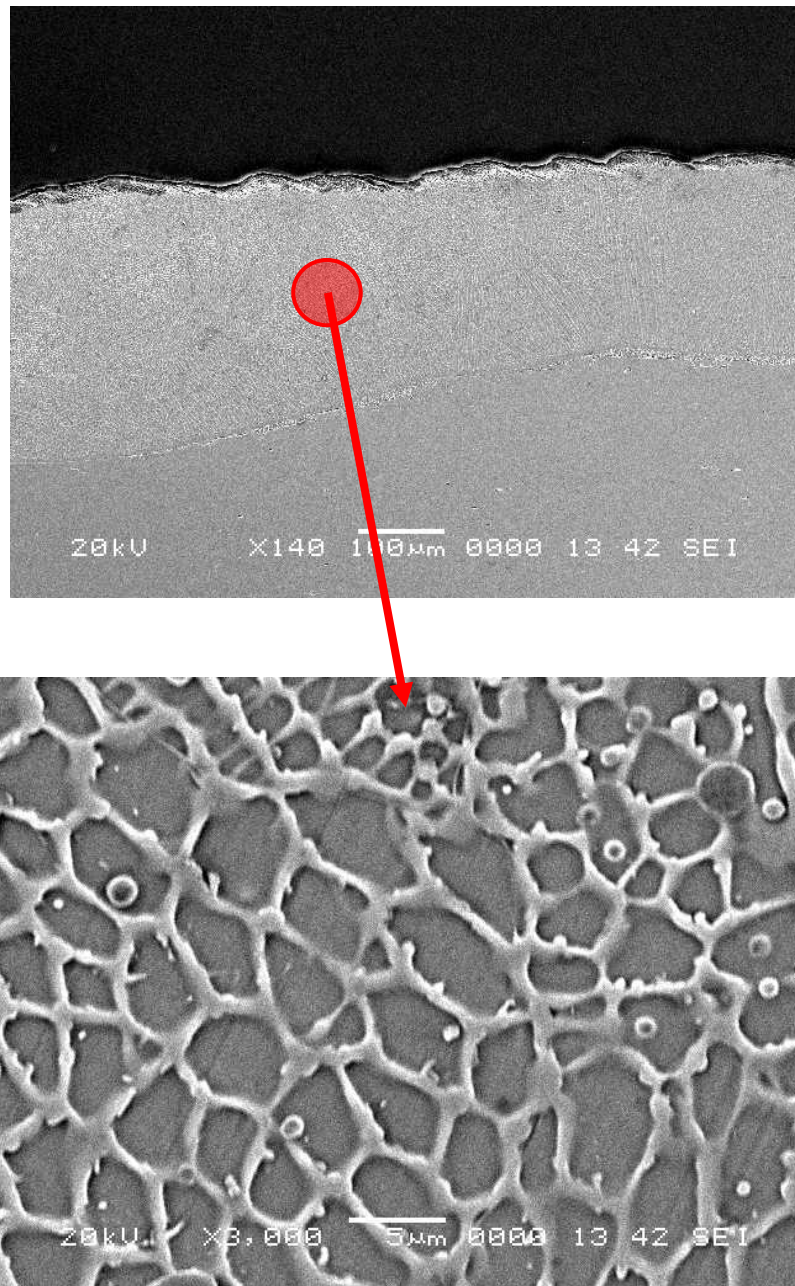


Figure 5.3. SEM micrograph of laser HVOF Inconel 625 coating (without WC inclusion) cross-section after the laser treatment. The cellular structure is clearly observed.

Table 5.1. EDS results for the laser melted region for HVOF Inconel 625 coating. Each spectrum represents the different points across the cross-section of the coating after the laser treatment. The existing of gold in the spectrums is because of the gold coating of the samples prior to the EDS analysis.

Spectrum	C	Al	Cr	Fe	Ni	Au	Total
Spectrum 1		0.25	16.98	52.49	30.28		100.00
Spectrum 2	0.67		16.18	45.17	26.60	11.38	100.00
Spectrum 3	0.37		16.24	45.96	26.55	10.87	100.00
Spectrum 4	0.50		15.60	46.36	25.65	11.89	100.00
Spectrum 5	0.79		15.70	45.95	25.32	12.25	100.00
Spectrum 6	0.62		16.50	45.22	26.82	10.84	100.00
Spectrum 7	0.59		17.60	44.48	26.36	10.97	100.00
Spectrum 8	0.59		14.33	46.64	26.56	11.88	100.00
Spectrum 9	0.60		15.29	46.68	25.31	12.11	100.00
Max.	0.79	0.25	17.60	52.49	30.28	12.25	
Min.	0.37	0.25	14.33	44.48	25.31	10.84	

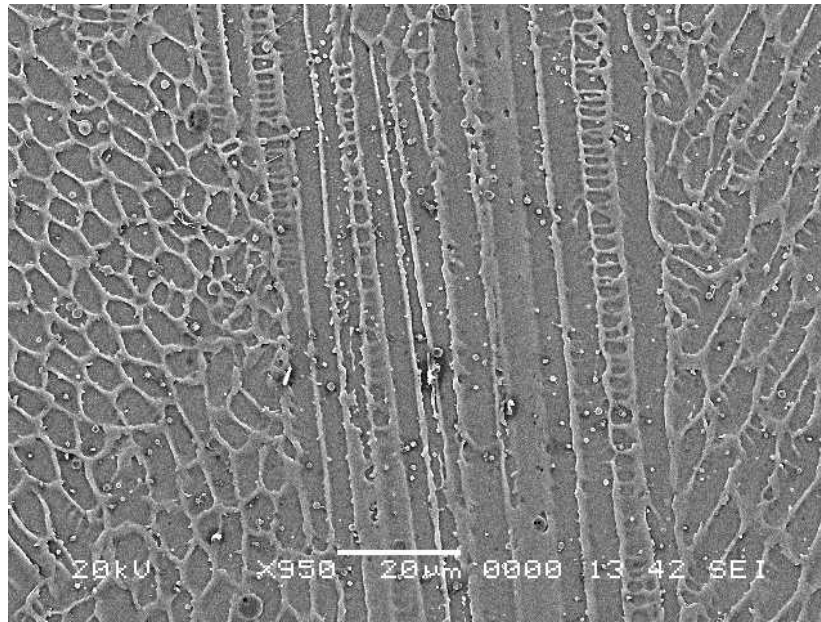


Figure 5.4. SEM micrograph of laser HVOF Inconel 625 coating (without WC inclusion) cross-section after the laser treatment. The corrugations of the cellular structure are observed.

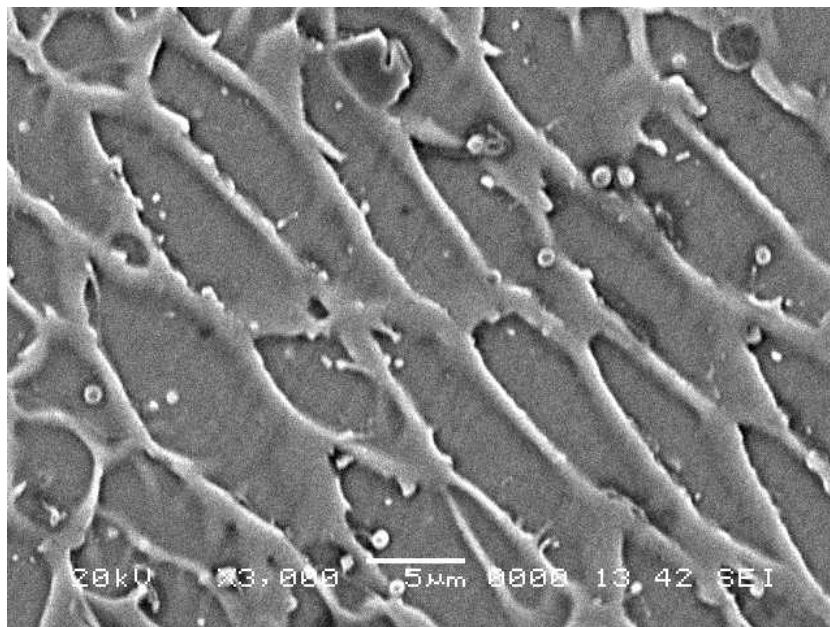


Figure 5.5. SEM micrograph of laser HVOF Inconel 625 coating (without WC inclusion) cross-section after the laser treatment. The

differences in the cell sizes are observed due to non-uniform cooling rates.

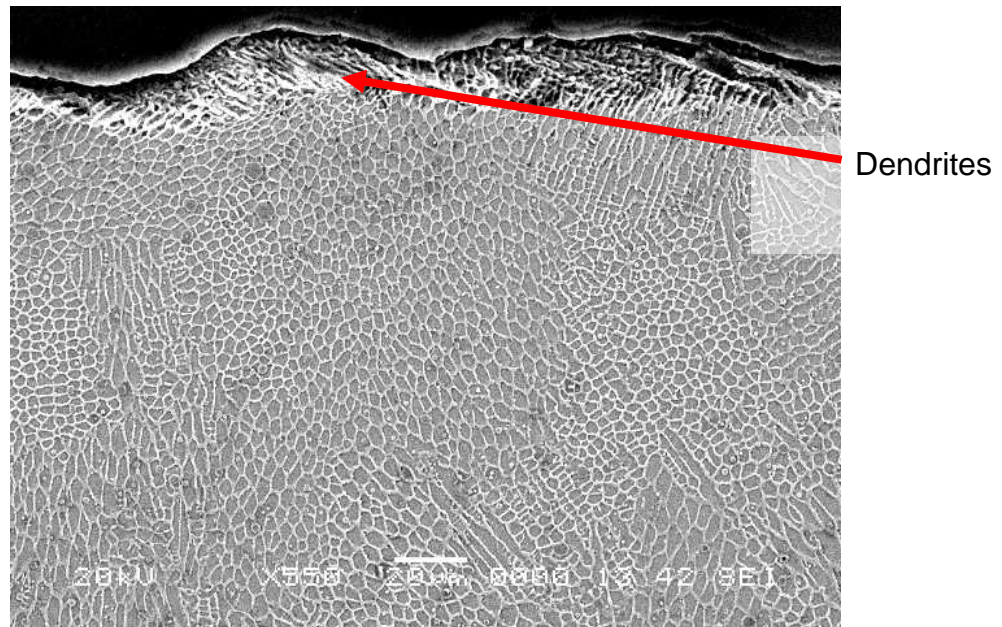


Figure 5.6. SEM micrograph of laser HVOF Inconel 625 coating (without WC inclusion) cross-section after the laser treatment. The dendritic structure is observed in the surface region of the coating.

5.2 Mechanical Changes and Thermal Analysis in Coating

In this work, laser melting of the coating formed through HVOF thermal spraying of Inconel 625 powders mixed with WC particles onto a steel 304 workpiece is investigated. Temperature rise inside the substrate material is computed and the residual stress developed in the substrate material after the laser treatment process is measured using the XRD technique. The analytical solution presented in the early study [27] is

used to determine the residual stress in the coating. In addition, the influence of WC content on the residual stress is also examined.

Figure 5.7 shows temporal variation of temperature (obtained from equation (56)) at the coating surface during the laser heating process for three concentrations of WC. It should be noted that the thermal properties used in the simulations is recalculated according to the WC concentration in the coating, which is given in Table 4.2 and equation (56) is used in the simulations. The rise of surface temperature is significantly high in the early heating period and as the time progresses, the rate of temperature rise reduces. This is because of the internal energy gain of the substrate material from the irradiated laser energy. In this case, internal energy gain from the irradiated field is significantly high and energy loss from the free surface through forced convection is small as well as the rate of energy diffusion from the surface region to the solid bulk is low due to the low temperature gradient in the early heating period. It should be noted that the influence of heat transfer coefficient used in the current simulations ($h = 3000 \text{ W/m}^2\text{K}$) on temperature rise is not significant, which is due to the fact that the heat transfer coefficient $h \leq 10^7 \text{ W/m}^2\text{K}$ temperature rise is not affected [105]. However, as the heating period progresses, the temperature gradient in the neighborhood of the surface increases. This enhances the

heat diffusion from the surface region to the solid bulk. Consequently, internal energy gain in the irradiated region balances the diffusional energy transfer from the irradiated region to the solid bulk. This changes the temperature rise at the surface such that it increases steadily with progressing time. Moreover, WC content in the coating modifies temperature rise at the surface. This is because of the change in the thermal properties. In this case, increasing WC content improves the thermal conductivity of the coating and suppresses temperature rise at the surface. Consequently, increasing thermal conductivity enhances the diffusional energy transport from the surface region to the solid bulk lowering the internal energy gain in the surface region of the coating.

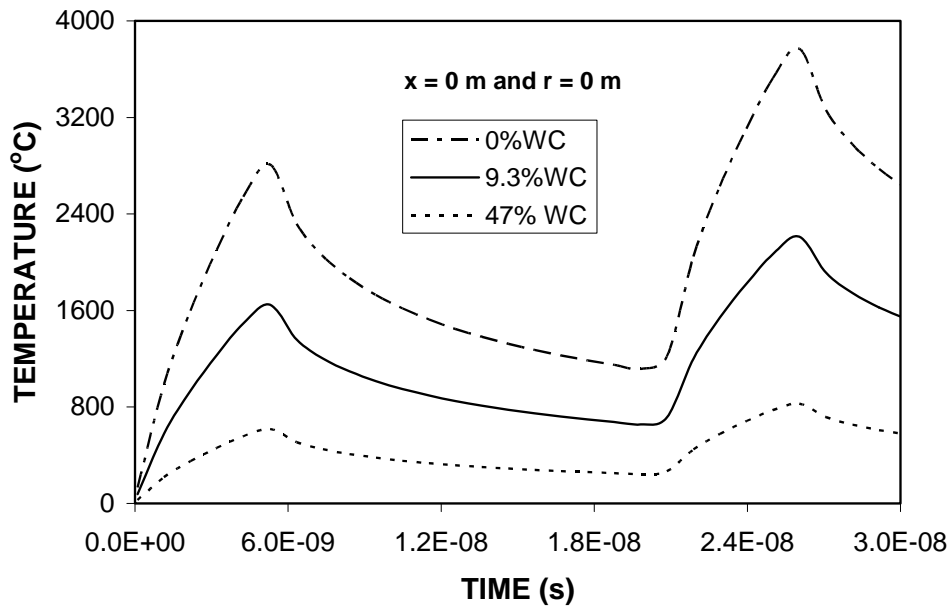


Figure 5.7. Temporal distribution of temperature due to two consecutive laser pulses for HVOF coating of Inconel 625 powders blended with different percentage of WC.

Figure 5.8 shows temperature distribution in the coating for two WC concentrations. Temperature decays sharply in the vicinity of the surface and as the depth below the surface increases, temperature decay becomes gradual. The sharp decay of temperature in the surface region is because of the internal energy gain from the irradiated field, which is high in this region. As the depth below the surface becomes comparable to the absorption depth (1.6×10^{-7} m), temperature decay becomes gradual in this region. This is due to the fact that the energy transfer by conduction beyond this region dominates the energy transport in the coating. Consequently, large temperature gradient in the surface region results in high heating and cooling rates in this region. Increasing WC content modifies temperature distribution inside the substrate material. In this case, high WC content lowers the temperature gradient in the surface region because of increasing thermal conductivity (Table 4.2). It should be noted that increasing WC content increases the thermal conductivity of the coating. Surface temperature attains low values due to high thermal conductivity and the temperature gradient becomes low with increasing WC content in the coating.

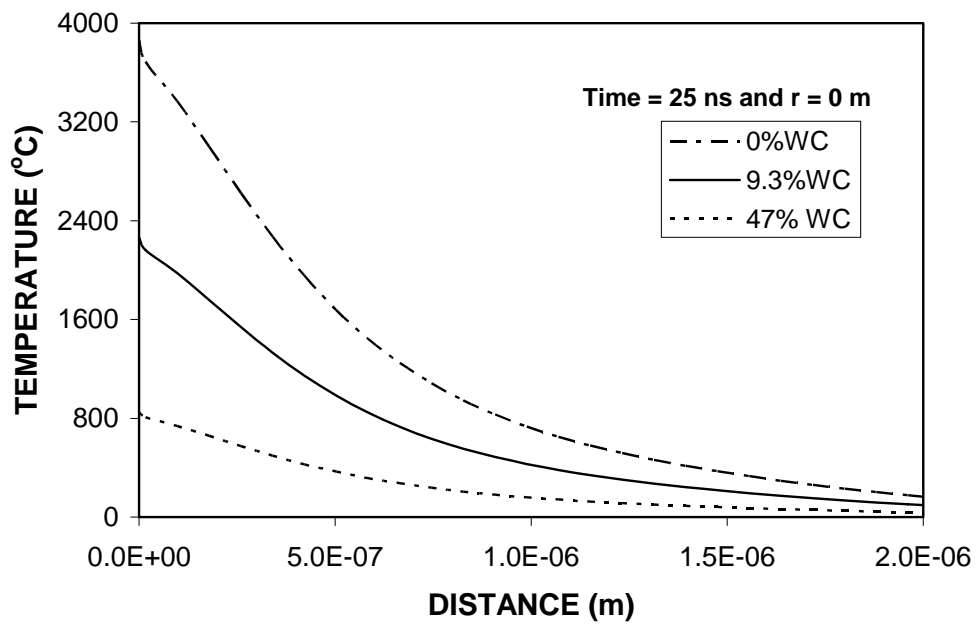
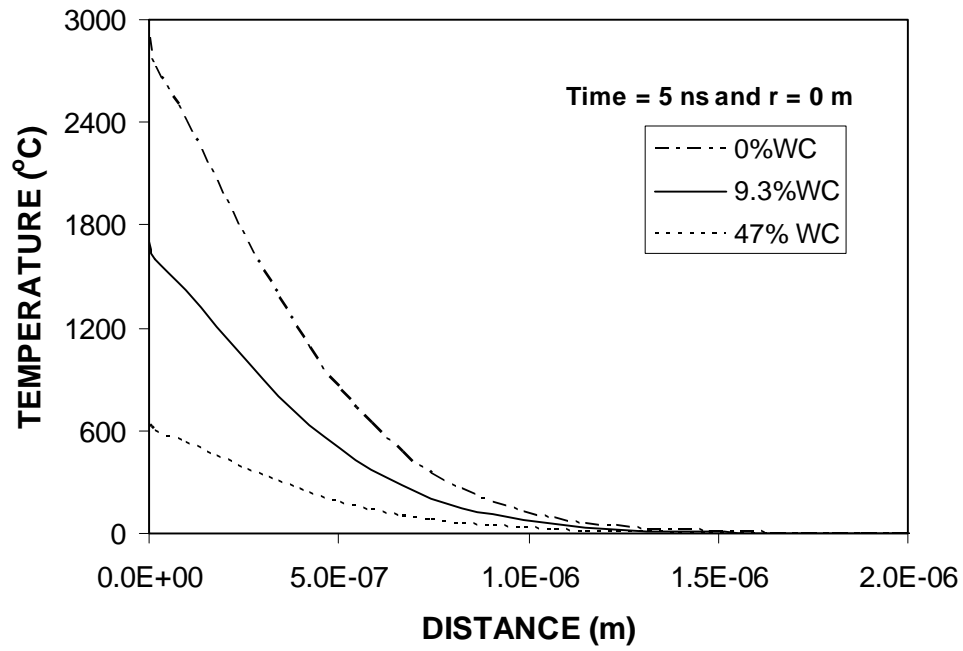


Figure 5.8. Temperature distribution inside the coating at two different heating periods. Inconel 625 powders are blended at different weight ratios of WC.

Table 3.5 gives fracture toughness determined from the indentation tests and elastic modulus determined from the mass fraction of the constituent composition. It is evident that the fracture toughness improves with increasing WC concentration. This is because of the WC dissolution in the surface region where temperature is high. In addition, laser re-melted Inconel 625 coating without WC content is brittle because of the high oxygen content in the surface region [106]. Consequently, homogeneous structure in the surface vicinity of the coating with high WC content slightly enhances the fracture toughness of the coating. Table 5.2 gives the residual stress determined from the XRD technique and the analytical formulation [27]. It can be observed that the residual stress determined from the analytical method is slightly lower than that of the XRD technique, except 47% WC, provided that this difference is small. It should be noted that the analytical expression (equation 2) provides the residual stress at coating interface. Therefore, the discrepancies between the measurement and analytical results are because of the fact that the residual stresses in the coating and at the interface differ as well as the assumptions made in the analytical formulation, i.e. uniform temperature distribution, homogeneous coating structures, and uniform properties of coating. Moreover, increasing WC content increases the residual stress levels in the coating. This is because of the partial

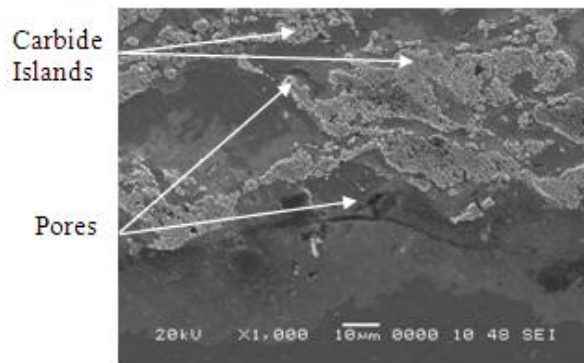
dissolution of WC ion in the Inconel 625 coating during the laser melting, which contributes to the stress levels in the coating. In addition interfacial strain developed at boundaries between WC and W_2C contributes to the residual stress development after the laser re-melting process [107], which is more pronounced in the surface region of the coating where temperature is high due to absorption of laser beam energy. In cooling period, quenching stresses are developed because of the contraction of different constituted molten particles during the solidification. These stresses are mainly tensile and contribute to the total residual stress in the region where the cooling rates are high, particularly in the surface region and in the interfacial region of the coating base substrate [108]. Moreover, the mismatch in thermal contraction between coating and substrate material contributes the residual stress in this region. It should be noted that the temperature gradient generated during the cooling cycle of the re-melting process becomes high for the species with high thermal conductivity in the coating, i.e., high thermal conductivity of WC cools the coating at a faster rate than that of the Inconel 625 in the coating. This results in high temperature gradient across the Inconel 625 and WC particles; as consequence, the level of residual stress increases.

Table 5.2. Residual stress measured using XRD technique and determined from analytical formulation [27]. The error estimated based on the repeats of the XRD measurements is in the order of 5%.

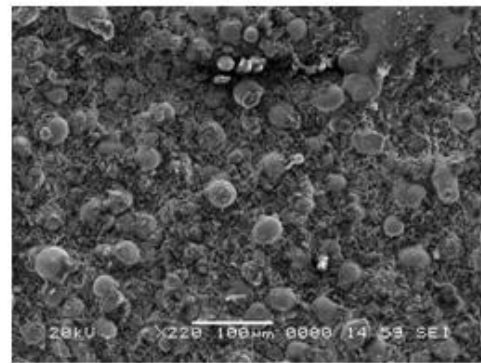
	XRD Technique (MPa)	Analytical MPa
0%WC	300	230
9.3%WC	360	342
47%WC	400	429

Figure 5.9 shows SEM micrographs of the top and cross-sectional views of the coating with two different WC contents. The coating surface is intact and no microcrack is observed. In addition, partial or total disbonded splats at the coating surface are not evident. The cross-sectional examination of the coating reveals that interconnected carbide particles with a mean size of about 2 μm embedded in the Inconel 625 coating are evident. This is more pronounced for the coating with high volume content of WC. The splat pattern forms laminated-like structure in the coating. However, the splats appear to be elongated parallel to the coating surface. The carbide particles form islands with certain degree of homogeneity in the coating. Moreover, the high carbide concentration

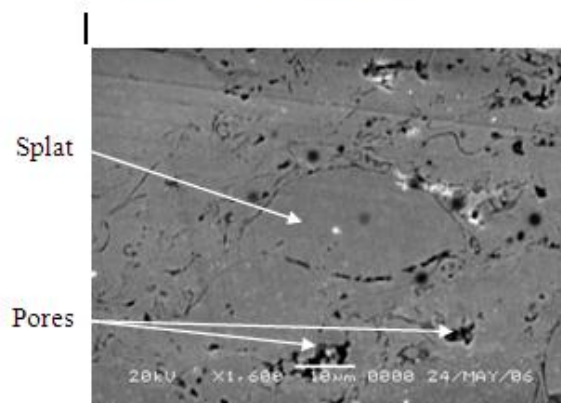
region reveals that some of the carbide particles loss their angularity and partially dissolves in the coating, which is more pronounced for the coating with high carbide concentrations. This situation can also be observed from the EDS line scan across the coating after the laser treatment (Figure 5.10). In this case, W concentration increases locally indicating the existence of the WC particles. However, in the neighborhood of W peaks, W concentration reduces indicating the dissolution of WC in the melt pool and most probably forming the W_2C in this region. This situation occurs in the surface region as well as in the central region of the coating where the liquids temperature is high due to the high rate of the internal energy gain from the irradiated laser energy. In the surface region formation of carbonic gases at high temperatures contributes to reduction in carbon content while forming W_2C . Moreover, the porosity increases slightly with the carbide concentration; in which case, the small gap between the carbide particles and the splats is responsible for the high porosity.



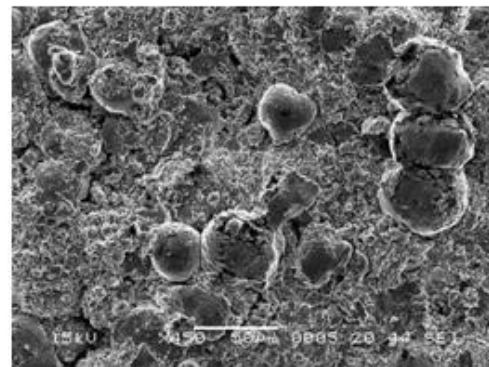
Cross-section of coating with 47% WC



Top view of coating with 47% WC

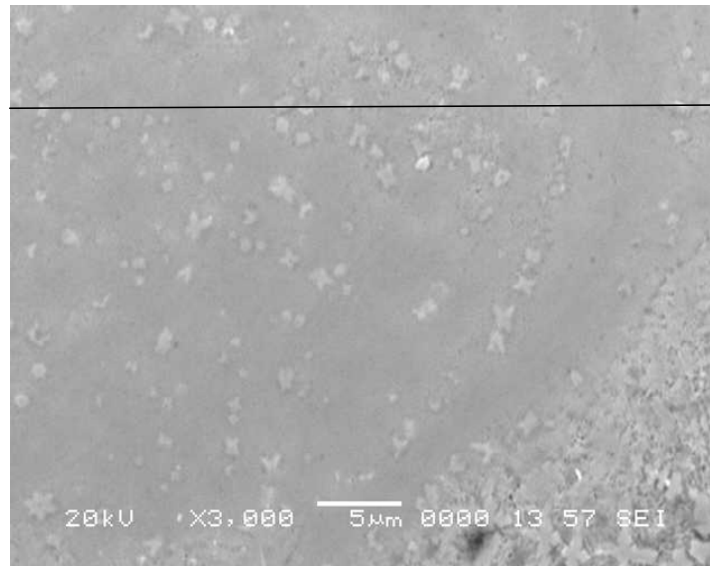


Cross-section of coating with 0% WC



Top view of coating with 0% WC

Figure 5.9. SEM and optical micrographs of coatings with and without WC.



Line
Scann

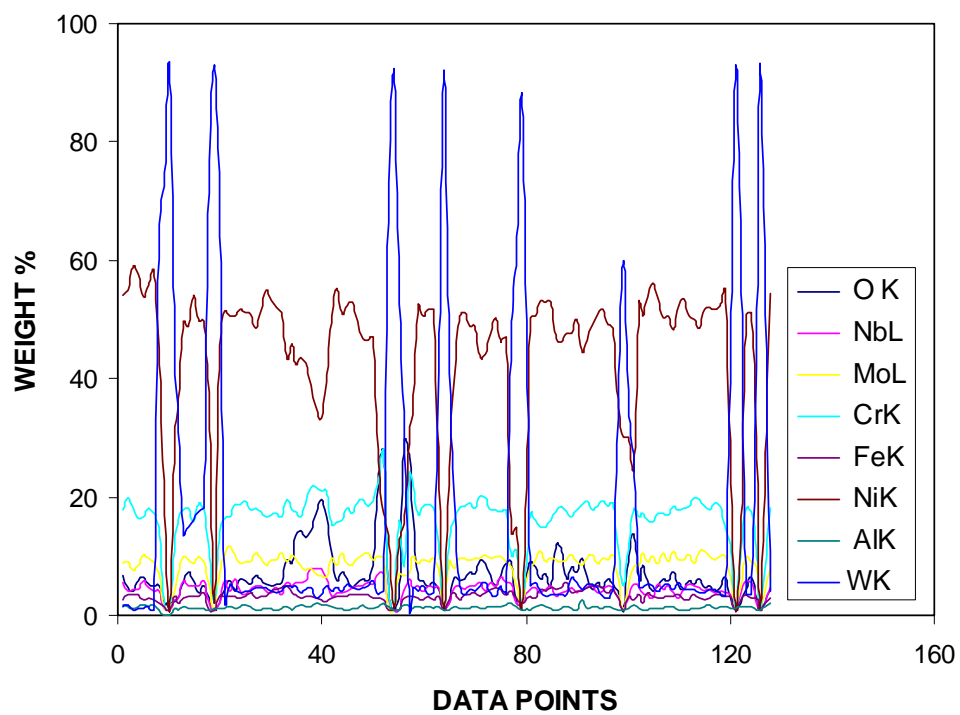


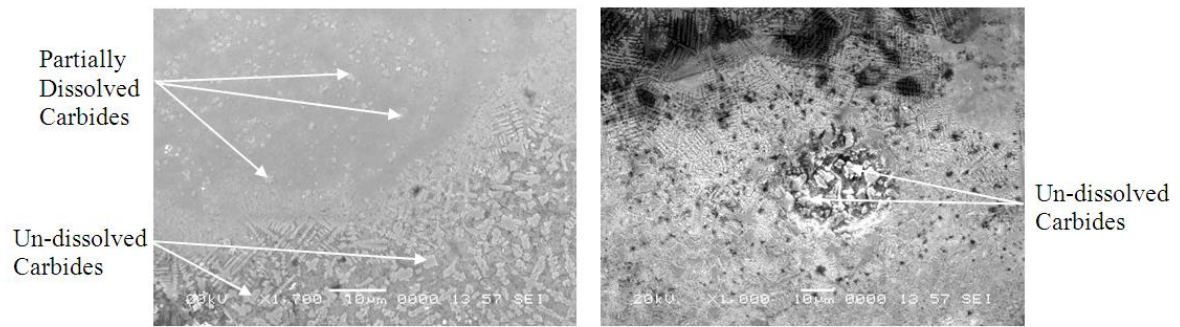
Figure 5.10. EDS line scan in the coating. The existence of low peaks of W and slope of WC peaks (WK) indicates the existence of W_2C and WC dissolution in the coating. (9.3% WC content)

In the case of WC addition and laser melted specimens (Figure 5.11), the cellular structure is superimposed in the lamellar structure modifying the cellular structure as observed for the coating without WC addition. The difference in the thermal properties of coating alloy and WC results in growing of phases at different times in the liquid layer. This causes formation of small cells through polyphase solidification. The crystals of the discontinuous phases nucleate with random orientations; as a consequence, topology with randomly oriented interfaces is resulted. Since the melting temperature of the carbide particles is significantly high (2870 °C [109]), locally scattered un-melted and un-dissolved carbide particles are observed in the coating after the laser melting. This situation is observed in the region close to the coating base substrate material interface where temperature reduces because of the conduction energy losses from coating to the substrate material. The similar observations are also reported in the previous study [107]. However, small tungsten crystallites are formed in the vicinity of the polycrystallite structure. This is also evident from the EDS results; in which case, the local enrichment of tungsten is observed (Table 5.3 and Figure 5.10). In addition, some limited WC dissolution in the central region of the large polycrystalline cells is observed. This is because of loss of carbon through carbonic gas formation during the melting

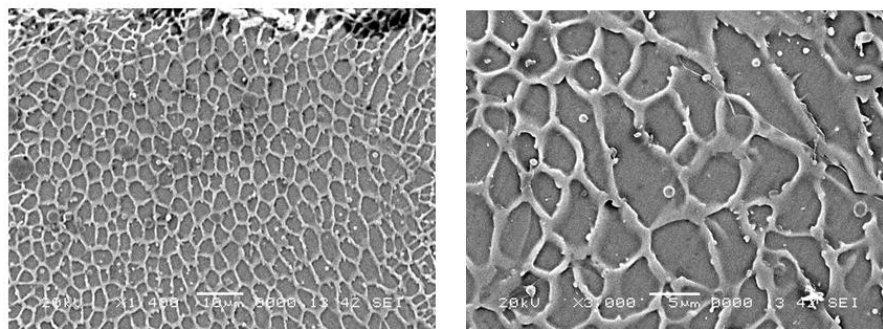
process. It should be noted that the Inconel 625 splats oxidized at the splat boundary during the spraying process [106]. This contributes the carbonic gas formation, particularly in the surface region, during the melting process. In the process of carbonic gas formation, carbon is oxidized at high temperature in the coating and then it is released in the form of carbon oxide from the melt surface.

Table 5.3. EDS analysis results for as received and laser melted coating. The WC content is 9.3% untreated coating.

Spectrum	O	Al	Ti	Cr	Fe	Co	Ni	Mo	W
As Received	0.4	2.01	0.21	13.00	0.75	4.41	Balance	1.81	9.32
Laser Melted	4.00	1.12	0.26	21.43	0.75	3.94	Balance	1.88	14.94



Cross-section of laser melted coating with 47% WC



Cross-section of laser melted coating with 0% WC

Figure 5.11. SEM micrographs of laser melted coatings with and without WC.

Figure 5.12 shows XRD results obtained prior and after the laser melting process. The results show that the coating prior to melting contains WC phase without existing of W_2C compound. This indicates that the formation of carbonic gas and release of carbon monoxide is not possible during the present spraying process. It should be noted that the surface of the splats acts as a sink for carbon, which causes carbon diffusion through the liquid toward the surface, thereby alloying for the decarbonization of the inner part of the splats [110]. In addition, creation

of the new surface through the in-flight particle fragmentation enhances the carburization process. However, W_2C peaks are observed for the laser melted coatings. The presence of W_2C reveals the liberation of carbon from WC into the surroundings of the high temperature melt. Moreover, in the surface region of the coating, carbon can be oxidized and released as carbonic gas to the environment. In addition, existing of Cr_2O_3 peaks for both prior and after the laser melting process suggested that oxidation of splats during in-flight occurs. The laser melting contributes to the Cr_2O_3 formation, particularly in the surface region of the coating. After closed examination of XRD peaks, it can be observed that full width at half maximum (FWHM) of the peak is a broader for the laser melted coating than as sprayed coating. This indicates that the crystals are smaller in the laser melted coating than that of coating without melting.

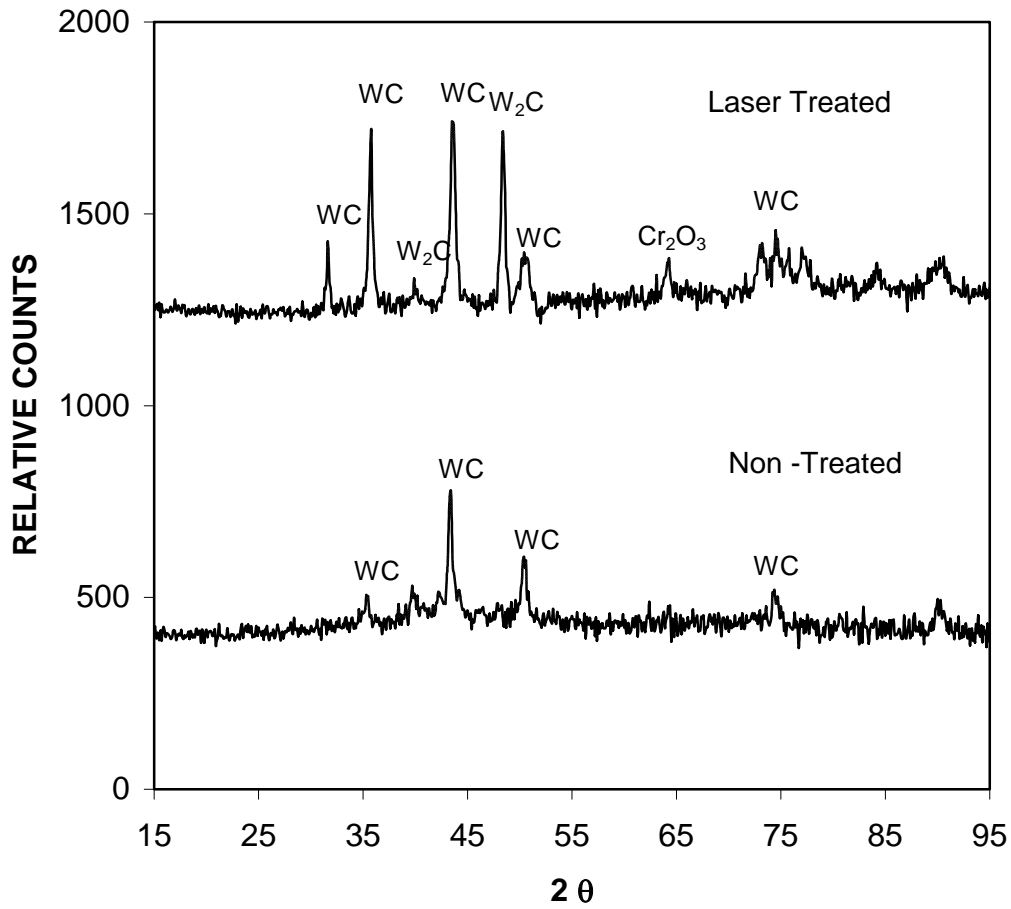


Figure 5.12. XRD results for laser treated and un-treated coating (9.3% WC content).

5.3 Corrosion Behaviour

Typical phase constitutions of various coatings before and after laser treatment, studied using XRD analysis, are indicated in Table 5.4.

Figure 5.13 shows the anodic polarization curves for HVOF Inconel 625 coating with 47%WC before and after laser treatments by diode laser

equipment in deaerated 3.5% NaCl solution at 24 °C, while the corrosion parameters of the three coatings have been summarized in Table 5.5. For sample with 0%WC, the HVOF-sprayed coating presented a passive behaviour with breakdown potential of 175 mV. Both partially- and fully-melted surface presented more positive breakdown potentials of 260 mV and 245 mV respectively. This implied that the content of Fe wt.% caused by the dilution from the base-alloy for the fully-melted layer did not significantly affect the corrosion behaviour. As laser re-melted surface generated solidified structure with a certain degree of inhomogeneity or microsegregation within the interdendritic regions. Once the alloying elements like Cr and Mo, which are the primary elements to promote resistance to corrosion by formation of Cr/Mo oxide film, were tied up as carbides, the regions adjacent to the carbides would be depleted of Cr and Mo elements would reduce the beneficial effect of passivation protection locally. Galvanic cells formed between the carbides and the depleted region around the carbides promoted corrosion to take place. Therefore the improvement in corrosion performance after laser treatment was not significant although the laser treatment eliminated the discrete splats and porosity. With the introduction of the WC phase into the melt pool, not only is there microsegregation from solidification of matrix, but also the

presence of the WC particles forming more complex phases especially after laser treatment, should be considered. In addition, the depletion of alloying elements like Cr and Mo could be more severe when additional WC was added to form other forms of carbides due to the extra C available as a result of dissolution of the WC in the laser melt pool. For samples of 9.3%WC, the passive behaviour of the HVOF-sprayed coating was less obvious compared with Sample of 0%WC, due to the addition of 9.3wt.% of WC, exhibiting a breakdown potential of 170 mV and corrosion current density of $0.106 \mu\text{A}/\text{cm}^2$. However, both partially- and fully-melted coatings demonstrated significant improvement of corrosion resistance, with the breakdown potentials of 770 mV and 700 mV, and corrosion current densities of $0.032 \mu\text{A}/\text{cm}^2$ and $0.018 \mu\text{A}/\text{cm}^2$, respectively. Compared with the laser-melted sample of 0%WC, the laser-melted Sample of 9.3%WC displayed much higher corrosion resistance. This was believed to be caused by the complete dissolution of the WC particles but mainly by the increased amount of W in Ni(γ)-matrix, which enhanced the degree of passivation. In addition, the concentrations of Cr for both laser-melted layers were almost kept the same value of the content of Cr in the HVOF-sprayed coating. It was believed that dissolved W into Ni-matrix might promote a more protective film. It was also reported [111] that alloying of W

element in Co-based alloys improved resistance to erosion and erosion-corrosion. With further increase in amount of the WC to 47 wt.%, the HVOF-sprayed coating displayed a different electrochemical response from the other two types of coatings, which had a relative small passive region with breakdown potential of -100 mV. However, as the potential was shifted more positive from E_{corr} , the current density raised to a stable value of approximately $40\text{--}50$ $\mu\text{A}/\text{cm}^2$. At the potential of approximately $+320$ mV, the second rapid rise in current density was observed. After laser treatment, both partially- and fully-melted surface displayed positive shifted breakdown potentials and decreased corrosion current densities, as shown in Table 5.5. The improvement in the corrosion performance after laser treatment was mainly associated with the elimination of microcrevices between the WC particles and the Ni(γ)-matrix. In addition, the difference of electrochemical potentials between the WC and the matrix could be decreased due to the formation of the interfacial phase between the two phases in the partially-treated layer, and also the completely formation of various new phases, although there is no data available on the relative position of the WC and other alloyed carbides in the electrochemical series [78].

Table 5.4. Phase constitutions of various coatings before and after laser treatment by XRD.

Sample A 0 wt.% of WC	HVOF-sprayed	γ -matrix
	Partially-melted	γ -matrix
	Fully-melted	γ -matrix
Sample 9.3 wt.% of WC	HVOF-sprayed	γ -matrix, WC, W_2C
	Partially-melted	γ -matrix, WC, W_2C , $(Cr, Mo)_2C$, Ni_4W_2C ,
	Fully-melted	γ -matrix, Ni_4W_2C , Fe_3W_3C - Fe_4W_2C
Sample 47 wt.% of WC	HVOF-sprayed	γ -matrix, WC, W_2C
	Partially-treated	γ -matrix, WC, Ni_4W_2C , $(Cr, Mo)_2C$,
	Fully-melted	γ -matrix, WC, Ni_4W_2C , Fe_3W_3C - Fe_4W_2C , $(Cr, Mo)_2C$,

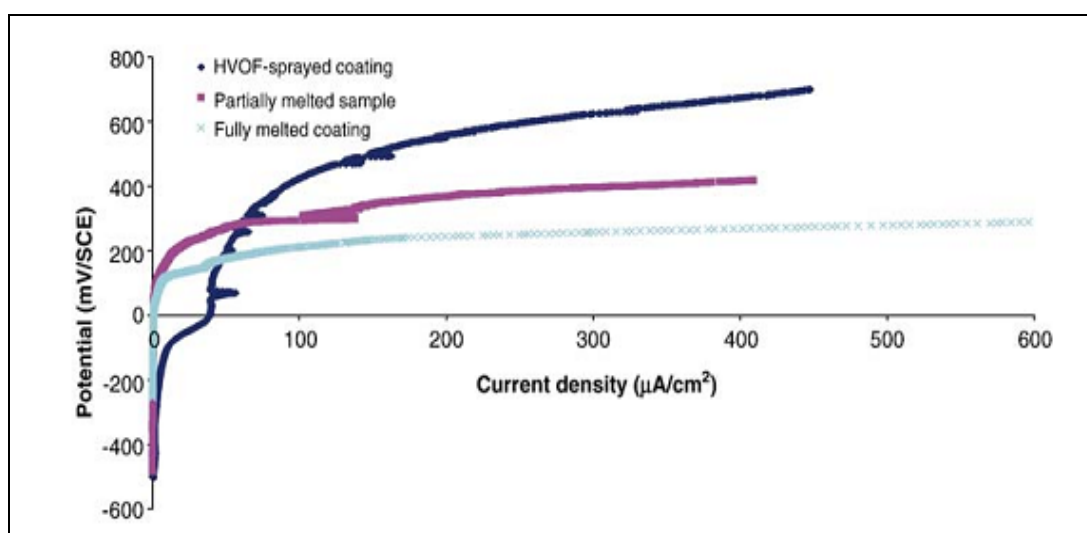


Figure 5.13. Polarization curves of sample 47 wt.% of WC before (dark blue) and after laser treatment (red for partially melted and light blue for fully melted coating).

Table 5.5. Corrosion parameters of various coatings before and after laser treatment.

	Sample	E_{corr}, vs. SCE	I_{corr}, $\mu\text{A}/\text{cm}^2$	Breakdown Potential, E_b, vs. SCE
Sample 0 wt.% of WC	HVOF-sprayed			175
	Partially-melted			260
	Fully-melted			345
Sample 9.3 wt.% of WC	HVOF-sprayed	– 177	0.106	170
	Partially-melted	– 35	0.032	770
	Fully-melted	– 15	0.018	700
Sample 47 wt.% of WC	HVOF-sprayed	– 257	0.382	– 110
	Partially-treated	– 217	0.073	175
	Fully-melted	– 53	0.096	126

Chapter 6 – Conclusions and Suggestions for Future Work

- The predictions of liquid layer thickness agree reasonably well with the experimental findings. However, some small discrepancies between in the results are observed and are attributed to the assumptions made in the current analysis. In this case, the assumptions of homogeneous structure, constant thermal properties, and uniform laser heating situation are mainly responsible for these discrepancies. The re-crystallization of the laser melted layer results in cellular structure with different sizes. The change in the cell size is due to cooling rates, which are non-uniform in all directions. However, constitutional super-cooling causes the development of a transverse growth of cellular structure; in which case, elongated cellular structure is observed locally. The corrugations are almost parallel to the direction of growth of the crystals. Moreover, rapidly decanted liquid at the solid liquid interface results in almost uniformly distributed cellular structure. The free dendritic growth is observed locally,

which is attributed to the extension of super-cooling due to locally reduced temperature gradient. The cellular type dendritic growth is also observed; in which case, the temperature gradient in the liquid phase is small and latent heat of fusion is conducted into the solid.

- Increasing the WC percentage lowers the temperature rise and its gradient in the coating. This is because of increasing thermal conductivity with increasing WC concentration in the coating. Moreover, differences in the thermal properties of the coating and WC result in the formation of small cells though polyphase solidification. WC dissolution in the central region of the large polycrystalline cells is observed due to the loss of carbon through carbonic gas formation. This situation is also observed from the XRD graph; in which case, the presence of W_2C peaks is evident. Increasing WC concentration improves the elastic modulus and the fracture toughness of the coating. However, the residual stress increases significantly with increasing WC content in the coating. The residual stress measured from the XRD technique shows general agreement with the results obtained from the previous analytical formulation.

- Laser surface treatment was found to improve the corrosion performance of the various HVOF-sprayed coatings as a result of the removal of the discrete splat-structure and micro-crevices, and also the reduction of compositional gradient between the WC and the matrix due to the formation of interfacial phases. Polarization curves demonstrated a significant improvement of corrosion resistance with the breakdown potentials of high positive value and corrosion current densities of low value. Furthermore, it was proven that the laser-melted sample of 9.3%WC displayed much higher corrosion resistance than the sample of 0.0%WC (no WC addition).

Suggestions for Future Work

In the present study, laser re-melting of HVOF coating was studied and the microstructural analysis prior and post re-melting has been carried out. Inconel 625 with addition of WC particles is used as the spraying powder while stainless steel (SS 304) is used as the based material for the coating. EDS, optical microscopy, and SEM are conducted for material characterization. The microstructural analyses show that increase of WC percentage in the spraying powder would contribute to the residual stress levels and the fracture toughness of the coating, which is due to improper distribution of WC particles in the coating. Moreover, laser heating situation is modeled using the lump parameter analysis and predications are compared with the experimental findings. However, assumptions of uniform properties in the analytical formulation resulted in some discrepancies in the melt depth predictions. Consequently, the following studies are suggested as the future work:

- Improve the theoretical model by incorporating varying material properties. In this case, linear or quadratic variation of thermal properties with coating depth can be adopted in the formulation. In addition, ANSYS FEM code can be used to predict the melt layer thickness for the validation of the code developed.

- Other hard particles like TiC or TaC can be mixed with Inconel 625 powders prior to spraying. The effect of hard particles on the coating properties can be examined. This will form the basis for comparison of the coating properties when WC is mixed.
- The heat treatment of coating after laser re-melting process can be carried out to examine the stress relaxation in the coating. This may allow accommodating high percentage of WC concentration in the coating while improving the mechanical properties of the coating in the surface region.
- The effect the gradually varying (functional gradient) hard particle concentration in the coating can be examined while spraying at increasing percentage of WC particles in Inconel 625 powder. This will provide high concentration of WC at the surface of the coating, which is expected to improve the tribological properties.

References

- [1] W. M. Steen, Laser Material Processing, 1994, Springer – Verlag, London.
- [2] <http://www.airproducts.com/Products/CylinderGases/default.htm>, 2008
- [3] C. Reignier and A. Sturgeon, HVOF Sprayed WC-Co-Cr as a Generic Coating Type for Replacement of Hard Chrome Plating, Paper 99, presented at ITSC 2002 International Thermal Spray Conference, 4-6, 2002, Essen, Germany.
- [4] A. J. Sturgeon, The corrosion behaviour of HVOF sprayed stainless steel and nickel alloy coatings in artificial seawater, Paper No.03245 presented at CORROSION 2003, NACE Conference, 16-21, 2003, San Diego, CA, USA.
- [5] J. Sturgeon, Improved Corrosion Resistant Coatings Prepared Using a Modified Diamond Jet HVOF Spraying System, Paper 171 presented at ITSC 2002 International Thermal Spray Conference, 2002, Essen, Germany.
- [6] M. D. F. Harvey, S. Shrestha and A. Sturgeon, Coatings for offshore applications by high velocity wire flame spraying, NACE 2005, Houston, Texas.
- [7] www.twi.co.uk/content/faqsk016.html, 2008
- [8] Y. I. Posudin, Laser in Agriculture, 1998, Science Publisher Inc., USA.
- [9] B. Eigenmann, Residual Stresses due to Thermal, Thermo-Chemical and Mechanical Surface Treatments: Generation, Determination, Evaluation, Proc. Surface Treatment, 95, 1995, 17-25.

- [10] M. de Freitas, M.S. Pereira, H. Michaud and D. Pantelis, Analysis of residual stresses induced by laser processing, *Materials Science and Engineering, A* 167, 1993, 115-122.
- [11] M. Schneider, laser cladding with powder, 1998, Ph.D. Thesis, University of Twente, Enschede, The Netherlands.
- [12] B. R. Marple, J. Voyer, J. F. Bisson and C. Moreau, thermal spraying of nanostructured cermet coatings, *Journal of Materials Processing Technology*, 17, 2001, 418-423.
- [13] H. L. de Villiers Lovelock, P. W. Richter, J. M. Benson and P. M. Young, Parameter Study of HP/HVOF Deposited WC-Co Coatings, *Journal of Thermal Spray Technology*, 7, 1998, 97-107.
- [14] L. Jacobs, M. M. Hyland and M. De Bonte, Comparative study of WC-cermet coatings sprayed via the HVOF and the HVOF Process, *Journal of Thermal Spray Technology*, 7, 1998, 213-218.
- [15] H. Li, K. A. Khor and P. Cheang, Effect of the powders' melting state on the properties of HVOF sprayed hydroxyapatite coatings, *Materials Science and Engineering, A* 293, 2000, 71-80.
- [16] L. Zhao., M. Maurer, F. Fischer, R. Dicks and E. Lugscheider, Influence of spray parameters on the particle in-flight properties and the properties of HVOF coating of WC-CoCr, *Wear*, 257, 2004, 41-46.
- [17] M. P. Planche, B. Normand, H. Liao, G. Rannou, C. Coddet, Influence of HVOF spraying parameters on in-flight characteristics of Inconel 718 particles and correlation with the electrochemical behaviour of the coating, *Surface and Coatings Technology*, 157, 2002, 247-256.
- [18] E. Lugscheider, C. Herbst and L. Zhao, Parameter studies on high-velocity oxy-fuel spraying of MCrAlY coatings *Surface and Coatings Technology*, 108-109, 1998, 16-23.

- [19] Y. Y. Wang, C. J. Li and A. Ohmori, Examination of factors influencing the bond strength of high velocity oxy-fuel sprayed coatings, *Surface & Coatings Technology*, 200, 2006, 2923– 2928.
- [20] C. J. Li, Y. Y. Wang, T. Wu, G. C. Ji and A. Ohmori, Effect of types of ceramic materials in aggregated powder on the adhesive strength of high velocity oxy-fuel sprayed cermet coatings, *Surface and Coatings Technology*, 145, 2001, 113-120.
- [21] A. Dolatabadi, J. Mostaghimi and V. Pershin, Effect of a cylindrical shroud on particle conditions in high velocity oxy-fuel spray process, *Science and Technology of Advanced Materials*, 3, 2002, 245–255.
- [22] D. M. Nuruzzaman, A. Nakajima and T. Mawatari, Effects of substrate surface finish and substrate material on durability of thermally sprayed WC cermet coating in rolling with sliding contact, *Tribology International*, 39, 2006, 678–685.
- [23] T. Y. Cho, J. H. Yoon, K. O. Song, Y. K. Joo, W. Fang, S. H. Zhang, S. J. Youn, H. G. Chun and S. Y. Hwang, A study on HVOF coatings of micron and nano WC-Co powders, *Surface and Coating Technology*, 202, 2008, 5556-5559.
- [24] Y. Qiao, T. E. Fischer and A. Dent, The effects of fuel chemistry and feedstock powder structure on the mechanical and tribological properties of HVOF thermal-sprayed WC–Co coatings with very fine structures, *Surface and Coatings Technology*, 172, 2003, 24–41.
- [25] P. Chivavibul, M. Watanabe, S. Kuroda and K. Shinoda, Effects of carbide size and Co content on the microstructure and mechanical properties of HVOF-sprayed WC-Co coatings, *Surface and Coating Technology*, 202, 2007, 509-521.
- [26] H. Liao, P. Vaslin, Y. Yang, C. Coddet, Determination of residual stress distribution from in situ curvature measurements for thermally sprayed WC/Co coatings, *Journal of Thermal Spray Technology*, 6(2), 1997, 235-412.

- [27] J. Stokes and L. Looney, Residual stress in HVOF thermally sprayed thick deposit, *Surface and Coating Technology*, 117-118, 2004, 18-23.
- [28] M. Toparli, F. Sen, O. Culha and E. Celik, Thermal stress analysis of HVOF sprayed WC-Co/NiAl multilayer coatings on stainless steel substrate using finite element methods, *Journal of Material Processing Technology*, 190, 2007, 26-32.
- [29] C. R. C. Lima, J. Nin and J. M. Guilemany, Evaluation of residual stresses of thermal barrier coatings with HVOF thermally sprayed bond coats using the modified layer removal method (MLRM), *Surface and Coatings Technology*, 200(12-13), 2006, 5963-5972.
- [30] S. C. Gill and T. W. Clyne, Investigation of residual stress generation during thermal spraying by continuous curvature measurement, *Thin Solid Films*, 250, 1994, 172-180.
- [31] O. Kesler, O. J. Matejcek, S. Sampath, S. Suresh, T. Gnaeupel-Herold, P. C. Brand, and H. J. Prask, Measurement of residual stress in plasma-sprayed metallic, ceramic and composite coatings, *Materials Science & Engineering*, 257(2), 1998, 215-224.
- [32] Y. Y. Santana, J. G. La Barbera-Sosa, M. H. Staia, J. Lesage, E. S. Puchi-Cabrera, D. Chicot and E. Bemporad, Measurement of residual stress in thermal spray coatings by the incremental hole drilling method, *Source: Surface & Coatings Technology*, 201(5), 2006, 2092-2098.
- [33] T. C. Totemeier and R. N. Wright, Residual stress determination in thermally sprayed coatings – a comparison of curvature models and X-ray techniques, *Surface and Coatings Technology*, 200(12-13), 2006, 3995-3962.
- [34] J. Wang, P. Shortriya and K. S. Kim, Surface residual stress measurement using curvature interferometry, *Experimental Mechanics*, 46, 2006, 39-46.

- [35] R. Ghafouri-Azar, J. Mostaghimi and S. Chandra, Modelling development of residual stresses in thermal spray coatings, *Computational Materials Science*, 35, 2006, 13-26.
- [36] F. Otsubo, K. Kishitake and T. Terasaki, Residual stress distribution in thermally sprayed self-fluxing alloy coatings, *Materials Transactions*, 46(11), 2005, 2473-2477.
- [37] R. T. F. McGrann, D. J. Greving, J. R. Rybicki, B. E. Bodger and D. A. Somerville, Effect of residual stress in HVOF tungsten carbide coatings on the fatigue life in bending of thermal spray coated aluminum, *Journal of Thermal Spray Technology*, 7(4), 1998, 546-552.
- [38] J. Stokes and L. Looney, HVOF system definition to maximise the thickness of formed components, *Surface and Coatings Technology*, 148, 2001, 18-24.
- [39] R. Ahmed, Contact fatigue failure modes of HVOF coatings, *Wear* 253, 2002, 473–487.
- [40] S. Stewart and R. Ahmed, Contact fatigue failure modes in hot isostatically pressed WC-12%Co coatings, *Surface and Coatings Technology*, 172, 2003, 204–216.
- [41] L. Hernandez, F. Oliveira, J. A. Berryos, C. Villalobos, A. Pertuz and E. S. Puchi Cabrera, Fatigue properties of a 4340 steel coated with a Colmonoy 88 deposit applied by high-velocity oxygen fuel, *Surface and Coatings Technology* 133-134, 2000, 68-77.
- [42] K. Padilla, A. Velasquez, J. A. Berros and E. S. Puchi Cabrera, Fatigue behaviour of a 4140 steel coated with a NiMoAl deposit applied by HVOF thermal spray, *Surface and Coatings Technology*, 150, 2002, 151–162.
- [43] M. Cherigui, N. E. Fenineche and C. Coddet, Structural study of iron-based microstructured and nanostructured powders sprayed by HVOF thermal spraying, *Surface & Coatings Technology*, 192, 2005, 19– 26.

- [44] F. Toma, G. Bertrand, S. Chwa, D. Klein, H. Liao, C. Meunier, and C. Coddet, Microstructure and photocatalytic properties of nanostructured TiO₂ and TiO₂-Al coatings elaborated by HVOF spraying for the nitrogen oxides removal, *Materials Science and Engineering, A* 417, 2006, 56–62.
- [45] G. Yang, C. Li, F. Han and A. Ohmori, Microstructure and photocatalytic performance of high velocity oxy-fuel sprayed TiO₂ coatings, *Thin Solid Films*, 466, 2004, 81– 85.
- [46] C. H. Lee and K. O. Min, Effects of heat treatment on the microstructure and properties of HVOF-sprayed Ni-Cr-W-Mo-B alloy coatings, *Surface and Coatings Technology* 132, 2000, 49-57.
- [47] H. Weiss, Adhesion of advanced overlay coatings: mechanisms and quantitative assessment, *Surface and Coatings Technology*, 71, 1995, 201-207.
- [48] L. Li, X. Y. Wang, G. Wei, A. Vaidya, H. Zhang, S. Sampath 2004, Substrate melting during thermal spray splat quenching, *Thin Solid Films*, 468, 2004, 113-119.
- [49] K. A. Khor, H. Li and P. Cheang, Significance of melt-fraction in HVOF sprayed hydroxyapatite particles, splats and coatings, *Biomaterials*, 25, 2004, 1177-1186.
- [50] Y. Hu, M. Aindow, I. P. Jones and I. R. Harris, Effects of Zn coating on the microstructure and magnetic properties of Nd-Fe-B magnets, *Journal of Alloys and Compounds*, 351, 2003, 299-303.
- [51] K. Tokunaga, N. Yoshida, N. Noda, T. Sogabe and T. Kato, 1998, High heat load properties of tungsten coated carbon materials, *Journal of Nuclear Materials* 258-263, 1998, 998-1004.
- [52] M. Mellali, P. Fauchais and A. Grimaud, Influence of substrate roughness and temperature on the adhesion/cohesion of alumina coatings *Surface and Coatings Technology*, 81, 1996, 275-286.

- [53] P. Fauchais, M. Vardelle, A. Vardelle and L. Bianchi, Plasma spray: Study of the coating generation, *Ceramics International*, 22, 1996, 295-303.
- [54] A. L. Hutson, M. Niinomi, T. Nicholas and D. Eylon, Effect of various surface conditions on fretting fatigue behaviour of Ti-6Al-4V, *International Journal of Fatigue*, 24, 2002, 1223-1234.
- [55] S. Amada and T. Hirose, Influence of grit blasting pre-treatment on the adhesion strength of plasma sprayed coatings: fractal analysis of roughness, *Surface and Coatings Technology*, 102, 1998, 132-137.
- [56] C. J. Li, Y. Y. Wang, T. Wu, G. C. Ji and A. Ohmori, Effect of types of ceramic materials in aggregated powder on the adhesive strength of high velocity oxy-fuel sprayed cermet coatings, *Surface and Coatings Technology*, 145, 2001, 113-120.
- [57] P. H. Suegama, C. S. Fugivara, A.V. Benedetti, J. Fernandez, J. Delgado and J. M. Guilemany, Electrochemical behaviour of thermally sprayed stainless steel coatings in 3.4% NaCl solution, *Corrosion Science*, 47, 2005, 605-620.
- [58] A. A. Boudi, M. S. J. Hashmi, B. S. Yilbas, HVOF coating of Inconel 625 onto stainless and carbon steel surfaces: corrosion and bond testing, *Journal of Materials Processing Technology*, 155-156, 2004, 2051-2055.
- [59] T. Sundararajan, S. Kuroda, F. Abe, S. Sodeoka, Effect of thermal cycling on the adhesive strength of Ni-Cr coatings, *Surface and Coatings Technology*, 194 (2-3), 2005, 290-299.
- [60] R. A. Mahesh, R. Jayaganthan and S. Prakash, Evaluation of hot corrosion behaviour of HVOF sprayed NiCrAl coating on superalloys at 900 °C, *Material Chemistry and Physics*, 111, 2008, 524-533.
- [61] P. K. Aw, A. L. K. Tan, T. P. Tan and J. Qiu, Corrosion resistance of tungsten carbide based cermet coatings deposited by High Velocity Oxy-Fuel spray process, *Thin Solid Film*,

516, 2008, 5710-5715.

- [62] P. H. Shipway and L. Howell, Microscale abrasion–corrosion behaviour of WC–Co hardmetals and HVOF sprayed coatings, *Wear*, 258, 2005, 303-312.
- [63] H. Chen, C. Xu, Q. Zhou, I. M. Hutchings, P.H. Shipway and J. Liu, Micro-scale abrasive wear behaviour of HVOF sprayed and laser-remelted conventional and nanostructured WC–Co coatings, *Wear*, 258, 2005, 333-338.
- [64] H. Y. Al-Fadhli, J. Stokes, M.S.J. Hashmi, B.S. Yilbas, The erosion–corrosion behaviour of high velocity oxy-fuel (HVOF) thermally sprayed inconel-625 coatings on different metallic surfaces, *Surface and Coatings Technology*, 200 (20-21), 2006, 5782-5788.
- [65] W. Pang, H. C. Man and T. M. Yue, Laser surface coating of Mo-WC metal matrix composite on Ti6Al4v alloy, *Material Science and Engineering, A* 390, 2005, 144-153.
- [66] P. Wu, C. Z. Zhou and X. N. Tang, Microstructural Characterization and Wear Behaviour of Laser Cladded Nickel-Based and Tungsten Carbide Composite Coatings, *Surface and Coatings Technology*, 166, 2003, 84-88.
- [67] B. S. Yilbas, A. F. M. Arif and M. A. Gondal, HVOF coating and laser treatment: three-point bending tests, *Journal of Materials Processing Technology*, 164-165, 2005, 954-957.
- [68] J. Mateos, J. M. Cuetos, R. Vijande and E. Fernandez, Tribological properties of plasma sprayed and laser remelted 75/25 Cr₃C₂/NiCr coatings, *Tribology International*, 34, 2001, 345-351.
- [69] B. S. Sidhu, D. Puri and S. Prakash, Mechanical and metallurgical properties of plasma sprayed and laser remelted Ni–20Cr and Stellite-6 coatings, *Journal of Materials Processing Technology*, 159, 2005, 347-355.

- [70] J. Morimoto, T. Onoda, Y. Sasaki and N. Abe, Improvement of solid cold sprayed TiO₂–Zn coating with direct diode laser, *Vacuum*, 73, 2004, 527-532.
- [71] J. Mateos, J.M. Cueto, E. Fernandez and R. Vijande, Tribological behaviour of plasma-sprayed WC coatings with and without laser remelting, *Wear*, 239, 2000, 274-281.
- [72] J. Mateos, J.M. Cueto, E. Fernandez and R. Vijande, Tribological properties of plasma sprayed and laser re-melted 75/25 Cr₃C₂/NiCr coatings, *Tribology International*, 34(5), 2001, 345-351.
- [73] G. Y. Liang, T. T. Wong, J. M. K. MacAlpine and J. Y. Su, A study of wear resistance of plasma-sprayed and laser-remelted coatings on aluminium alloy, *Surface and Coatings Technology*, 127 (2-3), 2000, 233-238.
- [74] J. Tuominen, P. Vuoristo, T. Mantyla, M. Kylmalahti, J. Vihinen and P. H. Andersson, Improving corrosion properties of high-velocity oxy-fuel sprayed Inconel 625 by using a high-power continuous wave neodymium-doped yttrium aluminium garnet laser, *Journal of Thermal Spray Technology*, 9 (4), 2000, 513-519.
- [75] M. Oksa, E. Turunen and T. Varis, Sealing of thermally sprayed coatings, *Surface Engineering*, 20 (4), 2004, 251-254.
- [76] D. Zhang and X. Zhang, Laser cladding of stainless steel with Ni–Cr₃C₂ and Ni–WC for improving erosive–corrosive wear performance, *Surface & Coatings Technology*, 190, 2005, 212– 217.
- [77] S. W. Huang, M. Samandi and M. Brandt, Abrasive wear performance and microstructure of laser clad WC/Ni layers, *Wear*, 256 (11-12), 2004, 1095-1105.
- [78] K. P. Cooper, P. Slebodnick and E. D. Thomas, Seawater corrosion behaviour of laser surface modified Inconel 625 alloy, *Materials Science and Engineering*, A206 (1), 1996, 138-149.

- [79] J. Suutala, Tuominen, and P. Vuoristo, Laser-assisted spraying and laser treatment of thermally sprayed coatings, *Surface & Coatings Technology*, 201, 2006, 1981-1987.
- [80] A. Hjornhede, A. Nylund, Adhesion testing of thermally sprayed and laser deposited coatings, *Surface and Coatings Technology*, 184, 2004, 208-218.
- [81] S. Kumari, A.S. Khanna and A. Gasser, The influence of laser glazing on morphology, composition and microhardness of thermal sprayed Ni-WC coatings, *Surface Engineering - Proceedings of the 4th International Surface Engineering Conference*, 200 (2006) 128-135.
- [82] P. Bansal , P. H. Shipway, S. B. Leen, Finite element modelling of the fracture behaviour of brittle coatings, *Surface & Coatings Technology*, 200, 2006, 5318 – 5327.
- [83] P. Bansal , P. H. Shipway, S. B. Leen, Residual stresses in high-velocity oxy-fuel thermally sprayed coatings – Modelling the effect of particle velocity and temperature during the spraying process, *Acta Materialia*, 55, 2007, 5089-5101.
- [84] V. V. Sobolev, J. M. Guilemany, A. J. Martin, J. A. Calero, P. Vilarrubias, Modelling of the in-flight behaviour of stainless steel powder particles in high velocity oxy-fuel spraying, *Journal of Materials Processing Technology*, 79, 1998, 213–216.
- [85] M. M. Lima, C. Godoy, J. C. Avelar-Batista, P. J. Modenesi, Toughness evaluation of HVOF WC-/Co coatings using non-linear regression analysis, *Materials Science and Engineering*, A357, 2003, 337-345.
- [86] J. Koutsky, High velocity oxy-fuel spraying, *Journal of Materials Processing Technology*, 157–158, 2004, 557–560.
- [87] Brilliant Cutting machine, 220, made by ATA in Germany / Applied Surface Technology Ltd. UK.

- [88] Enviraclean, series 2000, Engineered finishing system, Hodge Clemco Ltd / Applied Surface Technology Ltd. UK.
- [89] HVOF JP-5000, model 5220 Gun, TAFA, Praxair S.T. Technology, Inc. / Applied Surface Technology Ltd. UK.
- [90] T. C. Totemeier and R. N. Wright, Residual stress determination in thermally sprayed coatings – a comparison of curvature models and X-ray techniques, *Surface and Coatings Technology*, 200(12-13), 2006, 3995-3962.
- [91] W. C. Oliver and G. M. Pharr, Improved technique for determining hardness and elastic modulus using load and displacement sensing indentation experiments, *J of Materials Research*, 7, 1992, 1564-1580.
- [92] K. Niihara, R. Morena and D. P. H. Hasselman, Indentation fracture toughness of brittle materials for palmqvist cracks, *Fracture Mechanics of Ceramics*, 5, 1983, 97-105.
- [93] E. Lopez Cantera and B. G. Mellor, Fracture toughness and crack morphologies in eroded WC-Co-Cr thermally sprayed coatings, *Materials Letters*, 37, 1998, 201-210.
- [94] A. G. Evans and E. A. Charles, Fracture Toughness Determinations by Indentation, *Journal of the American Ceramic Society*, 59, 1976, 370–371.
- [95] G. R. Anstis, P. Chantikul, B. R. Lawin, D. B. Marshall, A Critical Evaluation of Indentation Techniques for Measuring Fracture Toughness: I, Direct crack measurements, *Journal of the American Ceramic Society*, 64, 1981, 533-538.
- [96] A. G. Evans, T. R. Wilshaw, Quasi-static solid particle damage in brittle solids—I. Observations analysis and implications, *Acta Metallurgica*, 24(10), 1976, 939-956.
- [97] B. S. Yilbas and A. Z. Sahin, Turbulent boundary layer approach allowing chemical reactions for CO₂ laser oxygen assisted cutting process. *Proc. of Instn. Mech. Eng. C: J. Mech. Eng. Sci.* 208, 1994, 275–84.

- [98] W. H. Dorrance, *Viscous Hypersonic Flow*, 1992, New York: McGraw-Hill.
- [99] H. Schlichting, *Boundary Layer Theory*, 7th edition, 1979, New York: McGraw-Hill.
- [100] B. S. Yilbas and B. J. Abdul Aleem, Dross formation during laser cutting process, *J. Phys. D: Appl. Phys.* 39, 2006, 1451–1461.
- [101] B. S. Yilbas and M. Kalyon, Repetitive laser pulse heating analysis: pulse parameter variation effects on closed form solution, *Applied Surface Science*, 252, 2006, 2242–2250.
- [102] M. Abramowitz and I. A. Stegun, "Handbook of Mathematical Functions", 1965, Dover, New York.
- [103] <http://www.hightempmetals.com/techdata/hitempInconel625data.php>, 2008
- [104] S. Z. Shuja, B. S. Yilbas and M. O. Budair, Modelling of laser heating of solid substance including assisting gas impingement. *Numerical Heat Transfer, A* 33, 1998, 315-339.
- [105] B. S. Yilbas, S. Z. Shuja and M.O. Budair, Nano-second pulse heating and gas assisting jet considerations, *Int. J. Machine Tools and Manufacture*, 40, 2000, 1023-1038.
- [106] D. Al-Anazi, M. S. J. Hashmi and B. S. Yilbas, HVOF coating of AMDRY 9954 onto Ti-6Al-4V alloy: fracture toughness measurement, *Proc. Inst. Mech. Engrs., Part B, Journal of Engineering Manufacture*, 221, 2007, 617-623.
- [107] J. A. Vreeling, V. Ocelik and J. T. M. De Hosson, Ti-6Al-4V strengthened by laser melt injection of WCp particles, *Acta Materialia*, 50, 2002, 4913-4924.
- [108] J. Pina, A. Dias and J. L. Lebrun, Study by X-ray diffraction and mechanical analysis of the residual stress generation during thermal spraying, *Material Science and Engineering*, A347, 2003, 21-31.

- [109] R. C. West, Handbook of Chemistry and Physics, 36th edition, Bocan Raton, FL, CRC Press (1982-1983).
- [110] C. Verdon, A. Kerimi and J. L. Martin, A study of high velocity oxy-fuel thermally sprayed tungsten carbide based coatings. Part 1: microstructure, Materials Science and Engineering, A246, 1998, 11-24.
- [111] U. Malayoglu and A. Neville, Mo and W as alloying elements in Co-based alloys - Their effects on erosion-corrosion resistance, Wear, 259 (1-6), 2005, 219-229.

Publications by the Author

- Z. Liu, J. Cabrero, S. Niang, Z. Y. Al-Taha, Improving corrosion and wear performance of HVOF-sprayed Inconel 625 and WC-Inconel 625 coatings by high power diode laser treatments, *Surface and Coatings Technology*, Volume 201, Issues 16-17, 21 May 2007, Pages 7149-7158.
- Z. Y. Taha-al, M. S. Hashmi, B. S. Yilbas, Laser treatment of HVOF coating- model study and characterization, *Journal of Mechanical Science and Technology* Vol.21 No.10, 2007, pp. 1439-1444.
- Z. Y. Taha-al, M. S. Hashmi, B. S. Yilbas, Effect of WC on the residual stress in the laser treated HVOF coating, *Journal of Materials Processing Technology*, In Press, Corrected Proof. doi:10.1016/j.jmatprotec.2008.07.027.